MODELING AND MODE TRANSITION CONTROL OF AN HCCI CAPABLE SI ENGINE

By

Shupeng Zhang

A DISSERTATION

Submitted to
Michigan State University
in partial fulfillment of the requirements
for the degree of

Mechanical Engineering - Doctor of Philosophy

2014

ABSTRACT

MODELING AND MODE TRANSITION CONTROL OF AN HCCI CAPABLE SI ENGINE

By

Shupeng Zhang

While the homogeneous charge compression ignition (HCCI) combustion has its advantages of high thermal efficiency with low emissions, its operational range is limited in both engine speed and load. To utilize the advantage of the HCCI combustion an HCCI capable SI (spark ignition) engine is required. One of the key challenges of developing such an engine is to achieve smooth mode transition between SI and HCCI combustion, where the in-cylinder thermal and charge mixture properties are quite different due to the distinct combustion characteristics. In this research, mode transition between SI and HCCI combustion was investigated for an HCCI capable SI engine equipped with electrical variable valve timing (EVVT) systems, dual-lift valves and electronic throttle control (ETC) system.

For the purpose of reducing research cost and development duration, one of the most efficient approaches is to develop and validate the control strategy using an HIL (hardware-in-the-loop) simulation environment, where the real engine is replaced by a control-oriented real-time engine model. This dissertation describes a two-zone HCCI combustion model, where the in-cylinder charge is divided into the well-mixed and unmixed zones as the result of charge mixing. Simplified fluid dynamics is used to predict the residual gas fraction before the combustion phase starts, which defines the mass of the unmixed zone, during real-time simulations. The unmixed zone size not only determines how well the in-cylinder

charge is mixed, which affects the start of HCCI combustion, but also the resulting peak in-cylinder pressure and temperature during the combustion process. The developed model was validated in the HIL simulation and experiments.

To achieve smooth combustion mode transition, the throttle position needs to be controlled accurately with fast response. In this dissertation, an electronic throttle control (ETC) system was modeled as an LPV (linear parameter varying) system in discrete-time domain, where the nonlinearities are modeled as varying parameter or compensated through feed-forward control. Mixed constrained H_2/H_∞ LPV controller was designed to achieve the best performance and also guarantee the system robustness. Then a model-based mode transition control strategy between SI and HCCI combustion was developed and experimentally validated for an HCCI capable SI engine equipped with electrical variable valve timing (EVVT) systems, dual-lift valves and ETC system. During the mode transition, a manifold air pressure controller was used to track the desired intake manifold pressure for managing the charge air; and an iterative learning fuel mass controller, combined with sensitivity-based compensation, was used to manage the engine torque in terms of net effective mean pressure, an indicator of engine output torque, at the desired level for smooth mode transition. Experiment results show that the developed controller is able to achieve smooth combustion mode transition with guaranteed robustness.

ACKNOWLEDGMENTS

This dissertation would not have been possible without the help of so many people. I would like to express my sincere appreciation to these who provided me guidance, support, encouragement, and also brought a lot of fun to my research and life.

I would like to express my deepest gratitude to my advisor, Dr. Guoming Zhu. It is my fortune and great privilege to do my research work under his continued support and excellent guidance. His comprehensive knowledge of control theory and automotive application inspired me to keep on pursuing and enriching my knowledge and experience. His systematic guidance encouraged me to improve the way of think and exploring. Besides, he also gave me generous encouragement for my future career and life, which is a lifetime of wealth!

I would like to express my appreciation to my committee members: Dr. Harold Schock, Dr. Hassan Khalil, and Dr. Jongeun Choi, for their discussions and insight comments during my dissertation work. Their wonderful graduate courses also provided me valuable knowledge and firm foundation for my research work, and brought me to the world of engine and control.

I would also like to say thanks to the graduate students and research assistants in the lab, who helped me set up the engine bench and run the experiments, even day and night: Xuefei Chen, Jerry Yang, Andrew Huisjen, Ruitao Song, Jie Yang, Tao Zeng, Yifan Men, Tom Stuecken.

Lastly, I am overly grateful for my parents' continued support and warm hearted solicitude that makes me full of courage to strive for the future.

TABLE OF CONTENTS

LIST OF TABLES

LIST OF FIGURES

CHAPTER 1

INTRODUCTION

1.1 Motivation

Homogeneous charge compression ignition (HCCI) combustion has been widely investigated in past decades, and demonstrated the potential of providing higher fuel thermal efficiency and lower emissions than those of the conventional spark ignition (SI) combustion. The un-throttled HCCI combustion significantly reduces the pumping loss, and the lean HCCI combustion results in relatively low in-cylinder flame temperature and has the advantage of reducing the level of NO_x emissions [1]-[5].

However, the operational range of the HCCI combustion is limited by knock (determined by the rate of in-cylinder pressure rise) at high load, and by combustion instability (partial burn or misfire) at low load as shown in Figure 1.1. Although the HCCI operational range could be enlarged to a certain extent as reported in [6] and [7], it will be able to cover the entire engine operational range. Therefore, it is important to have an HCCI capable SI engine that is able to operate at both SI and HCCI combustion modes under different operational conditions to take the advantages of both combustion modes; and smooth combustion mode transition is essential for the HCCI capable SI engine. Achieving smooth mode transition between the SI and HCCI combustion is challenging due to the significant thermal and charge mixture differences between

the HCCI and SI combustion. HCCI combustion requires un-throttled operation to reduce pumping loss, while the SI combustion operates in a throttled mode with relatively low manifold pressure, especially around the combustion mode transition region. Besides, in order to trigger the auto-ignition, HCCI combustion requires relatively high in-cylinder temperature at intake valve closing (IVC). The most common approach is to use the negative valve overlap (NVO) to trap high fraction of the hot residual gas from the previous cycle, where a variable timing valve-train is utilized. Then during the combustion mode transition, combustion control parameters such as fuel mass, air-to-fuel ratio, and EGR rate have to be well managed to achieve smooth combustion mode transition.

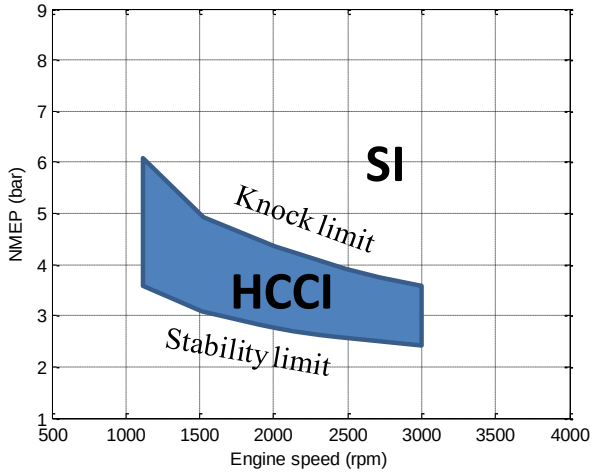

Figure 1. 1: Two-zone model architecture

1.2 Research Work

To realize stable HCCI combustion on an HCCI capable SI engine has many challenges, and this dissertation focuses on the smooth mode transition between SI and HCCI combustion. The engine been studied in this dissertation is a 2.0L four-cylinder engine equipped with electronic throttle, two-step valve lift and variable timing valve-train system. The engine is

capable of SI and HCCI combustion. Figure 1.2 shows the top-view of the engine with actuators. During the mode transition, these actuators have to be controlled separately. Firstly, the electronic throttle control (ETC) guarantees the throttle position acting between small opening (SI mode) and wide opening (HCCI mode) for the combustion modes requirement. Secondly, the electrical variable valve timing (EVVT) system achieves negative valve overlap (NVO) in HCCI mode to trap certain portion of residual gas to initiate auto-ignition by advancing the exhaust cam and retarding the intake cam in the few transition cycles. Thirdly, due to the different combustion characteristics of SI and HCCI modes, injected fuel mass and ignition timing have to be adjusted cycle by cycle during the mode transition, to achieve constant NMEP (net mean effective pressure, related to engine output torque). Normally the EVVT system has much less nonlinearities and external disturbances than ETC system, and an existing OCC (output covariance constraint) controller [8] was used to accurately regulate the intake and exhaust valve timings. This dissertation focuses on the electronic throttle control and NMEP control.

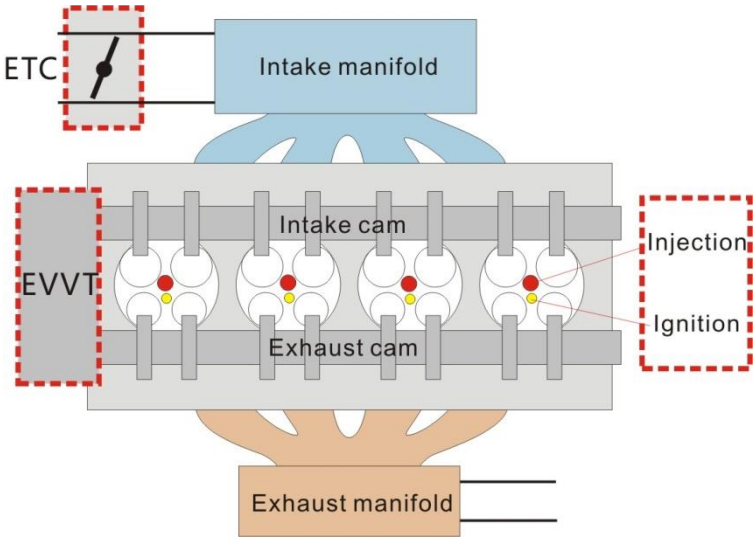

Figure 1. 2: HCCI capable SI engine

1.2.1 Engine modeling and HIL simulation

Nowadays for the purpose of reducing research cost and development duration, one of the most efficient approaches is to develop and validate the control strategy using an HIL (hardware-in-the-loop) simulation environment, where the real engine is replaced by a control-oriented real-time engine model.

To accurately control the HCCI combustion process, a precise charge mixing and combustion model is a necessity. Especially during the combustion mode transition, where the hybrid combustion mode most likely to occur, accurate auto-ignition timing prediction is essential for NMEP control. Widely used high fidelity engine models, such as GT-Power and WAVE, provide fairly accurate engine charge mixing and combustion simulations. However, they can only be used for off-line simulations and cannot be used for model-based control, where real-time HIL simulations are required. The mean-value models are simple and can run fast enough for real-time application; however, it can't provide detailed combustion information such as in-cylinder pressure and temperature, which are essential for control design and validation, especially for combustion feedback.

In this dissertation a control-oriented charge mixing and two-zone HCCI model was developed, based on thermodynamics and fluid dynamics, and it provides instantaneous in-cylinder pressure and temperature information for control purpose. By dividing the in-cylinder into mixed zone and unmixed zone, it provides a more accurate auto-ignition timing prediction, which is essential for hybrid mode combustion and mode transition control.

The HIL simulation is a powerful tool for control development. In this dissertation, the

dSPACE engine simulation system was used as the HIL simulator that runs the proposed engine model and communicates with the controller; that is, it provides various engine output signals based upon the control signals provided by the engine controller at different engine operational conditions. All the control strategies developed in this dissertation were validated in HIL simulation before experimental validation.

1.2.2 Electronic throttle control

Accurate control of electronic throttle motion is required in combustion mode transition to achieve desired air-to-fuel level. Around the mode transition region, where the engine load is usually low, the SI combustion is operated with relatively low manifold pressure and small throttle opening; while the HCCI combustion operates in an un-throttle mode with widely opened throttle. Hence, during the few transition engine cycles, the electronic throttle needs to be opened (from SI to HCCI) or closed (from HCCI to SI) in a relatively short duration. Furthermore, the transient response of throttle plate highly affects the manifold filling dynamics, and thereby affects the air-to-fuel ratio and combustion performance.

However, it is challenging to control the throttle plate accurately due to its nonlinearity caused by high nonlinear limp-home (LH) spring. The success of mode transition highly depends on whether the throttle plate can cross the LH position smoothly. Moreover, the intake air flow brings external disturbance to the electronic throttle system; especially when valve lifts change during mode transition, large additional torque caused by the pressure wave is applied to the throttle plate. In this dissertation an LPV gain-scheduling controller was designed to achieve the best performance, and also guarantee the robustness due to the external disturbance.

1.2.3 Combustion mode transition

It is fairly challenging to achieve smooth mode transition between the SI and HCCI combustion due to the significant thermal and charge mixture differences between the HCCI and SI combustion. Around the mode transition region, the SI combustion requires to be operated in a throttled mode with relatively low manifold pressure, while the HCCI combustion operates in an un-throttle mode to reduce pumping loss; furthermore, SI combustion operates with stoichiometric air-to-fuel ratio and PVO (positive valve overlap) which implies relatively low trapped residual gas ratio, while HCCI requires lean combustion and large amount of trapped residual gas. Therefore, it is essential to develop control strategies during the transition cycles to guarantee the smooth combustion mode transition between steady SI mode and HCCI mode without engine torque fluctuations.

Combustion mode transition has been widely investigated in recent years. Successful mode transition between SI and HCCI combustion within one engine cycle was reported by utilizing camless valve-train system including electromagnetic [9][10] and electro hydraulic [11] ones. However, camless valve-train system is difficult for commercial production due to its high cost, system complexity, and relatively lower reliability. In [12] an experimental investigation on SI-HCCI-SI mode transition using hydraulic two-stage profile camshafts with VVT (variable valve timing) system was performed, where the valve timing, one-step throttle opening timing, and fuel mass were optimized. However, considerable engine torque fluctuation during the combustion mode transition was observed. In [13] a state feedback controller was designed based on a state-space model obtained from system identification, fuel mass and NVO were used as the

control inputs to track the desired IMEP and combustion phasing. This model-based controller reduces torque fluctuation over the traditional PI (proportional and integral) controller, but engine torque output still varies unexpectedly, especially at the beginning of the mode transition.

Figure 1.3 shows three combustion mode transition cases from SI to HCCI at 1500rpm and 5.0 bar NMEP, including successful mode transition, unsuccessful mode transition and failed transition. For unsuccessful mode transition, significant NMEP can be observed which was possibly due to the inappropriate fuel mass or ignition timing. For failed mode transition, misfire or incomplete burning led to large drop of NMEP during the mode transition, and that might be caused by the ultra-lean combustion which was resulted from the inappropriate throttle opening.

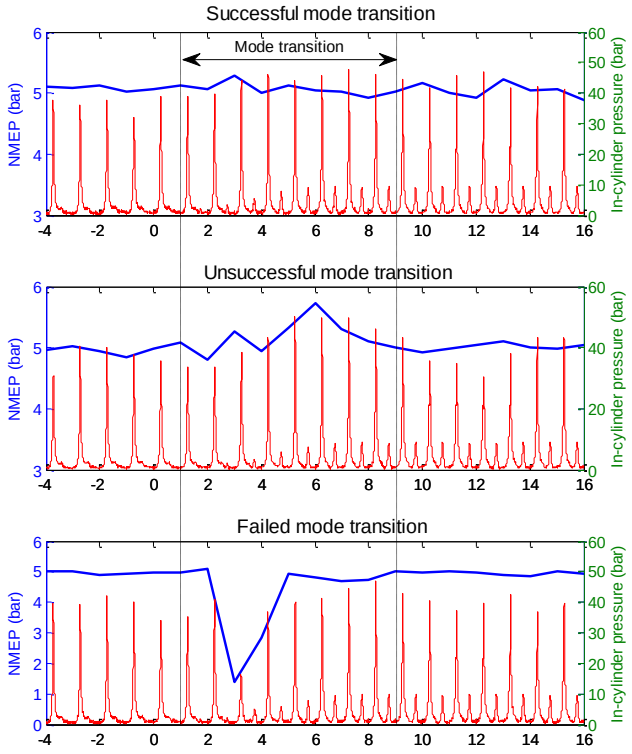

Figure 1. 3: Mode transition cases

In this dissertation, based on the actuator (ETC and EVVT) setup, a model-based control strategy was developed to achieve smooth mode transition between SI and HCCI combustion. This control strategy includes manifold pressure tracking control, iterative learning fuel mass control and sensitivity-based fuel mass compensator for improved robustness. The model-based controller was validated in HIL simulation first, with the developed two-zone control-oriented engine model, and then validated experimentally.

1.3 Dissertation Contributions

The dissertation has the following major contributions:

- A control-oriented charge mixing and two-zone HCCI combustion model was developed, which is able to predict the combustion timing with improved accuracy over the existing one-zone model. The improved flow dynamic modeling also guarantees the fidelity of the HIL simulations during the combustion mode transition. The model can be also used for other control developments, such as HCCI combustion control in future work.
- An LPV gain-scheduling control strategy for electronic throttle control dealing with the high system nonlinearity and external disturbance was developed and validated. This control approach can be also applied to other mechatronics or powertrain systems.
- The proposed control strategy to achieve smooth combustion mode transition is based upon manifold pressure control and fuel mass management. The iterative learning approach provided an efficient way for a wide operational range calibration, and the sensitivity-based feed-forward compensation can deal with certain type of cycle-by-cycle variation. The experimental results show that the maximum absolute variation during the model transition is compatible with that for

steady SI and HCCI combustion.

1.4 Dissertation outline

The material presented in this thesis is organized into three chapters. In chapter 2, a two-zone charge mixing and HCCI combustion model is proposed, and was implemented into the HIL simulation environment. The simulation results were compared with GT-Power simulation results and experimental data. It provides a simulation platform for developing the real-time mode transition control strategy. In chapter 3, a discrete-time gain-scheduling mixed constrained H_2/H_∞ controller is designed for an electronic throttle system, which can be controlled accurately and also robust to external disturbance during the combustion mode transition. In chapter 4, a model-based control strategy for combustion mode transition between SI and HCCI is proposed, and smooth transition was achieved both in HIL simulation end experimentally. Chapter 5 provides conclusions and future work.

CHAPTER 2

CONTROL-ORIENTED CHARGE MIXING AND TWO-ZONE HCCI COMBUSTION MODELING

2.1 Introduction

One challenge for the HCCI combustion control is to predict the start of combustion precisely. Moreover, HCCI combustion mode can only operate in a certain range of engine conditions and is limited at high engine load due to knock and low load due to misfire. Several approaches have been demonstrated to achieve auto-ignition combustion for an SI engine, such as intake charge heating, increasing the compression ratio, exhaust gas recirculation, and residual gas trapping that is achieved by negative valve overlap (NVO) [5], along with corresponding control strategies. Nowadays for the purpose of reducing research cost and shortening the development duration, one of the most efficient approaches is to develop and validate the control strategy using an HIL (hardware-in-the-loop) simulation environment, where the real engine is replaced by a control-oriented real-time engine model.

To accurately control the HCCI combustion process, a precise charge mixing and combustion model is a necessity. Widely used high fidelity engine models, such as GT-Power and WAVE, provide fairly accurate engine charge mixing and combustion models. However, they can only be used for off-line simulations and cannot be used for model-based control, where

real-time HIL simulations are required. Multi-zone models based on chemical kinetics, that divide the cylinder into adiabatic core zones and thermal boundary layers, are capable of simulating more realistic HCCI combustion phenomena [14][15]. Unfortunately, these models are not fast enough for real-time simulations. The mean-value single-zone method was used in [16] to model the averaged chemical kinetics and thermodynamic properties and a control-oriented modeling approach was used for multi-mode HCCI engine in [17].

In [18] a control-oriented one-zone HCCI combustion model was constructed based on the assumption that the in-cylinder fuel, air, and residual gas charges are uniformly premixed at the intake valve closing (IVC). However, during the engine intake process, some of the residual gas is not mixed with the fresh intake gas, which remains at certain position of the cylinder. This unmixed portion is so-called unmixed residual gas fraction. Ignoring the unmixed residual gas fraction will result in modeling errors for the peak in-cylinder pressure and temperature since the unmixed residual gas may have a quite different temperature compared with the well mixed zone. Also the volume and air-to-fuel ratio (AFR) of the mixed zone will be affected by the unmixed portion in the cylinder. During the gas exchange process described in [5], a first order transfer function was used to approximate the in-cylinder pressure, which led to large errors compared with the actual pressure. In [19] and [20] a two-zone HCCI model were established taking into consideration of unmixed zone during combustion phase. Reference [19] developed a two-zone model based on thermochemistry and chemical kinetics, which ensures better combustion results, but the charge mixing process is not modeled. As a result, the size of the unmixed zone cannot be determined in real-time. In [20] the unmixed zone was assumed to remain at the bottom of the

cylinder with a columnar intake flow jet, and the mass transfer rate from unmixed zone to mixed zone is proportional to the kinetic energy of the intake flow, which denoted that the charge mixing only occurs during the intake phase; however, this simplified model ignored the turbulent phenomenon caused by both of the bifurcated intake flow shear and high speed moving piston, which would last for the entire intake phase and compression phase.

In this article, to make the real-time simulation possible, mass fraction burned Wiebe function, along with energy conservation principle, was used to model the combustion process to guarantee the accuracy of thermodynamics characteristics such as in-cylinder pressure and temperature. One dimensional flow dynamics equations are used to model the detailed gas exchange dynamic process. During the intake phase, the in-cylinder charge is divided into two zones, mixed and unmixed zones, and modeled based upon the turbulent flow analysis approach.

This chapter is organized as follows. In section II the engine description and modeling framework are discussed. In section III detailed modeling approach is described for each combustion phase and simulation results are compared with GT-Power simulation results and experimental data in section IV. Section V addresses the conclusions.

2.2 Engine Description and Modeling Framework

The engine used for the modeling work is a 2.0L four-cylinder equipped with two-step valve lift and electrical cam phaser. The engine is capable of SI and HCCI combustion. Figure 2.1 shows the architecture of the entire engine model. Compared with the one-zone model in [18], it has the similar overall framework. The engine model receives inputs from the engine controller, including spark signal, injection signal, throttle signal, etc. The outputs of the engine model

include mean-value based crank shaft speed, exhaust pressure, crank based in-cylinder pressure, temperature, etc. Also, the engine crank, cam and gate signals are generated to synchronize with engine control unit for HIL simulations. The engine model consists of five subsystem models: combustion model, throttle and manifold model, EGR (exhaust gas recirculation) model, piston/crank dynamics and dyno model. Crank-based combustion related variables are updated every crank degree; and mean-value engine variables, including throttle, manifold model, crank and dynamometer models are updated with a fixed sample time at 1ms.

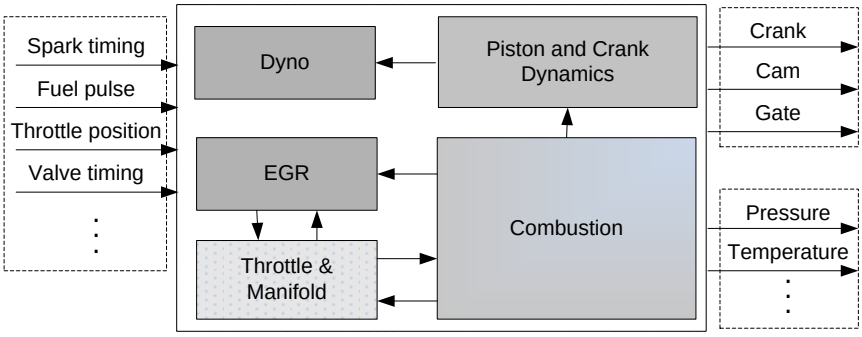

Figure 2. 1: Two-zone model architecture

However, one challenge for the HCCI combustion control is to predict the start of combustion precisely. Moreover, HCCI combustion mode can only operate in a certain range of engine conditions and is limited at high engine load due to knock and low load due to misfire. Several approaches have been demonstrated to achieve auto-ignition combustion for an SI engine, such as intake charge heating, increasing the compression ratio, exhaust gas recirculation, and residual gas trapping that is achieved by negative valve overlap (NVO) [5], along with corresponding control strategies. Nowadays for the purpose of reducing research cost and shortening the development duration, one of the most efficient approaches is to develop and validate the control strategy using an HIL (hardware-in-the-loop) simulation environment, where

the real engine is replaced by a control-oriented real-time engine model.

For the charge mixing process, the in-cylinder charge mixture is divided into two zones, mixed and unmixed, before the combustion starts. In order to predict the size of the unmixed zone, it is essential to model the flow dynamics during the entire intake process. A compressible flow dynamics method is used to predict the flow rate in real-time. When combined with turbulent diffusion analysis, the transfer rate between the two zones can finally be obtained. During the intake phase, due to the NVO recompression occurred before the intake phase, the in-cylinder pressure is usually higher than the intake manifold pressure at the start of the intake phase. Therefore, at the beginning of the intake process, the trapped in-cylinder gas flows from cylinder to manifold and then flow back to the cylinder. This intake process is considered in the model.

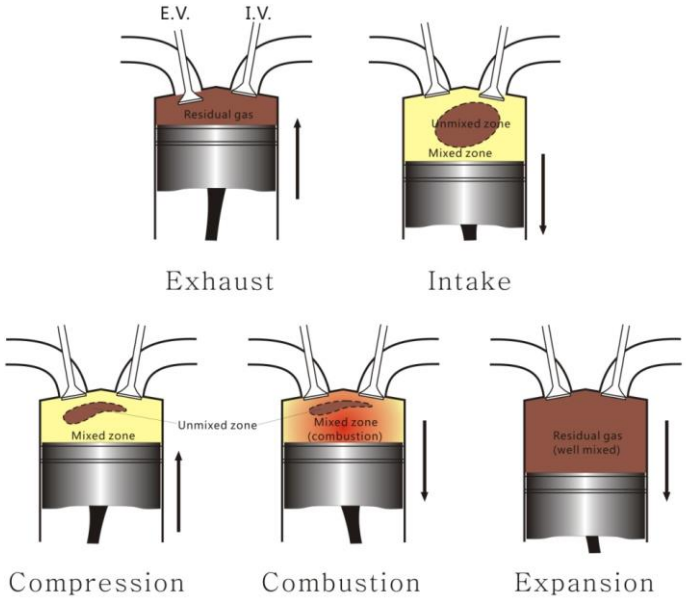

Figure 2. 2: Two-zone charge mixing and HCCI combustion model

Figure 2.2 shows a diagram of the two-zone mixing process over an entire engine cycle.

The unmixed zone is assumed to be located in the inner part of the cylinder, and its size is shrinking due to the gas diffusion to the mixed zone. Once auto-ignition occurs, it is assumed that the mass of unmixed zone does not change and a polytropic compression is assumed. When combustion ends, the two-zone assumption is not essential to in-cylinder analysis, hence it is assumed that the in-cylinder residual gas distributes homogeneously. Since the calculated temperature and volume of the unmixed zone can be updated each crank degree under this assumption, it is easy to analyze the combustion process in the mixed zone. In this article, it is also assumed that there is no heat exchange between the two zones, but the mixed zone exchanges heat with the cylinder wall.

2.3 Two-zone Charge Mixing and Combustion Model

The thermodynamic characteristics of the in-cylinder gas, such as in-cylinder pressure and temperature, are of great interest in the SI and HCCI combustion modeling research. This is especially important at certain critical combustion phases such as the IVC (intake valve closing).

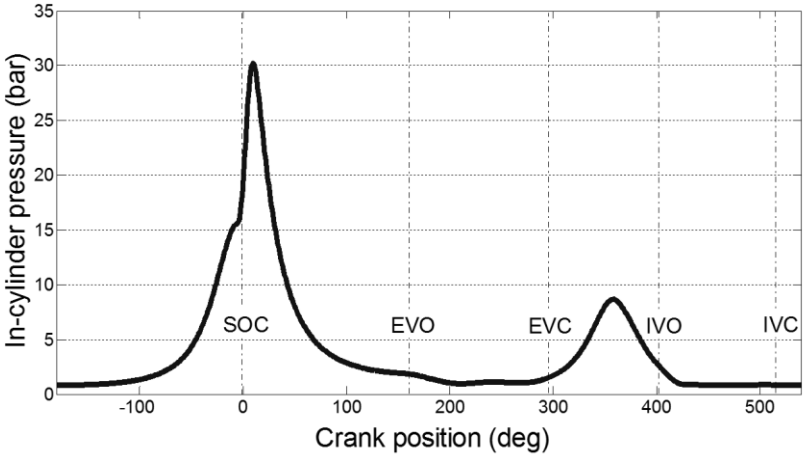

Figure 2. 3: Two-zone charge mixing and HCCI combustion model

Figure 2.3 shows five key combustion phases of an HCCI combustion process within one

engine cycle. They are: intake valve closing; start of HCCI combustion (SOC); exhaust valve opening (EVO); exhaust valve closing (EVC); and intake valve opening (IVO). For each combustion phase, the in-cylinder combustion variables, such as pressure and temperature are modeled using thermodynamic governing partial differential equations that are discretized every crank degree and solved analytically. For the HCCI combustion process, Wiebe based mass fraction burned (MFB) function, calibrated using experimental data, was used to approximate the complicated chemical reaction process to make the real-time simulation possible with required simulation accuracy; for the gas exchange process, the discretized governing equations (2.6) and (2.8) were solved iteratively, along with 1-D flow dynamics equations, with the guaranteed convergence for in-cylinder thermodynamics characteristics. In the rest of this section, crank resolved model of each combustion phase are presented.

2.3.1 Intake phase

During this phase, the fresh charge enters the cylinder and mixes gradually with the residual gas. As a result, the total mass of the unmixed zone reduces. The goal is to predict the size of the unmixed zone at IVC; hence, it is essential to model the flow dynamics during the entire intake phase. Calculation of the intake flow rate is based on the one-dimensional compressible flow equations [21]:

a) When the flow is not choked ($P_T/P_0 > \left[2/(\gamma+1)\right]^{\gamma/(\gamma-1)}$),

$$\dot{m}_v = \frac{C_D A_v P_0}{\sqrt{RT_0}} \left(\frac{P_T}{P_0}\right)^{1/\gamma} \left\{ \frac{2\gamma}{\gamma-1} \left[1 - \left(\frac{P_T}{P_0}\right)^{(\gamma-1)/\gamma} \right] \right\}^{1/2} \tag{2.1}$$

b) When the flow is choked ($P_T/P_0 \le \left[2/(\gamma+1)\right]^{\gamma/(\gamma-1)}$),

$$\dot{m}_v = \frac{C_D A_v P_0}{\sqrt{RT_0}} \gamma^{1/2} \left(\frac{2}{\gamma+1}\right)^{(\gamma+1)/2(\gamma-1)} \tag{2.2}$$

where C_D is the discharge coefficient and experimentally determined, P_0 and T_0 are the upstream stagnation pressure and temperature, P_T is the downstream pressure, A_v is the intake valve reference area, and γ is the specific heat ratio.

For an HCCI combustion engine with the NVO strategy, most often, the in-cylinder pressure is higher than the intake manifold pressure at the IVO due to the residual gas recompression and early exhaust valve closing. Hence, a certain portion of the residual gas will escape into the manifold after IVO. This is called backflow. In order to simplify the modeling process, the entire intake phase is divided into three stages under certain assumptions:

Firstly, right after the IVO, the trapped residual gas flows out of the cylinder through the intake valve. In this case, P_0 and T_0 in (2.1) and (2.2) are in-cylinder pressure and temperature, respectively, P_T is the manifold pressure, and $\dot{m}$ is treated as a negative value in the model for calculation convenience. During this stage, as the in-cylinder total mass is decreasing while the cylinder volume is increasing, the in-cylinder pressure and temperature both drop significantly.

Secondly, once the in-cylinder pressure becomes lower than the intake manifold pressure, the flow direction reverses. It is assumed that the escaped residual gas in the first stage was not mixed with the fresh charge in the manifold. Since the GT-Power and CFD (computational fluid dynamics) simulation results show that the back flow occurred during the first stage will be charged back into the cylinder completely. Therefore, this assumption will not lead to large

modeling error at the end of the charge mixing process. For equations (2.1) and (2.2), in this case, P_0 is the manifold pressure, P_T is the in-cylinder pressure, and T_0 is the residual gas temperature reduced by a factor governed by heat transfer and expansion.

Finally, after all the escaped residual gas flows back into the cylinder, the actual fresh charge process begins. During this stage, P_0 and T_0 are the intake manifold pressure and temperature, respectively, and P_T is the in-cylinder pressure. This stage has the longest duration among the three stages. Mixing occurs in this stage.

The calculation of in-cylinder pressure and temperature is based upon the first law of thermodynamics. Since there is only one-direction flow path at one time due to the NVO operation, the energy conservation equation can be written as

$$\frac{d(mu)}{dt} = \dot{Q}_w - \dot{W} + \dot{m}h \tag{2.3}$$

where $\dot{W}$ is the rate of the transferred work, which equals $p\dot{V}$. $\dot{Q}_w$ is the total heat-transfer rate to the cylinder walls, which can be obtained using the Woschni correlation model [22][23]:

$$\dot{Q}_w = -A_c h_c \left(T - T_w\right) / N_e \tag{2.4}$$

where A_c is the contact area between gas and cylinder wall, T_w is average temperature of cylinder wall, N_e is the engine speed, and h_c is the instantaneous convection coefficient that can be calculated by

$$h_c = \alpha B^{-0.2} P^{0.8} T^{-0.55} \left[C_1 \bar{S}_p + C_2 \frac{V_d T_r}{p_r V_r} \left(P - P_{mot}\right) \right]^{0.8} \tag{2.5}$$

where B is the bore; P is the in-cylinder pressure; $\bar{S}_p$ is the mean piston speed; V_d is the displaced volume; T_r, p_r, and V_r are the in-cylinder temperature, pressure and volume at some

reference state, such as intake valve closing; and P_{mot} is the motored in-cylinder pressure at the current crank position. α , C_1 and C_2 are the scaling factors used as model calibration parameters. To simplify calculation, it is assumed that h_c is constant within the calculation step but variable step-by-step.

In the developed model equation (2.3) is discretized and solved analytically. Note that C_p and C_v do change as a function of temperature and species. However, within one computational step (one crank degree) the variations of C_p and C_v are fairly small. To simplify calculation, it is assumed that C_p and C_v are constant within the calculation step but variable step-by-step. It is also assumed that the pressures in mixed and unmixed zones are identical. Then the in-cylinder temperature can be determined at every crank degree by the following equation

$$T(\theta_i) = \frac{Q_w - P(\theta_{i-1})\left[V(\theta_i) - V(\theta_{i-1})\right] + \dot{m}\Delta t C_p T_0 + m(\theta_{i-1}) C_v T(\theta_{i-1})}{\left[m(\theta_{i-1}) + \dot{m}\Delta t\right] C_v} \tag{2.6}$$

where θ is crank angle; T_0 is the intake flow temperature; Δt is the time interval for each crank degree; and Q_w is the heat transfer to the cylinder wall during the time interval, which can be obtained by

$$Q_w = \dot{Q}_w\left(\theta_{i-1}\right)\Delta t \tag{2.7}$$

based on the assumption that the heat transfer rate remains unchanged within one calculation step.

Since the mixture can be considered as an ideal gas, in-cylinder pressure can be obtained by

$$P(\theta_i) = \frac{m(\theta_i) R T(\theta_i)}{V(\theta_i)} \tag{2.8}$$

Equations (2.1) and (2.2) are discretized at each crank step and solved numerically, where

the solution is obtained using iterative approach for a given step, along with (2.6) and (2.8). In-cylinder pressure, temperature and intake flow rate are updated at each iteration. During the third phase of the process, the residual gas mixes with the fresh charge gradually in a fairly complicated dynamic process. The main task of the modeling work is to describe the mass transfer rate from the unmixed zone to the mixed zone using a simple approach, which is solvable in real-time for HIL simulations.

Due to the high intake flow velocity and piston motion, there is significant in-cylinder turbulent motion, combined with tumble and swirl. The flow field changes significantly as manifold shape, combustion chamber geometry and valve timing vary. CFD models were widely used to provide the relatively accurate estimation of in-cylinder gas motion [24][25]. Figure 4 shows a side view of a simulated charge mixing process with NVO. The entire process can be considered as a turbulent diffusion process. Figure 2.4 (a) shows that at the beginning of the third stage, as discussed previously, the fresh charge comes in, and bifurcates into two jets; the right jet flows along the cylinder wall towards the piston, and the left jet flows along the cylinder head and past the exhaust valve. As the valve lift increases, additional incoming fresh charge leads to faster in-cylinder flow velocity and turbulent intensity, and forms two main vortices: the left-top vortex caused by the shear between the left jet and cylinder wall, and the right-bottom vortex caused by the interaction between the right jet and piston, as shown in Figure 2.4 (b). The mass transfer from residual gas to well-mixed gas, resulting from the species gradient between fresh charge and residual gas, is augmented by this in-cylinder turbulence. Once the intake valve is about to close and the piston is approaching to BDC (bottom dead center), the in-cylinder

average flow velocity drops, but turbulence keeps the process going albeit at a decreasing rate, as shown in Figure 2.4 (c). When the piston moves up towards the TDC (top dead center), it pushes the residual gas to the upper location of the cylinder, and a newly formed vortex is conducive to charge mixing, as shown in Figure 2.4 (d).

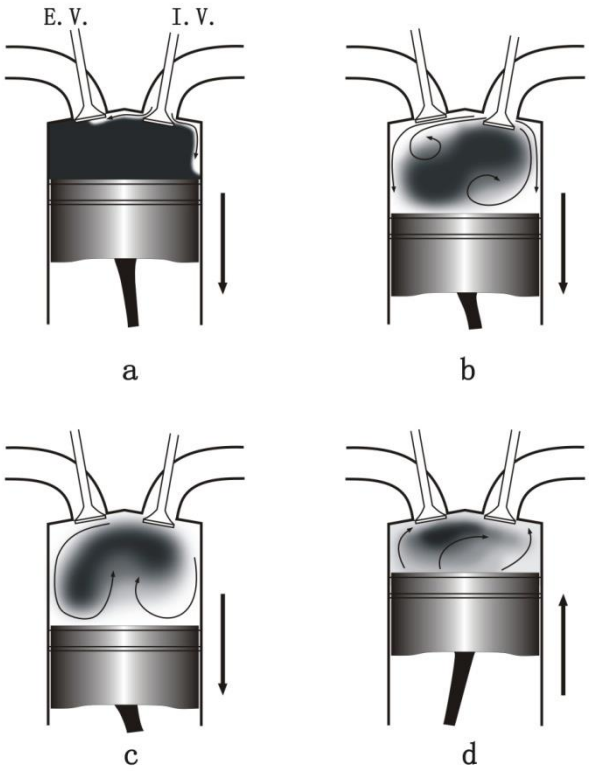

Figure 2. 4: Charge mixing process

Based on the CFD simulation results [24][25], although different valve timing strategies will lead to different flow fields and residual gas shapes, the shape of the unmixed zone formed by the residual gas is similar. In most of the cases, the residual gas is surrounded by the mixed charge due to continuous shear flow. Hence a simplified model is proposed in Figure 5.

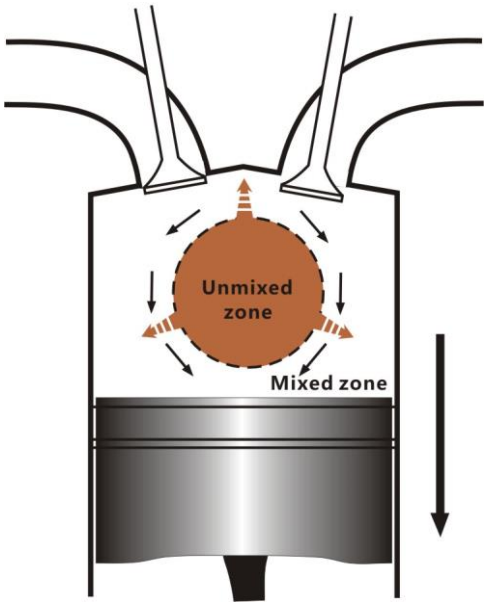

Figure 2. 5: A simplified charge mixing model

It is assumed that during the charge mixing process the unmixed zone (formed by residual gas) remains in the center of the cylinder, and the shape is assumed to be spherical. The fresh charge surrounds the unmixed zone with velocity tangent to the sphere and mixes with the residual gas gradually, which forms the mixed zone. The mass transport from the unmixed zone to mixed zone is caused by gas diffusion, which consists of both molecular diffusion and turbulent diffusion. Since the turbulent diffusion rate is much higher than that of molecular diffusion, the latter is ignored. Under this assumption Fick's first law of diffusion will be applied [26]:

$$j_t = -\rho \mathcal{D}_t \frac{d\omega}{dr} \tag{2.9}$$

where j_t is the turbulent mass flux of the residual gas; ρ is the density of the residual gas; $\mathcal{D}_t$ is the turbulent diffusivity and the last term describes the mass fraction of the residual gas distribution in the mixed zone in the radius direction. This mass flux denotes the mass flow rate

from unmixed zone to mixed zone per unit interaction area per unit time. To simplify the problem, it is assumed that at any time the residual gas in the mixed zone has a constant distribution gradient, hence the last term can be rewritten as $-\omega_0/l$, where ω_0 is the concentration of residual gas at the interaction surface and l is the thickness of mixed zone. The relationship between turbulent diffusivity and turbulent viscosity leads to the following equation that can be used to solve $\mathcal{D}_t$:

$$Sc_t = \frac{\nu_t}{\mathcal{D}_t} \tag{2.10}$$

Here, Sc_t is a dimensionless constant known as the turbulent Schmidt number. The turbulent viscosity can be obtained by:

$$\nu_t = c_1 \bar{v} \tag{2.11}$$

where $\bar{v}$ is the average velocity in the mixed zone, which is approximated by mean value of intake flow velocity and piston velocity; l is the thickness of the mixed zone, the same as in residual gas distribution gradient calculation; and c_1 is a constant to be calibrated. Finally the mass transfer rate can be expressed as

$$\dot{m}_{tr}(\theta_i) = \rho(\theta_i) c_1 \bar{v}(\theta_i) \omega_0 c_2 A(\theta_i)/Sc_t \tag{2.12}$$

where A is the surface area of the unmixed zone, which can be easily calculated under the "sphere" assumption; and c_2 is a calibration constant due to the assumptions made. Notice that at the beginning of the charge mixing process, the amount of the incoming fresh charge is not enough to surround the residual gas, and in this case A should be the surface area of the mixed zone and calculated by assuming that the thickness of the mixed zone is identical to the intake

valve lift.

Notice that during the entire intake phase temperature gradient exists between two zones, resulting in heat transfer from the unmixed zone to the mixed zone. Hence a polytropic process can be approximated in the unmixed zone, and the polytropic exponent *n* was calibrated as a function of temperature to match the GT-Power simulation results over a wide engine operation range. Then the temperature in both zones can be obtained sequentially, assuming that the pressures of the mixed and unmixed zones are identical:

$$T(\theta_i)_{unmixed} = T(\theta_{IVO}) \cdot \left(\frac{P(\theta_{IVO})}{P(\theta_i)} \right)^{n-1/n} \tag{2.13}$$

$$T(\theta_i)_{mixed} = \frac{m(\theta_i)T(\theta_i) - m_{unmixed}(\theta_i)T(\theta_i)_{unmixed}}{m_{mixed}(\theta_i)} \tag{2.14}$$

The volume of both zones can be determined by ideal gas law.

Since the developed model is capable of SI and HCCI combustion modes, the modeling methodology described above can be also used for the positive valve overlap (PVO) case. Similar analysis can be used during the intake valve opening and exhaust valve closing; however, during the valve overlap stage, complicated in-cylinder mixing process exists. Due to the strong in-cylinder motion (combination of turbulence and tumble) after intake valve opening, it is assumed that intake fresh charge will not get out through the exhaust valve, that is, there is no fresh charge flow into the exhaust port. This assumption is due to the fact that under most engine operational conditions there is no fresh charge escaped through the exhaust valve. Hence the intake charge mixing process and residual gas exhaust process can be calculated separately. Note that in some case the backflow phenomenon does exist, including flow from cylinder to intake

manifold, and flow from exhaust manifold to cylinder. Similar criteria and method can be applied to this case as in the first two stages mentioned above.

2.3.2 Compression phase

Since at the end of compression phase the in-cylinder temperature might be very high, the heat transfer effect cannot be neglected to achieve an accurate prediction of the start of HCCI combustion. Based on energy conservation, temperatures of both mixed and unmixed zones can be calculated separately:

$$T(\theta_i)_{unmixed} = \frac{m_{unmixed}(\theta_{i-1})C_v T_{unmixed}(\theta_{i-1}) - P(\theta_{i-1})\Delta\bar{V}(\theta_i) - \dot{m}_{tr}(\theta_i)\Delta t C_p T(\theta_i)_{unmixed}}{\left[m_{unmixed}(\theta_{i-1}) - \dot{m}_{tr}(\theta_i)\Delta t\right]C_v} \quad (2.15)$$

$$T(\theta_i)_{mixed} = \frac{Q_{mixed} - P(\theta_{i-1})\Delta\hat{V}(\theta_i) + m_{mixed}(\theta_{i-1})C_v T_{mixed}(\theta_{i-1}) + \dot{m}_{tr}(\theta_i)\Delta t C_p T(\theta_i)_{unmixed}}{\left[m_{mixed}(\theta_{i-1}) + \dot{m}_{tr}(\theta_i)\Delta t\right]C_v} \quad (2.16)$$

where

$$\Delta\bar{V}(\theta_i) = \left[V_{unmixed}(\theta_i) - V_{unmixed}(\theta_{i-1})\right],\ \Delta\hat{V}(\theta_i) = V_{mixed}(\theta_i) - V_{mixed}(\theta_{i-1})$$

Note that Q_{mixed} is heat transfer to the cylinder walls from the mixed zone; and $\dot{m}_{tr}$ is the mass transfer rate from unmixed zone to mixed zone that can be obtained by (2.12). Heat transfer between mixed zone and unmixed zone is neglected here. Then, the average in-cylinder temperature can be obtained by

$$T(\theta_i) = \frac{m_{mixed}T(\theta_i)_{mixed} + m_{unmixed}T(\theta_i)_{unmixed}}{m_{IVC}} \quad (2.17)$$

The compression phase ends when the HCCI combustion starts. A commonly used criterion for the start of combustion (SOC) timing is the Arrhenius integral [27][28], that depends on the oxygen and fuel concentration, which is described as

$$ARI = \int_{\theta_{IVC}}^{\theta_i} Ap^a \left[O_2\right]^b \left[Fuel\right]^c e^{-\frac{E_a}{R \cdot T_{mixed}(\theta)}} d\theta \tag{2.18}$$

where E_a is the activation energy for the auto ignition reaction and is chosen to be a constant; and A is a scaling factor related to fuel composition. Since for NVO strategy EGR rate has a strong effect on ignition delay [29], A is also a function of EGR, and a lookup table can be used to calibrate A.

The SOC crank position is defined as the crank angle for 1% fuel burned under HCCI combustion. During this phase, the Arrhenius integral continues its integration. As the in-cylinder temperature and pressure increase gradually due to compression, the Arrhenius integral increases as well. Once the *ARI* reaches criteria of the SOC ($ARI \geq 1$), it shows that the HCCI combustion phase starts. At this moment, the temperature of mixed zone will be recorded as $T(\theta_{SOC})$ and volume of unmixed zone as $V_{unmixed}(\theta_{SOC})$ to be used for calculation in the next phase.

2.3.3 Combustion and expansion phase

In the HCCI combustion phase, the following two assumptions are made:

1) There is no mass exchange between the mixed (burned) and the unmixed zones due to the weak in-cylinder gas motion during the combustion phase (near TDC).

2) There is no heat transfer between the two zones but each zone has heat transfer to the cylinder wall.

Under the two assumptions, thermodynamic activity in both zones can be solved separately. In order to simplify the coupled equations, in-cylinder pressure in the last crank degree is used to

calculate the volume of the current unmixed zone.

$$V_{unmixed}(\theta_i) = V_{unmixed}(\theta_{SOC}) \left[\frac{P(\theta_{SOC})}{P(\theta_{i-1})} \right]^{1/\gamma} \tag{2.19}$$

In the mixed zone, the fuel MFB is modeled based upon the Wiebe MFB function and associated heat release rate function. Experimental results show that the heat release rate curve for HCCI combustion varies significantly and is heavily dependent on the fuel types and engine operational conditions. Typically the combustion process can be divided into two stages, cool-flame reactions and main combustion [30][31]. Under certain lean combustion cases, especially with very high EGR rate (combined with both NVO trapped residual mass and external EGR), or highly diluted mixture case (high N_2 concentration or low fuel concentration), the main HCCI combustion stage can be further divided into two stages: fast reaction (heat release) rate stage and slow reaction rate stage [32][33], as shown in Figure 2.6. In order to develop a generic combustion model that can be applied to all types of four-stroke SI and CI engines, a generalized formula for MFB curve, that covers most possible combustion processes, is modeled by a combination of three functions

$$x(\theta) = \alpha x_1(\theta) + \beta x_2(\theta) + (1-\alpha-\beta) x_3(\theta) \tag{2.20}$$

and each of these three functions is modeled by the Wiebe function [21] with ($\alpha \geq 0,\ \beta \geq 0,\ \alpha+\beta \leq 1$)

$$x_i(\theta) = 1 - e^{-a_i \left(\frac{\theta-\theta_{0i}}{\Delta\theta_i} \right)^{m_i+1}}, \quad i = 1,2,3 \tag{2.21}$$

where coefficients a_i, m_i, factors α, β, and predicted burn duration $\Delta\theta_i$ are calibration

parameters of engine speed and load, and coolant temperature; θ_{0i} represents the start of combustion for the stage i; and $\theta_{01} = \theta_{SOC}$ is given by the Arrhenius criterion in (18). All these parameters were calibrated within certain engine operation condition range and lookup tables were used as functions of engine speed and air-to-fuel ratio. For the combustion with relatively low EGR rate and not extremely lean combustion the third combustion stage does not exist and $\alpha + \beta$ can be set to one; and for gasoline type fuels combustion where the cool-flame reaction is not evident α can be set to one and β to zero

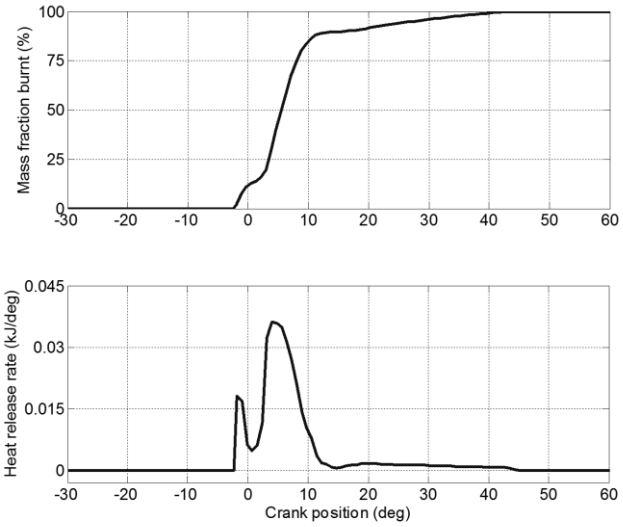

Figure 2. 6: HCCI combustion mass fraction burnt and heat release rate

The energy conservation equation applied to the mixed zone has the form

$$m_{mixed}\frac{du}{d\theta} + p\frac{dV}{d\theta} + Q_w = \eta_{HCCI} m_{fuel} Q_{LHV}\frac{dx}{d\theta} \tag{22}$$

where the combustion efficiency η_{HCCI} is a calibration parameter used to match the simulated IMEP (indicated mean effective pressure) provided by GT-Power model, and Q_{LHV} is the low heating value of the fuel. Considering the time interval for each crank degree is fairly small, the temperature calculation was simplified into two steps shown in (2.23) to make real-time

simulation possible. They are a polytropic volume change process without heat exchange and a heat exchange process without volume change, where in the numerical simulations parameter *n* is equal to γ. Then the temperature, pressure and volume of mixed zone can be solved by

$$T_{mixed}(\theta_i) = T_{mixed}(\theta_{i-1}) \cdot \left(\frac{V_{mixed}(\theta_{i-1})}{V_{mixed}(\theta_i)} \right)^{n-1} + \frac{\eta_{HCCI} m_{fuel} Q_{LHV} \left[x(\theta_i) - x(\theta_{i-1}) \right] - Q(\theta_i)}{m_{mixed} C_v} \tag{2.23}$$

$$P(\theta_i) = P(\theta_{i-1}) \cdot \frac{V_{mixed}(\theta_{i-1})}{V_{mixed}(\theta_i)} \cdot \frac{T_{mixed}(\theta_i)}{T_{mixed}(\theta_{i-1})} \tag{2.24}$$

and

$$V_{mixed}(\theta_i) = V(\theta_i) - V_{unmixed}(\theta_i) \tag{2.25}$$

Temperature in the unmixed zone can be obtained by (2.15).

After the HCCI combustion phase, the two-zone analysis is no longer essential for in-cylinder combustion behavior, and the two zones are assumed to be well mixed instantaneously. The in-cylinder average temperature can be obtained by (2.13) with the initial condition:

$$T(\theta_e) = \frac{m_{mixed} T(\theta_e) + m_{unmixed} T_{unmixed}(\theta_e)}{m_{IVC}} \tag{2.26}$$

where the index *e* denotes the crank position when combustion terminates.

2.3.4 Exhaust phase

The exhaust process is similar to the intake phase. Equations (2.1), (2.2), (2.6) and (2.7) are used for calculating the exhaust flow rate, in-cylinder temperature and pressure. Note that during this phase the in-cylinder pressure is higher than the exhaust manifold pressure in most of time, however, the situation can be reversed. Therefore, the backflow occurring is also considered. At

the exhaust valve closed (EVC), the trapped mass can be calculated by

$$m_{EVC} = \frac{P_{EVC} V_{EVC}}{R T_{EVC}} \tag{2.27}$$

2.3.5 NVO phase

The NVO phase is called as engine recompression. During this phase the trapped in-cylinder gas is polytropically compressed or expanded in a closed system with heat transfer to the cylinder wall, so (2.28) and (2.8) are used to calculate both temperature and pressure with $m(\theta_i)$ replaced by m_{EVC} in (2.8).

$$T(\theta_i) = T(\theta_{i-1}) \cdot \left(\frac{V(\theta_{i-1})}{V(\theta_i)} \right)^{n-1} \tag{2.28}$$

2.3.6 Throttle and manifold model

Throttle and intake manifold models provide the manifold pressure required for intake flow rate calculation in real-time. The fresh air flow rate through the throttle plate can be calculated using the one-dimensional compressible flow equation similar to the one used to solve intake valve case:

$$\dot{m}_t = \frac{C_d A_t P_0 \sqrt{2\gamma/(\gamma - 1)}}{\sqrt{R T_0}} \Psi(p_r) \tag{2.29}$$

where C_d is the discharge coefficient; P_0 and T_0 are the atmosphere pressure and temperature; A_t is the throttle reference area; and $p_r = p_{man}/p_0$ where p_{man} denotes the manifold pressure. The function Ψ is given by

$$\Psi(p_r)=\begin{cases}\sqrt{p_r^{\frac{2}{\gamma}}-p_r^{\frac{\gamma+1}{\gamma}}} & , \quad \text{if } p_r \geq \left(\frac{2}{\gamma+1}\right)^{\frac{\gamma}{\gamma-1}} \\ \sqrt{\left(\frac{\gamma-1}{2\gamma}\right)\left[\frac{2}{\gamma+1}\right]^{\frac{\gamma+1}{\gamma-1}}}, & \text{if } p_r < \left(\frac{2}{\gamma+1}\right)^{\frac{\gamma}{\gamma-1}}\end{cases} \tag{2.30}$$

Considering the throttle geometry, A_t can be approximated by

$$A_t = \frac{\pi}{4} D^2 \left[1-\cos\left(\alpha-\alpha_0\right)\right] \tag{2.31}$$

where D is the diameter of the throttle plate, and α_0 is the closed throttle angle.

Actual flow dynamics and thermodynamics in the manifold are quite complicated. In order to simplify the problem, a uniform condition assumption for the manifold is made, which assumes that there is no pressure gradient or temperature gradient in spatial distribution. By choosing the entire manifold as the control volume and applying the mass conservation, the mass change in the manifold is the difference between inlet mass flow (combined with air mass flow past the throttle and external EGR flow) and outlet mass flow (flow enter the cylinder through the valves). Then the equation for manifold mass change rate can be expressed as

$$\dot{m}_{man} = \dot{m}_t + \dot{m}_{EGR} - \dot{m}_v \tag{2.32}$$

Applying the ideal gas law in the manifold volume V, the pressure differential equation can be written as

$$\dot{p}_{man} = \frac{\dot{m}_{man} R T_{man}}{V} \tag{2.33}$$

Neglect the different gas thermodynamic properties between fresh air and EGR, the difference equation for manifold temperature is

$$\begin{aligned}&[T_{man}(\theta_i)m_{man}(\theta_i) - T_{man}(\theta_{i-1})m_{man}(\theta_{i-1})]C_{v,man} = \\ &\quad \left[T_0 \dot{m}_t\left(\theta_i\right)C_{v0} + T_{EGR}\dot{m}_{EGR}\left(\theta_i\right)C_{v,EGR} - T_{man}(\theta_{i-1})\dot{m}_v(\theta_i)C_{v,man}\right]\Delta t\end{aligned} \tag{2.34}$$

where Δt is the time interval for each crank degree. Then equations (2.32) and (2.33) can be discretized, along with (2.29) and (34), p_{man} and T_{man} can be solved online iteratively, which is similar to solving equations (2.1) – (2.8).

2.4 Simulation Results

The two-zone HCCI combustion model was validated in the HIL simulation environment (see Figure 2.7 for the HIL system architecture). On top of the figure a host computer is used for running the Opal-RT based engine controller; the lower host computer is used for running the dSPACE based real-time engine simulator which was introduced in this paper. The two host computers can communicate with each other to get all the data updated each crank angel to achieve the real-time simulation. An oscilloscope can be applied to display the simulation results.

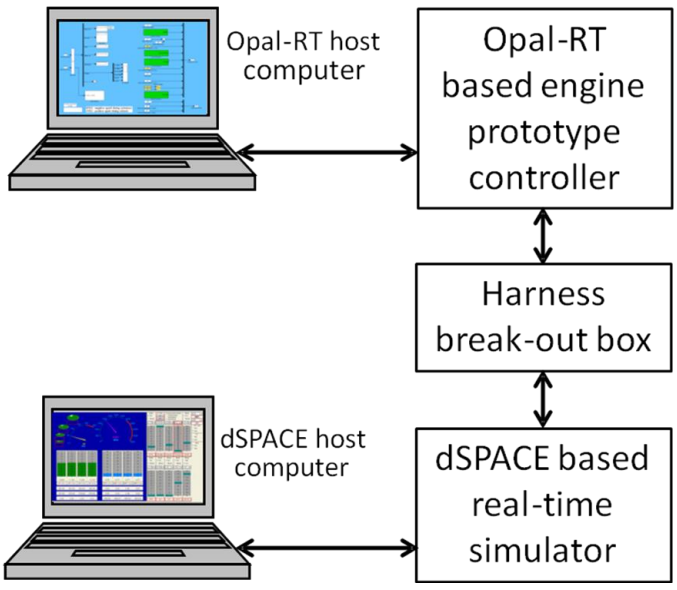

Figure 2. 7: HIL simulation environment

Table 2. 1: Engine Specifications

Parameter	Model value
bore/stroke/con-rod length	86mm/86mm/143.6mm
compression ratio	9.8:1
intake valve opening duration	148 crank degree
exhaust valve opening duration	148 crank degree
Intake/exhaust valve lifts	5mm

The engine parameters are given in Table 2.1, and Table 2.2 shows the model calibration parameters and how they are calibrated.

Table 2. 2: Calibration Parameters

Parameter	Equations	Calibration method
C_D	(1), (2), (29)	GT-Power
α, C_1, C_2	(5)	GT-Power
c_1, c_2	(11), (12)	Experiment
n	(13), (23), (28)	GT-Power
A, a, b, c	(18)	Experiment
α, β	(20)	Experiment

The two-zone model was validated for the engine operation at 2000 rpm with various loads. The simulation results at 4.2 bar IMEP are presented below. The associated valve timing for EVO, EVC, IVO and IVC are 156°, 304°, 382°, and 530° after TDC (top dead center). A four-cylinder GT-Power model is also developed and used to provide baseline simulation results, and Figure 2.8 shows the architecture of the model. For the purpose of validation, the proposed two-zone charge mixing and combustion model was compared with the one-zone model in [13], along with the improved one-zone model where the gas exchange flow dynamics was included but with the assumption of homogeneous mixing during the entire gas exchange process.

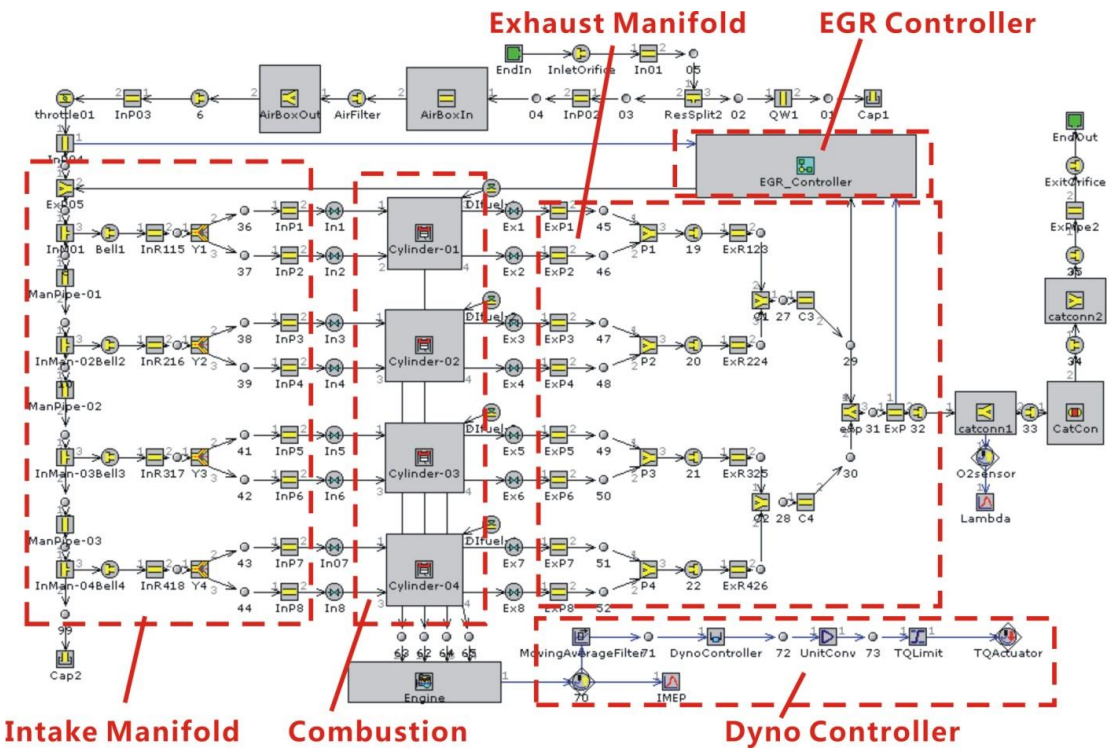

Figure 2. 8: GT-Power engine model diagram

Figures 2.9 and 2.10 show the in-cylinder pressures and temperatures over an engine cycle. Note that the two-zone charge mixing model can provide an accurate simulation results that match with GT-Power simulation results quite well.

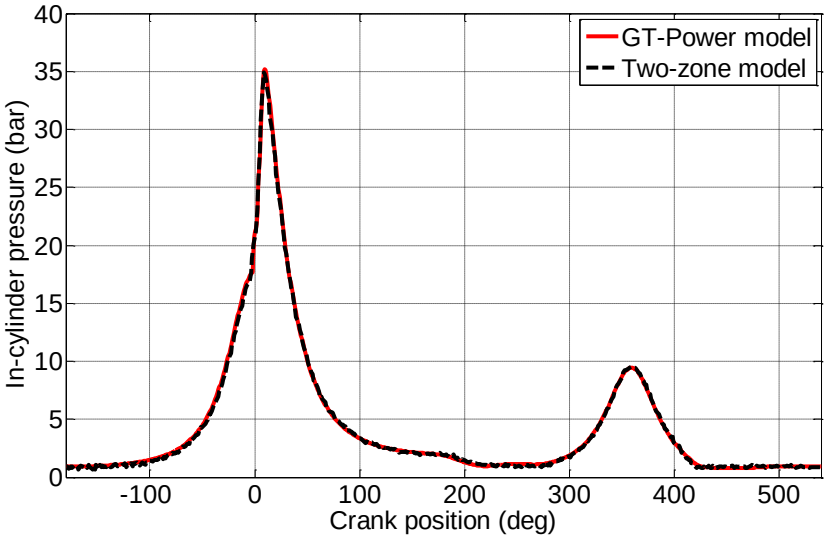

Figure 2. 9: In-cylinder pressure comparison.

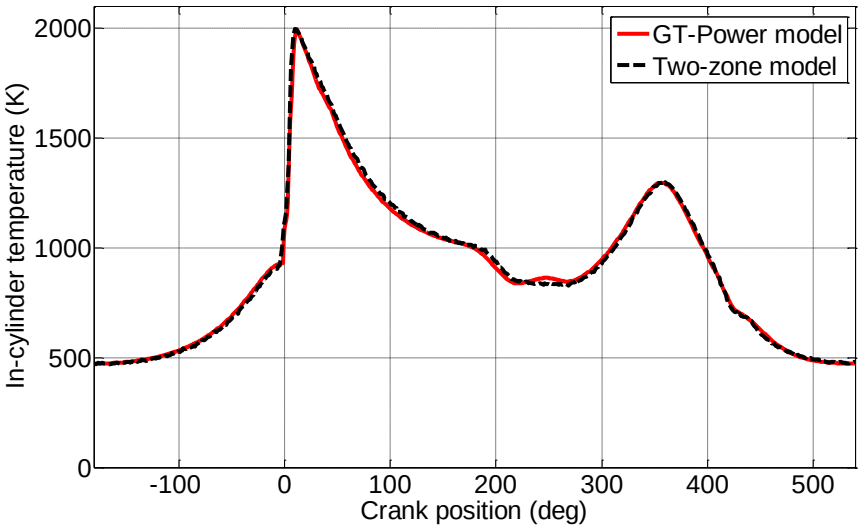

Figure 2. 10: In-cylinder temperature comparison.

Figures 2.11 and 2.12 show the in-cylinder pressures and temperatures during the gas exchange process. Compared with one-zone model without fluid dynamics, two-zone charge mixing model shows a significant improvement, and the simulated pressure and temperature responses match with these provided by GT-Power simulations quite well. On the other hand, the in-cylinder pressure of one-zone model has a large error with respect to GT-Power simulation, especially at the beginning of valve opening, but at the end of the intake process it converges to the accurate value due to the effect of the first-order approximation; the in-cylinder temperature of one-zone model has significant error during the entire gas exchange process since it was obtained based upon the in-cylinder pressure, assuming an isentropic process at each time interval. Moreover, at IVC the temperature does not converge to a reasonable value, leading to inaccurate trapped mass calculation and SOC prediction.

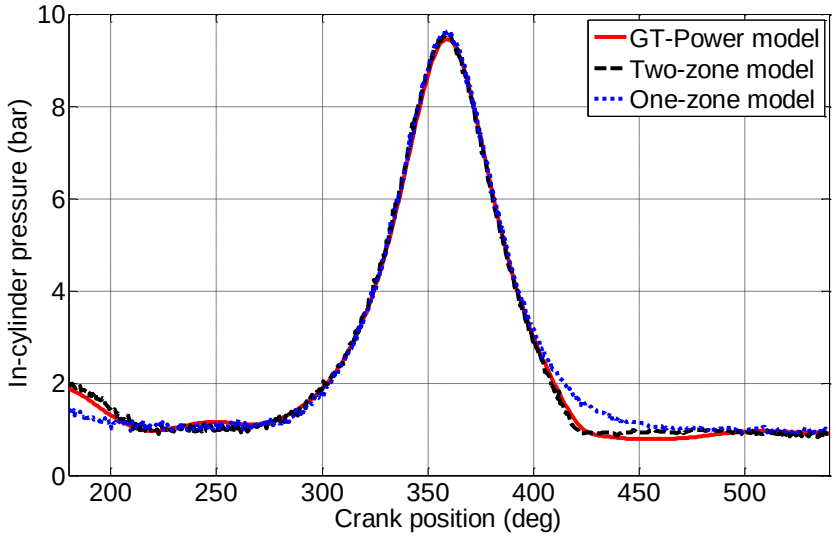

Figure 2. 11: In-cylinder pressure during the gas exchange process.

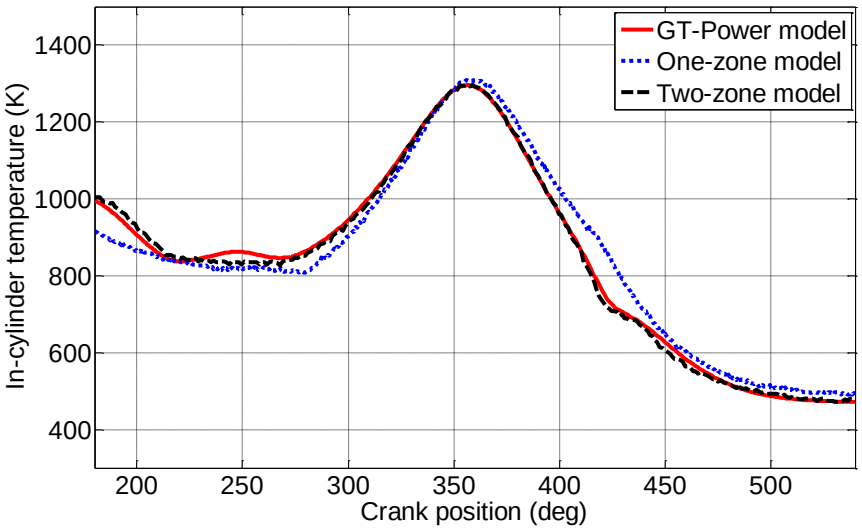

Figure 2. 12: In-cylinder temperature during the gas exchange process.

Table 2.3 compares the simulation results between two-zone and one-zone models under the same engine operation condition, where GT-Power simulation results are used as the baseline. Since the temperature obtained in one-zone model is always higher than the unmixed zone temperature in two-zone model, the SOC prediction is much earlier than that of the two-zone model. The IMEP is also higher due to the error in intake phase and combustion phase.

Table 2. 3: Simulation Results Comparison

Model	Fuel (mg)	SOC	IMEP
GT-Power	13.2	2	4.2
Two-zone model	13.2	2	4.22
One-zone model (w/ flow dynamics)	13.2	4	4.23
One-zone model (w/o flow dynamics)	13.2	8	4.36

In Figure 2.13 both of the simulated exhaust and intake flow rates obtained from the two-zone model were compared with these of GT-Power simulations. Again they matched quite well; on the other hand, the simulation result of one-zone model is not shown here since a first order transfer function was used to approximate the in-cylinder pressure, the flow rate calculation is trivial. This indicates the benefit of the proposed charge mixing model. Note that the error between GT-Power and two-zone model responses are due to the un-modeled pressure wave in both of the intake and exhaust manifolds; and this dynamics is fairly difficult to model using a simplified modeling approach for real-time simulations. However, the proposed charge mixing model does provide good charge flow estimation without pressure wave.

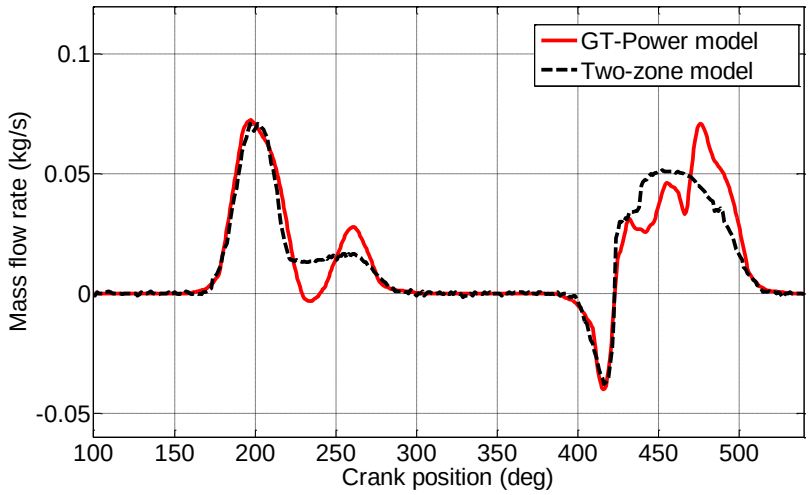

Figure 2. 13: Mass flow rate comparison.

Figure 2.14 shows the charge mixing process during the intake phase. At the beginning of intake valve open, the total in-cylinder trapped mass is reducing due to the backflow in the first stage; afterward, the backflow is sucked back to the cylinder and the trapped mass returns to the level before IVO. Then the third stage begins, fresh charge flows into the cylinder, which causes the mixed zone expanding and unmixed zone shrinking. At first the mass transfer rate is relatively slow since the unmixed zone is not been surrounded by the fresh charge thoroughly; then the transfer rate increases due to the increased intake flow and piston movement; and after IVC, the unmixed zone continues shrinking tardily, which indicates the effect of piston movement on mass diffusion is relatively weaker than that of the intake flow.

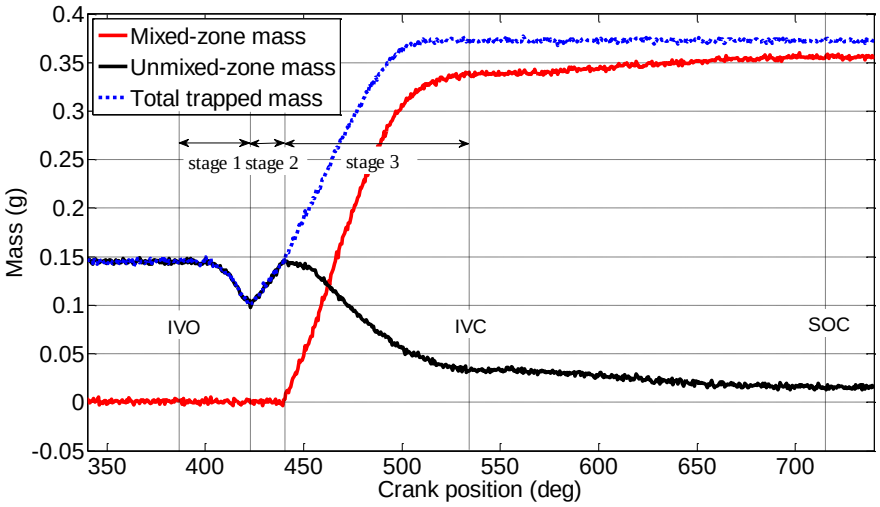

Figure 2. 14: Size change of each zone.

Figure 2.15 shows the in-cylinder average temperature, along with temperature in both of mixed zone and unmixed zone. Obviously, before combustion starts, since the unmixed zone consists of residual gas, its temperature is higher than that of the mixed zone; hence the average in-cylinder temperature is a little higher than that of the mixed zone, since the mixed zone

occupies most portion of the cylinder volume. After combustion, the temperature in the mixed zone rises significantly, but there is no combustion occurs in the unmixed zone, which results in higher temperature in the mixed zone than the average temperature.

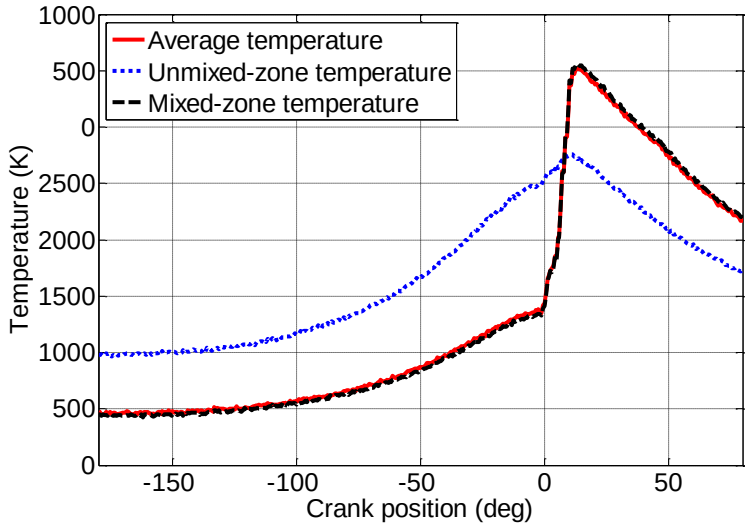

Figure 2. 15: Temperature of each zone.

Figure 2.16 compares in-cylinder pressure of the two-zone model with that of the improved one-zone model during compression and combustion phases. This improved one-zone model contains the flow dynamics during the gas exchange phase. Since the in-cylinder pressure is assumed to be uniformly distributed at any time, the averaged in-cylinder pressure of the two-zone model is much closed to these of the improved one-zone model. It can be seen that in the two-zone model the prediction of the SOC in the two-zone model is later than the one-zone model, and also the peak in-cylinder pressure is lower. This is due to the difference in estimated in-cylinder temperatures since the one-zone model uses the averaged temperature of two zones to estimate the SOC while the two-zone model uses the mixed zone temperature that is lower than the unmixed zone. It can be seen in Figure 2.17 that the Arrhenius integral increases slower for

the two-zone model than that for the one-zone model.

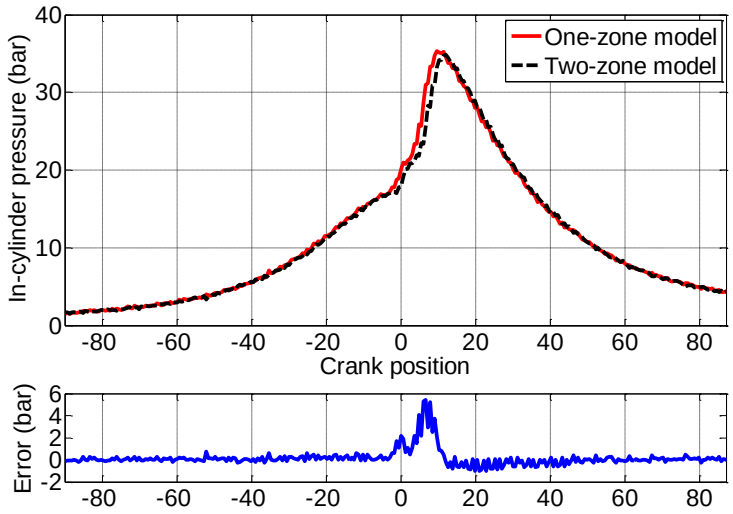

Figure 2. 16: In-cylinder pressure of two-zone and one-zone models.

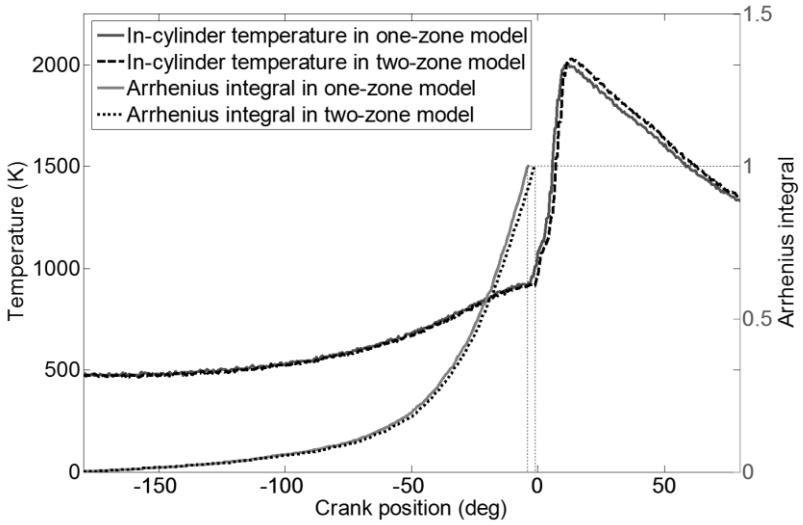

Figure 2. 17: In-cylinder temperature of two-zone and one-zone models.

To validate the charge mixing two-zone model over an operating range, additional simulations were conducted with nine different load conditions at 2000 rpm, where the injected fuel mass varies between 13.2 mg and 10.8 mg; exhaust valve timing EVO and EVC at 156° and 304°, respectively; and intake valve timing IVO and IVC at 382° and 530°, respectively. Figure

18 compares the IMEP and SOC of the two-zone model with those of GT-Power model, and shows that two-zone model has good agreement with GT-Power model.

The two-zone HCCI combustion model was then validated using experimental data. The engine was equipped with intake air heater and without external EGR, and the engine parameters are listed in Table 1. The associated valve timing for EVO, EVC, IVO and IVC are 146°, 294°, 392°, and 540° after TDC, respectively. Intake air temperature is 330K. Figure 2.19 shows the in-cylinder pressure and MFB of the two-zone model and experimental results during combustion phase. Note that the MFB was calibrated based upon the two-piece Wiebe function (a special case of the three-piece one) using experimental data. The parameters in equations (2.20) and (2.21) are: $\alpha = 0.79$, $\beta = 0.21$, $a_1 = a_2 = 0.61$, $\theta_{02} = -6$, $m_1 = 2$, $m_2 = 1.5$, $\Delta\theta_1 = 8$, and $\Delta\theta_2 = 22$. It shows that the two-zone model matches experimental result fairly well during combustion process.

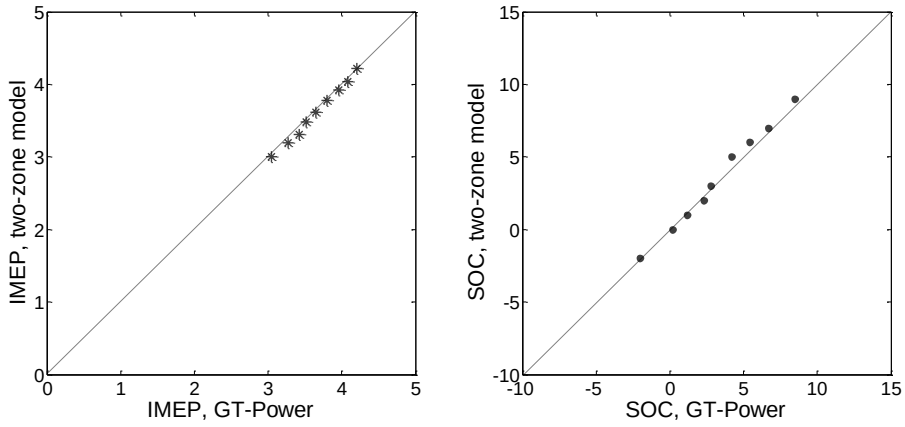

Figure 2. 18: IMEP and SOC of two-zone model and GT-Power model.

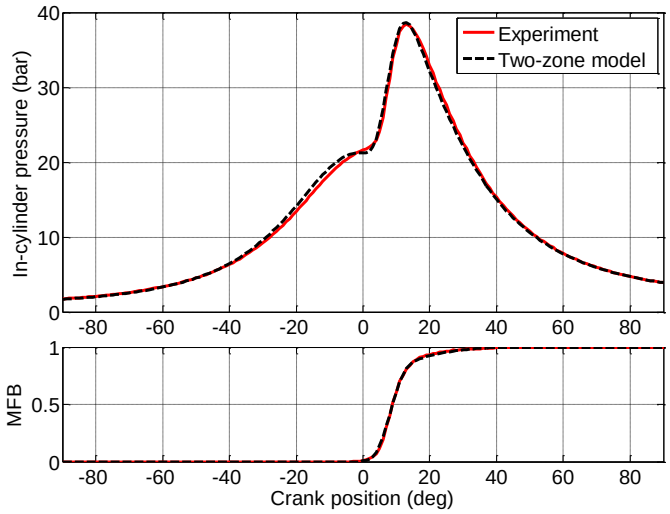

Figure 2. 19: Experimental comparison of In-cylinder pressure and MFB.

In summary, the charge mixing two-zone model is capable of achieving much more accurate simulation results than that of the one-zone model due to utilizing the fluid dynamics analysis. The two-zone charge mixing and combustion model provides the simulation results that are comparable with these of GT-Power model and experimental results.

2.5 Conclusions

A two-zone charge mixing and HCCI (homogeneous charge compression ignition) combustion model is proposed in this chapter based upon the simplified fluid dynamics. The developed model was implemented into the hardware-in-the-loop simulation environment for model validation. The simulation results of the proposed model match with the GT-Power simulation and experimental data well, and it is also demonstrated that the discretized fluid dynamics approach provides a satisfactory simulation results compared with GT-Power model. This indicates that it is feasible to develop a real-time control-oriented engine model that provides comparable simulation results to these provided by high fidelity model such as

GT-Power. The simulation results also show that the unmixed zone plays an important role in predicting the start of combustion, in-cylinder pressure and temperature during the combustion process. It is believed that the two-zone charge mixing and HCCI combustion model provides an improved simulation platform for developing the real-time HCCI control strategy.

CHAPTER 3

LPV MODELING AND MIXED CONSTRAINED H_2/H_∞ CONTROL OF AN ELECTRONIC THROTTLE

3.1 Introduction

Electronic throttle replaces the mechanical link between the vehicle acceleration pedal and engine intake throttle valve plate by accurately regulating the throttle plate position using either a DC motor or step motor [34] for internal combustion (IC) engines. This process is called electronic throttle control (ETC). The traditional engine throttle is mechanically connected to the vehicle acceleration pedal and the engine charge air quantity is controlled by the throttle plate position directly. The engine fuel quantity tracks the charge air to provide the desired air-to-fuel ratio, which is critical for engine emission regulation. The advantage of using the ETC for IC engines is that the engine charge air and fuel can be regulated simultaneously, providing accurate air-fuel-ratio control, especially under the transient engine operations. The ETC is also a key enabler for torque based engine control [35], where the acceleration pedal provides the desired torque and the engine control system determines the desired engine charge air and fuel to meet the torque requirement. The torque based control is especially important for hybrid powertrains ([36] and [37]), where the IC engine, electric machine(s) and generator(s) are managed by their torque outputs or loads. In recent years, as the HCCI (homogeneously charge compression

ignition) combustion is widely studied, the ETC also plays an important role in the mode transition control between SI (spark ignition) and HCCI combustion, where the accurate transient response of the ETC is essential for precise management of cycle-by-cycle charge air, thereby guaranteeing the stable hybrid mode combustion and smooth engine torque output [38].

A conventional electric throttle consists of a DC (or step) motor, a set of speed reduction gears, a throttle plate, and a limp-home (LH) spring set that keeps the valve plate at its default position. The electronic throttle system is highly nonlinear due to the LH spring set, the rotational static and dynamic friction; the vehicle battery voltage fluctuation due to the vehicle electrical load variation introduces another degree of variation; in addition, the torque load introduced by the intake air flow [39] brings additional external disturbance to the electronic throttle system. In this paper, these nonlinearities and variations are modeled as the measurable LPV (linear parameter varying) parameters.

Proportional-integral-derivative (PID) control is widely used in powertrain control systems due to its simplicity ([40] and [41]), and is capable of achieving good performance in large throttle opening case. However, the high nonlinearities of the ETC prevent the PID control from achieving the desired performance under certain operation conditions, especially with small opening near the limp-home position. The other commonly used approach for the electronic throttle control is sliding mode control, where the nonlinearities of friction and spring forces are considered as the parameter uncertainty and bounded external disturbance, respectively ([42]-[44]); however, the robust performance cannot be guaranteed, and sometimes the fast response is achieved with high magnitude of steady state control “chattering”. In [45], a

nonlinear feed-forward and feedback controller based on flatness was designed; however, parameter variations, especially the battery voltage variation, were not considered, leading to a relatively poor performance under these operational conditions. In [46] a linear position regulator was designed based upon the identified linear dynamics part of the system, and adaptive control was applied for the nonlinear time-varying friction and preload torque compensator. To meet the requirement of optimizing the control system performance over a certain operating range, and improve the accuracy of linearization of nonlinear system, LPV method was widely used in control of mechatronic systems [47]-[49] and in ETC system [49][50] in recent years. In [49] a gain-scheduling PID controller was designed to optimize the performance at each fixed operating point; and the stability of the closed-loop system was validated using LPV techniques by transforming the parametric closed-loop system into the LPV form. However, the closed loop performance is not guaranteed under parameter variations. In [50] a physics-based LPV throttle model was established to convert the highly nonlinear system into an LPV system, and an H_2 static output feedback control was designed to guarantee the system performance; however, due to the lack of robustness small modeling error could affect the system stability when a high gain controller was used to improve throttle performance. This motivates the application of the mixed constrained H_2 / H_∞ LPV gain-scheduling control technique to ETC problem in this paper.

The nonlinear electronic throttle system was modeled as an LPV system in this paper, where the friction torque and battery voltage are the varying parameters; and the disturbance torque, induced by the air flow and other sources, was modeled as an exogenous input. A virtual state was introduced to integrate the tracking error for set-point control to achieve zero

steady-state error. A feed-forward control was also used to compensate the preload spring torque designed for the limp-home operation. A mixed constrained H_2 / H_∞ LPV gain-scheduling controller was designed based upon the developed LPV model utilizing the LMI (linear matrix equality) convex optimization scheme, where the H_2 performance was optimized under a loose H_∞ constraint used to guarantee the robust stability of the closed-loop system under modeling uncertainties. A hard constraint, in terms of H_2 bound, is also used to guarantee that the control does not exceed its hardware limit. All weighting matrices were well-tuned during the control design and simulation validation process until the satisfactory performance was achieved. The finalized LPV controller was experimentally validated on a test bench.

This chapter is organized as follows. Section II presents a discrete-time electric throttle model that is linearized into the desired LPV form; and Sections III and IV describe the LMI based convex optimization design for the LPV ETC system and weighting matrices tuning process through simulation, respectively. The associated experimental validation results are shown in Section V. The last section adds some conclusions.

3.2 System Modeling

An electronic throttle system can be described by the schematic diagram shown below in Figure 3.1. A DC motor is driven by a controlled voltage V_a, which is powered by the battery. Note that $V_a = V_b u$ is often regulated by a PWM (pulse width modulated) duty cycle signal u, where the duty cycle is the output of the electronic throttle controller and V_b is the battery voltage. An H-bridge drive module is used to make it possible to apply the voltage in both directions, or equivalently, the duty cycle control signal is between -1 and 1. R and L denote

the resistance and inductance of the DC motor, respectively. The motor is connected to the throttle plate shaft by a set of gears, and a pair of return springs that keeps the throttle plate resting at the default position to enable the limp-home operation when the control input is zero.

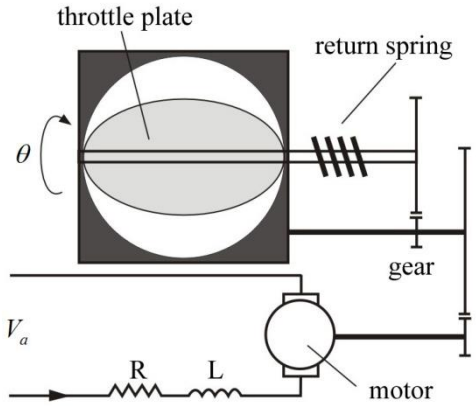

Figure 3. 1: An electronic throttle system

Figure 3.2 shows the nonlinear characteristic of the return spring. The magnitude of spring torque at limp-home position θ_0 is T_s, and the spring torque at θ_0 could take any value between $-T_s$ and T_s. Since the developed model in this paper is linear, the parameter denoting the throttle angle position discussed later is the position relative to θ_0.

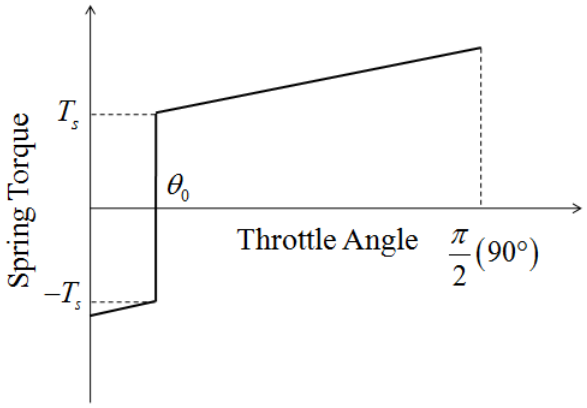

Figure 3. 2: Nonlinear property of return spring

3.2.1 Electronic throttle modeling

The electronic throttle (a mechatronic system) dynamics can be expressed using the following differential equations

$$V_a = iR + L\frac{di}{dt} + E_m, \qquad J\frac{d^2\theta}{dt^2} = T_m - \bar{T}_s - \bar{T}_f - T_d \tag{3.1}$$

where V_a, i, L, and R are the motor voltage, current, inductance and resistance, respectively; $E_m = K_m\dot{\theta}$ is the motor back EMF (electro-magnetic field) voltage, K_m is the back EMF coefficient associated with throttle plate angular velocity; J and θ are motor throttle assembly inertia and throttle angle; and T_m, $\bar{T}_s$, $\bar{T}_f$ and T_d represent the motor output torque, nonlinear spring torque, friction torque and other exogenous input torque such as the disturbance torque due to the unbalanced force, caused by the charge air flow, applied on the throttle plate.

Since the inductance L is relatively small for a DC motor, the inductance dynamics can be ignored and the motor current can be approximated by setting $L = 0$. That is

$$i = \frac{1}{R}\left(V_a - K_m\dot{\theta}\right) \tag{3.1}$$

and the motor output torque satisfies

$$T_m = K_a i = \frac{K_a}{R}\left(V_a - K_m\dot{\theta}\right) \tag{3.2}$$

where K_a is the motor torque coefficient associated with the torque at the throttle plate.

Finally the throttle system dynamics can be described by the following nonlinear differential equation.

$$J\ddot{\theta} = \frac{K_a}{R}\left(V_b u - K_m\dot{\theta}\right) - K_s\theta - T_s\,\mathrm{sgn}\left(\theta\right) - K_B\dot{\theta} - T_f\,\mathrm{sgn}\left(\dot{\theta}\right) - T_d \tag{3.3}$$

where K_B and K_s represent the viscous friction and spring stiffness coefficients; T_s and T_f represent the spring preload torque used to hold the throttle at the limp-home position and Coulomb friction torque, respectively. Note that $\bar{T}_s = K_s\theta + T_s \operatorname{sgn}(\theta)$ and $\bar{T}_f = K_B\dot{\theta} + T_f \operatorname{sgn}(\dot{\theta})$. Differential equation (3.4) can be represented by the following continuous-time state space model

$$\dot{x} = Ax + Bu + \Gamma(\theta, \dot{\theta}), \quad y = Cx \tag{3.4}$$

where

$$A = \begin{bmatrix} 0 & 1 \\ -\frac{K_s}{J} & -\frac{1}{J}\left(\frac{K_a K_m}{R} + K_B\right) \end{bmatrix}, \quad B = \begin{bmatrix} 0 \\ \frac{K_a V_b}{JR} \end{bmatrix}, \quad x = \begin{bmatrix} x_1 \\ x_2 \end{bmatrix} = \begin{bmatrix} \theta \\ \dot{\theta} \end{bmatrix}, \tag{3.5a}$$

$$\Gamma(\theta, \dot{\theta}) = \begin{bmatrix} 0 \\ -\frac{1}{J}\left(T_s \operatorname{sgn}(\theta) + T_f \operatorname{sgn}(\dot{\theta}) + T_d\right) \end{bmatrix}, \quad C = \begin{bmatrix} 1 & 0 \end{bmatrix} \tag{3.6b}$$

Since the system is of high nonlinearity due to term Γ, it has quite different dynamic behaviors (or transfer functions) under different operational conditions. Furthermore, system parameters are coupled in state space matrices; and it is almost impossible to use the experimental throttle step and sinusoid response data to determine all system parameters. Experiments were designed to isolate the throttle system parameters so that the system parameters can be determined by experiments. The spring preload torque and stiffness were obtained by measuring the torque at different stationary points; the Coulomb friction was obtained approximately by moving the throttle plate from the same initial position to opposite directions through electronic control; and the system inertia and viscous friction were obtained together by releasing the throttle plate freely from different holding positions, recording

correspondent responses, and conducting the simulation studies to find the best match for inertia and viscous friction. The obtained system parameters are shown in Table 3.1.

Table 3. 1: Electronic throttle parameters

meter	Value	arameter	alue
R	2.07	J	0035
K_a	0.487	K_m	0.4889
K_B	0.005	K_s	0914
T_f	0.089	T_s	3193

3.2.2 Discrete-time LPV model

To design an LPV gain-scheduling controller, the nonlinear system (3.6) needs to be converted into an LPV one. The entries in matrix Γ were treated in different ways.

Firstly, the spring preload torque $T_s \operatorname{sgn}(\theta)$ can be compensated by a control signal $u_0(\theta)$ as function of θ where

$$u_0 = \frac{RT_s}{K_a V_b} \operatorname{sgn}(\theta) \tag{3.6}$$

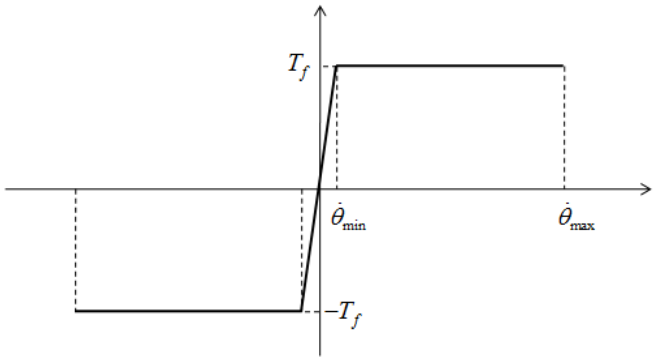

Figure 3. 3: Approximation of sign function

Secondly, as shown in Figure 3.3, $T_f \operatorname{sgn}(\dot{\theta})$ is approximated by

$$T_f \operatorname{sgn}(\dot{\theta}) = \left| T_f \middle/ \dot{\theta} \right| \dot{\theta} = \gamma_1 \dot{\theta} + \Delta T_f, \tag{3.7}$$

where $\left|T_f/\dot{\theta}\right|$ is treated as a term containing varying parameter γ_1 which is defined below

$$\gamma_1 = \begin{cases} T_f / \dot{\theta}, & \left|\dot{\theta}\right| \geq \dot{\theta}_{\min} \\ T_f / \dot{\theta}_{\min}, & else \end{cases}$$

ΔT_f is an uncertain input used to model the error caused by approximation of the sign function. Note that $\dot{\theta}_{\max}$ in Figure 3.3 can be experimentally determined by operating the ETC at the full motor torque and $\dot{\theta}_{\min}$ is chosen to be small enough to reduce approximation error.

Finally, T_d, along with uncertainty ΔT_f, forms the system exogenous input w, where

$$w = \frac{1}{J}\left(\Delta T_f + T_d\right) \tag{3.8}$$

Since the battery voltage varies during operations, V_b can be expressed as

$$V_b = \bar{V}_b\left(1+\gamma_2\right) \tag{3.9}$$

where γ_2 is the second varying parameter that is measurable. The following equation defines the ranges of γ_1 and γ_2.

$$\gamma_1(t) \in [0.0046,\ 32],\ \ \gamma_2(t) \in [-0.417,\ 0.167] \tag{3.10}$$

Then the continuous-time state space model can be converted into the following LPV system

$$\begin{aligned} \dot{x} &= \left(A_c + A_\gamma \gamma_1\right)x + B_{c1}\left(1+\gamma_2\right)u + B_{c2}w \\ y &= C_c x \end{aligned} \tag{3.11}$$

where the system matrices in (3.5) can be expressed as a sum of nominal state space matrices A_c, B_{c1}, B_{c2}, C_c, and varying parameter depended matrices $A_\gamma\gamma_1$ and $B_{c1}\gamma_2$.

There are two approaches to design a discrete-time controller required for microprocessor based control implementation for a continuous-time plant. One is to design a continuous-time

controller and then discretize it and the other is to discretize the plant and design a discrete-time controller directly. Note that both approaches lead to certain errors when the controller is implemented in a microprocessor. For this application, the second approach was selected due to the easy implementation of the designed discrete-time controller and the availability of discrete-time LPV synthesis method. With the selected small sampling period (1ms) it is believed that the required accuracy can be achieved for the discrete-time LPV system. The first order approximation described in [51] was used as follows:

$$\begin{aligned} A_P &= e^{A_c t_s} + e^{A_c t_s} A_\gamma \gamma_1 t_s, \quad C_P = C_c, \\ B_{Pw} &= e^{Act_s} B_{c2} t_s, \qquad\quad B_P = e^{Act_s} B_{c1}\left(1+\gamma_2\right) t_s \end{aligned} \tag{3.12}$$

where t_s, equal to 1ms, is the sampling period of the discrete-time system. For convenience, γ_1 and γ_2 are assumed to lie in the compact structure $\Theta = \mathrm{diag}\{\gamma_1, \gamma_2\}$, and

$$\Theta \in \Omega = \left\{\mathrm{diag}\left(\gamma_1, \gamma_2\right) : 0.000115 \le \gamma_1 \le 0.8, -0.417 \le \gamma_2 \le 0.167\right\} \tag{3.13}$$

The resulting discrete-time state-space LPV system is in the following form of

$$\begin{aligned} x_P\left(k+1\right) &= A_P\left(\Theta\right) x_P\left(k\right) + B_P\left(\Theta\right) u\left(k\right) + B_{Pw} w\left(k\right) \\ y_P\left(k\right) &= C_P x_P\left(k\right) \end{aligned} \tag{3.14}$$

3.2.3 LPV uncertainty model

The existence of modeling errors, due to part-to-part production deviations or circumstance changes (such as temperature and aging), cannot be neglected. For the purpose of enhancing the robustness of the ETC system, modeling uncertainties should be considered. Note that the state matrices in the LPV system (3.12) can be expressed as

$$A_c + A_\gamma \gamma_1 = \begin{bmatrix} 0 & 1 \\ A_{21}\left(\Theta\right) & A_{22}\left(\Theta\right) \end{bmatrix}, \; B_{c1}\left(1+\gamma_2\right) = \begin{bmatrix} 0 \\ B_2\left(\Theta\right) \end{bmatrix} \tag{3.15}$$

and let δ_1 denote the uncertainty on inertia *J* and δ_2 denote the uncertainty corresponding to the friction (including Coulomb and viscous friction), then the continuous-time state matrices of the LPV system with uncertainties are in the form of

$$\begin{aligned} A_\delta(\Theta) &= \begin{bmatrix} 0 & 1 \\ A_{21}(\Theta)(1+\delta_1) & A_{22}(\Theta)(1+\delta_1)(1+\delta_2) \end{bmatrix}, \\ B_\delta(\Theta) &= \begin{bmatrix} 0 \\ B_2(\Theta)(1+\delta_1) \end{bmatrix} \end{aligned} \tag{3.16}$$

Based on the LFT (linear fractional transformation) technique [54] with the first-order approximation, extra inputs and outputs can be appropriately defined to "pull out" the uncertainty parameters. Choosing $z_{\infty 1} = x_1$, $z_{\infty 2} = z_{\infty 4} = x_2$, $z_{\infty 3} = u$ and w_∞, respectively, and discretizing the system using the same first order approximation method as in (3.13) results in a discrete-time system in the LFT form:

$$\begin{cases} x_P(k+1) &= A_P(\Theta)x_P(k) + B_P(\Theta)u(k) + B_{P\infty}(\Theta)w_\infty(k) \\ w_\infty(k) &= \Delta z_\infty(k) \end{cases} \tag{3.17}$$

where $w_\infty = [w_{\infty 1}, w_{\infty 2}, w_{\infty 3}, w_{\infty 4}]^{\mathrm{T}}$, $z_\infty = [z_{\infty 1}, z_{\infty 2}, z_{\infty 3}, z_{\infty 4}]^{\mathrm{T}}$ and $\Delta = \mathrm{diag}[\delta_1, \delta_1, \delta_1, \delta_2]^{\mathrm{T}}$. The detailed procedure of LFT is omitted here.

3.2.4 Set-point control

In order to achieve zero steady-state regulation error, a third state was added to the electric throttle model in the discrete-time form：

$$x_I(k+1) = x_I(k) + t_s r(k) - t_s x_1(k) \tag{3.18}$$

where *r* denotes the reference signal. Since the throttle position can be measured directly, x_I can be obtained by integrating the tracking error online, and it is available for the state feedback.

3.2.5 Reduced order observer

Since the angular velocity, the second state (x_2), cannot be measured directly, an observer is required for output feedback control. A reduced order observer below was designed based upon the method described in [55] to estimate x_2:

$$\begin{aligned} x_O(k+1) &= \left(A_{P22}(k) - LA_{P12}(k)\right)x_O(k) + B_{P2}(k)u(k) \\ &\quad + \left(A_{P21}(k) - LA_{P11}(k) + LA_{P22}(k) - L^2A_{P12}(k)\right)x_1(k) \\ \hat{x}_2(k) &= x_O(k) + Lx_1(k) \end{aligned} \tag{3.19}$$

where A_{Pij} is the $(i,j)^{\text{th}}$ element of system matrix A_p in (3.13). Let

$$A_{O1}(k) =: \left(A_{P22}(k) - LA_{P12}(k)\right)$$

$$A_{O2}(k) =: \left(A_{P21}(k) - LA_{P11}(k) + LA_{P22}(k) - L^2A_{P12}(k)\right)$$

and the reduced observer can be rewritten as

$$x_O(k+1) = A_{O1}(k)x_O(k) + A_{O2}(k)x_1(k) + B_{P2}(k)u(k) \tag{3.20}$$

The observer gain was chosen by pole placement to guarantee that the estimation converges faster than the system response.

3.3 LPV Control Design

3.3.1 Augmented LPV system

0 shows the closed-loop discrete-time system architecture, where plant P is the resulting discrete-time state space model described in (15) and (18) with the third state $x_3 = x_I$ added for the set-point control; K is the closed-loop LPV controller to be designed. The control input of the system is a summation of feedback control u (from LPV controller K) and the feed-forward control u_0 (used to compensate the spring preload torque). Since u_0 can be obtained directly by

(3.7) with known (measured) battery voltage, and will only change sign when crossing the limp-home position, it will be ignored during the closed-loop control design process and compensated with a feed-forward control. For the LPV control design, since the system is linear, the reference signal can be set to zero for control design. System nominal performance is addressed by minimizing the weighted H_2 norm of outputs (tracking error z_1 and integral of tracking error z_2), subject to control input H_2 constraint, to have the balanced performance between small tracking error and fast response. This problem is a deterministic ICC (input covariance constraint) problem defined in [53], where LMI convex optimization approach can be used. Weighting functions W_e and W_I are selected as design constants and were tuned during the control design and experimental validation process for the best performance possible.

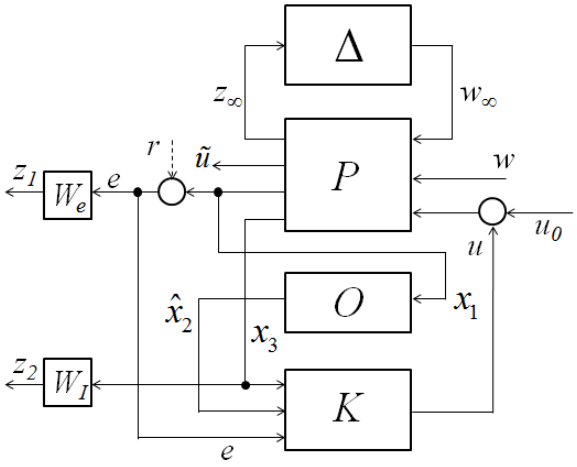

Figure 3. 4: Closed loop system block diagram

Robust stability is considered by investigating the LFT structure with extra inputs and outputs shown in the upper part of Figure 3.4. Since H_∞ controllers is capable of providing robust stability margins that H_2 controllers cannot [54], a predetermined bound on the H_∞

norm of the closed-loop transfer function from input w_∞ to output z_∞ was imposed.

Finally, the augmented discrete-time LPV systems $\Pi_2(\theta)$ and $\Pi_\infty(\theta)$ can be constructed:

$$\Pi_2(\theta):\quad \begin{bmatrix} x(k+1) \\ \tilde{u}(k) \\ z(k) \\ y(k) \end{bmatrix} = \begin{bmatrix} A(\Theta) & B_w(\Theta) & B_u(\Theta) \\ 0 & 0 & D_2 \\ C_1 & 0 & 0 \\ C_2 & 0 & 0 \end{bmatrix} \begin{bmatrix} x(k) \\ w(k) \\ u(k) \end{bmatrix} \tag{3.21a}$$

$$\Pi_\infty(\theta):\quad \begin{bmatrix} x(k+1) \\ z_\infty(k) \\ y(k) \end{bmatrix} = \begin{bmatrix} A(\Theta) & B_\infty(\Theta) & B_u(\Theta) \\ C_\infty & D_w & D_u \\ C_2 & 0 & 0 \end{bmatrix} \begin{bmatrix} x(k) \\ w_\infty(k) \\ u(k) \end{bmatrix} \tag{3.22b}$$

where $x(k) = \left[x_p^T(k)\ x_I^T(k)\ x_O^T(k)\right]^T \in \mathbb{R}^4$, the performance output $z(k) = \left[z_1(k)\ z_2(k)\right]^T \in \mathbb{R}^2$ and the measurement for control $y(k) = \left[y_P(k),\ y_I(k),\ y_D(k)\right]^T \in \mathbb{R}^3$. Note that $\tilde{u}$ denotes control inputs subject to certain constraints. For this application with single input, D_2 is a scalar that was set to one and $\tilde{u} = u$. w_∞ and output z_∞ are defined in (18). The state space matrices are

$$A(\Theta) = \begin{bmatrix} A_P(\Theta) & \begin{matrix} 0 & 0 \\ 0 & 0 \end{matrix} \\ \begin{matrix} -t_s & 0 \\ A_{O2}(\Theta) & 0 \end{matrix} & \begin{matrix} 1 & 0 \\ 0 & A_{O1}(\Theta) \end{matrix} \end{bmatrix},\ B_w(\Theta) = \begin{bmatrix} B_{Pw}(\Theta) \\ 0 \\ 0 \end{bmatrix},\ B_u(\Theta) = \begin{bmatrix} B_P(\Theta) \\ 0 \\ B_{P2}(\Theta) \end{bmatrix},$$

$$C_1 = \begin{bmatrix} -W_e & 0 & 0 & 0 \\ 0 & 0 & W_I & 0 \end{bmatrix},\ C_2 = \begin{bmatrix} -1 & 0 & 0 & 0 \\ L & 0 & 0 & 1 \\ 0 & 0 & 1 & 0 \end{bmatrix},\ D_2 = 1, \tag{3.22}$$

$$B_\infty(\Theta) = \begin{bmatrix} B_{P\infty}(\Theta) \\ 0 \end{bmatrix},\ C_\infty = \begin{bmatrix} 1 & 0 & 0 \\ 0 & 1 & 0 \\ 0 & 0 & 0 \\ 0 & 1 & 0 \end{bmatrix},\ D_w = 0,\ D_u = \begin{bmatrix} 0 \\ 0 \\ 1 \\ 0 \end{bmatrix}.$$

In the next subsection, the varying parameter compact set Θ will be expressed in a polytope structure, where the vertices of the polytope and the time-varying parameter rate of change will be defined. The system model will be put into a form applicable for the LMI convex

optimization.

3.3.2 Mixed constrained H_2/H_∞ control synthesis

For the augmented system (3.22), the goal is to design a static output feedback LPV gain-scheduling controller, $u(k)=K(\Theta)y(k)$, that minimizes the upper bound of the H_2 norm from $w(k)$ to $z(k)$ over any trajectories of $\Theta(k)\in\Theta$ for closed-loop LPV system Π_2 subject to the constraint on the H_2 norm from $w(k)$ to $u(k)$, and at the same time, H_∞ norm constraint η from w_∞ to z_∞ for closed-loop LPV system Π_∞ to guarantee the robust stability against the uncertain constraint $\|\Delta\|_\infty<\eta^{-1}$.

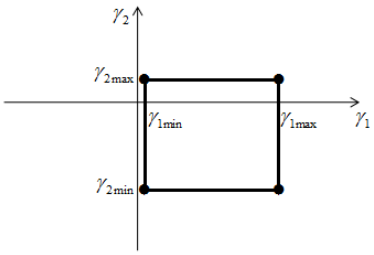

Figure 3. 5: Parameter space polytope

The state space model (22) was converted into a discrete-time polytopic time-varying system by expressing state space matrices containing varying parameters ($A(\Theta)$ and $B(\Theta)$) at the vertices of the parameter space polytope, as shown in Figure 3.5. Any system inside the polytope is represented by a convex combination of the vertex systems as weighted by the vector $\lambda(k)$ of the barycentric coordinates, and formula for computing the barycentric coordinates is available in [56]. The discrete-time polytopic time-varying system is given by

$$\Pi_2 : \begin{bmatrix} x(k+1) \\ \tilde{u}(k) \\ z(k) \\ y(k) \end{bmatrix} = \begin{bmatrix} \tilde{A}(\lambda(k)) & \tilde{B}_w(\lambda(k)) & \tilde{B}_u(\lambda(k)) \\ 0 & 0 & \tilde{D}_2 \\ \tilde{C}_1 & 0 & 0 \\ \tilde{C}_2 & 0 & 0 \end{bmatrix} \begin{bmatrix} x(k) \\ w(k) \\ u(k) \end{bmatrix} \tag{3.23a}$$

$$\Pi_\infty : \begin{bmatrix} x(k+1) \\ z_\infty(k) \end{bmatrix} = \begin{bmatrix} \tilde{A}(\lambda(k)) & \tilde{B}_\infty(\lambda(k)) & \tilde{B}_u(\lambda(k)) \\ \tilde{C}_\infty & \tilde{D}_w & \tilde{D}_u \end{bmatrix} \begin{bmatrix} x(k) \\ w_\infty(k) \\ u(k) \end{bmatrix} \tag{3.24b}$$

where the system matrices $\tilde{A}(\lambda(k)) \in \mathbb{R}^{4\times4}$, $\tilde{B}_w(\lambda(k)) \in \mathbb{R}^{4\times1}$, $\tilde{B}_u(\lambda(k)) \in \mathbb{R}^{4\times1}$ and $\tilde{B}_\infty(\lambda(k)) \in \mathbb{R}^{4\times4}$ belong to the following polytope

$$\begin{aligned} \mathcal{D} = \Big\{ & \left(\tilde{A}, \tilde{B}_w, \tilde{B}_u, \tilde{B}_\infty\right)(\lambda(k)) : \\ & \left(\tilde{A}, \tilde{B}_w, \tilde{B}_u, \tilde{B}_\infty\right)(\lambda(k)) = \sum_{i=1}^{N} \lambda_i(k) \left(A_i, B_{w,i}, B_{u,i}, B_{\infty,i}\right)_i, \lambda(k) \in \Lambda \Big\} \end{aligned} \tag{3.24}$$

where A_i, $B_{w,i}$, $B_{u,i}$ and $B_{\infty,i}$ are vertices of the polytope with $N = 4$ in this case, and $\lambda(k)$ is a vector in the barycentric coordinates which belongs to the unit simplex

$$\Lambda = \left\{ \zeta \in \mathbb{R}^N : \sum_{i=1}^{N} \zeta_i = 1, \zeta_i \geq 0, i = 1, \cdots, N \right\} \tag{3.25}$$

The rate of variation of $\lambda(k)$ can be defined as

$$\Delta\lambda_i(k) = \lambda_{i+1}(k) - \lambda_i(k), i = 1, \cdots, N \tag{3.26a}$$

which is bounded by

$$-b \leq \Delta\lambda_i(k) \leq b, i = 1, \cdots, N \tag{3.27b}$$

where $b \in [0,1]$. In this paper, *b* was selected to be 0.1 to cover the worst operational condition. Note that the uncertainty domain, where the vector $\left(\lambda(k), \Delta\lambda_i(k)\right)^{\mathrm{T}} \in \mathbb{R}^{2N}$ assumes values, can be modeled by the compact set

$$\Gamma_b = \left\{ \delta \in \mathbb{R}^{2N} : \delta \in co\left\{ g^1, ..., g^M \right\},\ \ g^j = \begin{pmatrix} f^j \\ h^j \end{pmatrix},\ f^j \in \mathbb{R}^N,\ h^j \in \mathbb{R}^N, \right.$$
$$\left. \sum_{i=1}^{N} f_i^{\,j} = 1 \text{ with } f_i^{\,j} \geq 0,\ i = 1, ..., N,\ \sum_{i=1}^{N} h_i^j = 0,\ j = 1, ..., M \right\} \tag{3.27}$$

Then using $\gamma(k) \in \Lambda_M$,

$$\left(\lambda(k), \Delta\lambda_i(k)\right)^{\mathrm{T}} = \sum_{j=1}^{M} \begin{pmatrix} f^j \\ h^j \end{pmatrix} \gamma_j(k) \tag{3.28}$$

Before introducing the mixed H_2/H_∞ LPV control problem, the constrained H_2 and H_∞ LPV control problems are to be discussed, respectively. Note that the LMIs of the standard H_2 LPV for discrete-time systems was introduced in Theorem 9 of [57]; and the LMI conditions for the constrained H_2 problem (also called the input covariance constraint problem) were given for discrete-time LTI systems in [53]. Theorem 1 below provides the LMIs for the constrained H_2 LPV systems. Note that the input covariance constraint matrix $\bar{U}$ is now part of the LMIs stated in equations (3.32) and (3.33). The proof of Theorem 1 is provided in Appendix.

Theorem 1. Consider system Π_2, given $\bar{U}$, if there exists, for i = 1, ... , N, matrices $G_i \in \mathbb{R}^{4\times4}$ and $Z_i \in \mathbb{R}^{1\times4}$, and symmetric positive-definite matrices $P_{2,i} \in \mathbb{R}^{4\times4}$ and $W_i \in \mathbb{R}^{4\times4}$ such that the following LMIs hold

$$\begin{bmatrix} \sum_{i=1}^{N} \left(f_i^{\,j} + h_i^j \right) P_{2,i} & * & * \\ \tilde{G}_j^{\mathrm{T}} \tilde{A}_j^{\mathrm{T}} + \tilde{Z}_j^{\mathrm{T}} \tilde{B}_{u,j}^{\mathrm{T}} & \tilde{G}_j + \tilde{G}_j^{\mathrm{T}} - \sum_{i=1}^{N} f_i^{\,j} P_{2,i} & * \\ \tilde{B}_{w,j}^{T} & 0 & I \end{bmatrix} = \Phi_j > 0 \tag{3.29}$$

for j = 1, ... , M;

$$\begin{bmatrix} \sum_{i=1}^{N}\left(f_i^{\,j}+f_i^{\,l}+h_i^{j}+h_i^{l}\right)P_{2,i} & * & * \\ \tilde{G}_j^{\mathrm{T}}\tilde{A}_l^{\mathrm{T}}+\tilde{G}_l^{\mathrm{T}}\tilde{A}_j^{\mathrm{T}}+\tilde{Z}_j^{\mathrm{T}}\tilde{B}_{u,l}^{\mathrm{T}}+\tilde{Z}_l^{\mathrm{T}}\tilde{B}_{u,j}^{\mathrm{T}} & \Phi_{22,jl} & * \\ \tilde{B}_{w,j}^{T}+\tilde{B}_{w,l}^{T} & 0 & 2I \end{bmatrix}=\Phi_{jl}>0 \tag{3.30}$$

where

$$\Phi_{22,jl}=\tilde{G}_j+\tilde{G}_j^{\mathrm{T}}+\tilde{G}_l+\tilde{G}_l^{\mathrm{T}}-\sum_{i=1}^{N}\left(f_i^{\,j}+f_i^{\,l}\right)P_{2,i}$$

for j = 1, ... , *M-1*, and $l = j$+1, ... , M;

$$\begin{bmatrix} \sum_{i=1}^{N} f_i^{\,j}\bar{U} & * \\ \tilde{Z}_i^{\mathrm{T}}\tilde{D}_{2,i}^{\mathrm{T}} & \tilde{G}_i+\tilde{G}_i^{\mathrm{T}}-\sum_{i=1}^{N} f_i^{\,j}P_{2,i} \end{bmatrix}=\Psi_j>0 \tag{3.31}$$

for j= 1, ... , M;

$$\begin{bmatrix} \sum_{i=1}^{N}\left(f_i^{\,j}+f_i^{\,l}\right)\bar{U} & * \\ \tilde{Z}_i^{\mathrm{T}}\tilde{D}_{2,j}^{\mathrm{T}}+\tilde{Z}_j^{\mathrm{T}}\tilde{D}_{2,i}^{\mathrm{T}} & \Psi_{22,jl} \end{bmatrix}=\Psi_{jl}>0 \tag{3.32}$$

where

$$\Psi_{22,jl}=\tilde{G}_j+\tilde{G}_j^{\mathrm{T}}+\tilde{G}_l+\tilde{G}_l^{\mathrm{T}}-\sum_{i=1}^{N}\left(f_i^{\,j}+f_i^{\,l}\right)P_{2,i}$$

for j = 1, ... , *M-1*, and $l = j$+1, ... , M;

$$W_i-\tilde{C}_1P_{2,i}\tilde{C}_1^{\mathrm{T}}\geq 0,\ i=1,\cdots,N, \tag{3.33}$$

with

$$\tilde{G}_j=\sum_{i=1}^{N} f_i^{\,j}G_i,\ \ \tilde{Z}_j=\sum_{i=1}^{N} f_i^{\,j}Z_i$$

then the state feedback controller

$$K\left(\lambda(k)\right)=\hat{Z}\left(\lambda(k)\right)\hat{G}\left(\lambda(k)\right)^{-1} \tag{3.34}$$

where

$$\hat{G}\left(\lambda(k)\right)=\sum_{i=1}^{N}\lambda_i(k)G_i,\ \ \hat{Z}\left(\lambda(k)\right)=\sum_{i=1}^{N}\lambda_i(k)Z_i \tag{3.35}$$

stabilizes system Π_2 with a guaranteed H_2 performance ν given by

$$\nu^2=\min_{P_{\infty,i},P_{2,i}G_i,Z_i,W_i}\max_i trace(W_i)\geq trace\left(C_1\bar{P}_2C_1^{\mathrm{T}}\right) \tag{3.36}$$

and also satisfies the input constraint

$$U=\tilde{D}_2K\bar{P}_2K^{\mathrm{T}}\tilde{D}_2^{\mathrm{T}}<\tilde{D}_2KP_2K^{\mathrm{T}}\tilde{D}_2^{\mathrm{T}}<\bar{U} \tag{3.37}$$

□

Proof of Theorem 1: LMIs (3.30) and (3.31) follow Theorem 9 of [57]. Define $A_{cl}(k)=\tilde{A}(k)+\tilde{B}_u(k)K(k)$, and let $\bar{P}_2(k)$ denote the closed-loop controllability Gramian, then $\bar{P}(k)$satisfies

$$\bar{P}_2(k+1)=A_{cl}(k)\bar{P}_2(k)A_{cl}(k)^{\mathrm{T}}+\tilde{B}_w(k)\tilde{B}_w(k)^{\mathrm{T}},\ \bar{P}_2(0)=0$$

Since equations (3.30) and (3.31) imply that

$$P_2(k+1)>A_{cl}(k)P_2(k)A_{cl}(k)^{\mathrm{T}}+\tilde{B}_w(k)\tilde{B}_w(k)^{\mathrm{T}}$$

there exists a matrice $M(k)=M(k)^{\mathrm{T}}>0$ such that

$$P_2(k+1)=A_{cl}(k)P_2(k)A_{cl}(k)^{\mathrm{T}}+\tilde{B}_w(k)\tilde{B}_w(k)^{\mathrm{T}}+M(k)$$

Consequently, $P_2(k)>\bar{P}_2(k)$ for all $k\geq 0$. Then for any $\gamma(k)\in\Lambda_M$, multiply (3.32) by γ_j^2 and sum for $j=1,...,M$ and multiply (3.33) by $\gamma_j\gamma_l$ and sum for $j=1,...,M-1$ and $l=j+1,...,M$. Adding the two resulting expressions to obtain

$$\Psi = \sum_{j=1}^{M} \gamma_j^2 \Psi_j + \sum_{j=1}^{M-1} \sum_{l=j+1}^{M} \gamma_j \gamma_l \Psi_{jl}$$
$$= \begin{bmatrix} \bar{U} & * \\ \tilde{Z}(\gamma)^{\mathrm{T}} \tilde{D}_2^{\mathrm{T}} & \tilde{G}(\gamma) + \tilde{G}(\gamma)^{\mathrm{T}} - \sum_{j=1}^{M} \gamma_j \left(\sum_{i=1}^{N} f_i^{\,j} P_{2,i} \right) \end{bmatrix}$$
$$= \begin{bmatrix} \bar{U} & * \\ \tilde{Z}(\lambda(k))^{\mathrm{T}} \tilde{D}_2^{\mathrm{T}} & \tilde{G}(\lambda(k)) + \tilde{G}(\lambda(k))^{\mathrm{T}} - P_2(\lambda(k)) \end{bmatrix} > 0$$

Multiply Ψ by $\begin{bmatrix} \mathrm{I} & -\tilde{D}_2 K(\lambda(k)) \end{bmatrix}$ on the left and by its transpose on the right yielding

$$\bar{U} - \tilde{D}_2 K(\lambda(k)) P_2(\lambda(k)) K(\lambda(k))^{\mathrm{T}} \tilde{D}_2{}^{\mathrm{T}} > 0 \Rightarrow \bar{U} > \tilde{D}_2 K P_2 K^{\mathrm{T}} \tilde{D}_2^{\mathrm{T}} > \tilde{D}_2 K \bar{P}_2 K^{\mathrm{T}} \tilde{D}_2^{\mathrm{T}} = U$$

Similarly, from (3.34) it can be shown that

$$W_i \geq \tilde{C}_1 P_{2,i} \tilde{C}_1^{\mathrm{T}} > \tilde{C}_1 \bar{P}_2 \tilde{C}_1^{\mathrm{T}}, \text{ for all } i = 1, \cdots, N$$

Therefore,

$$\nu^2 = \min_{P_{\infty,i}, P_{2,i} G_i, Z_i, W_i} \max_i trace(W_i) \geq trace\left(C_1 \bar{P}_2 C_1^{\mathrm{T}} \right).$$

□

Note that equations (3.30) and (3.31) address the stability issue; equations (3.32) and (3.33) apply the input constraint to the system; and equation (3.34) gives the condition corresponding to H_2 performance.

For the H_∞ LPV control problem, consider system Π_∞. Based on Theorem 8 of [57], if there exists, for i = 1, ... , N, symmetric positive-definite matrices $P_{\infty,i} \in \mathbb{R}^{3\times 3}$ such that the following LMIs hold

$$\begin{bmatrix} \sum_{i=1}^{N} \left(f_i^{\,j} + h_i^{\,j} \right) P_{\infty,i} & * & * & * \\ \tilde{G}_j^{\mathrm{T}} \tilde{A}_j^{\mathrm{T}} + \tilde{Z}_j^{\mathrm{T}} \tilde{B}_{u,j}^{\mathrm{T}} & \tilde{G}_j + \tilde{G}_j^{\mathrm{T}} - \sum_{i=1}^{N} f_i^{\,j} P_{\infty,i} & * & * \\ \tilde{B}_{\infty,j}^{T} & 0 & \eta I & * \\ 0 & \tilde{C}_{\infty,j} \tilde{G}_j + \tilde{D}_{u,j} \tilde{Z}_j & \tilde{D}_{w,j} & \eta I \end{bmatrix} = \Theta_j > 0 \qquad (3.38)$$

for $j = 1, \ldots, M$, and

$$\begin{bmatrix} \sum_{i=1}^{N}\left(f_i^{\,j} + f_i^{\,l} + h_i^{\,j} + h_i^{\,l}\right) P_{\infty,i} & * & * & * \\ \Theta_{21,jl} & \Theta_{22,jl} & * & * \\ \tilde{B}_{\infty,j}^{T} + \tilde{B}_{\infty,l}^{T} & 0 & 2\eta I & * \\ 0 & \Theta_{42,jl} & \tilde{D}_{w,j} + \tilde{D}_{w,l} & 2\eta I \end{bmatrix} = \Theta_{jl} > 0 \qquad (3.39)$$

for $j = 1, \ldots, M\text{-}1$, and $l = j+1, \ldots, M$, where

$$\Theta_{21,jl} = \tilde{G}_j^{\mathrm{T}} \tilde{A}_l^{\mathrm{T}} + \tilde{G}_l^{\mathrm{T}} \tilde{A}_j^{\mathrm{T}} + \tilde{Z}_j^{\mathrm{T}} \tilde{B}_{u,l}^{\mathrm{T}} + \tilde{Z}_l^{\mathrm{T}} \tilde{B}_{u,j}^{\mathrm{T}}$$
$$\Theta_{22,jl} = \tilde{G}_j + \tilde{G}_j^{\mathrm{T}} + \tilde{G}_l + \tilde{G}_l^{\mathrm{T}} - \sum_{i=1}^{N}\left(f_i^{\,j} + f_i^{\,l}\right) P_{\infty,i}$$
$$\Theta_{42,jl} = \tilde{C}_{\infty,j} \tilde{G}_l + \tilde{C}_{\infty,l} \tilde{G}_j + \tilde{D}_{u,j} \tilde{Z}_l + \tilde{D}_{u,l} \tilde{Z}_j$$

then the static output feedback controller $K\left(\lambda(k)\right)$ given by (35) also stabilizes the system Γ Π_∞ with a guaranteed H_∞ performance from w_∞ to z_∞ bounded by η.

Mixed constrained H_2/H_∞ LPV control design problem:

For both systems Π_2 and Π_∞ find an optimal LPV (gain-scheduling) controller, defined in (3.36), that minimizes the H_2 performance ν, defined in (3.37), with the given input (control) covariance bound $\bar{U}$ for system Π_2 and H_∞ norm bound η for system Π_∞ subject to the LMI conditions (3.30)-(3.34) and (3.38)-(3.39).

□

The LMI convex optimization approach can be used to solve the above LPV gain-scheduling control problem. That is also reported in [58]-[60].

The resulting closed-loop system with the LPV optimal control is robustly stable for $\|\Delta\|_\infty \le \eta^{-1}$, where Δ is the system modeling uncertainty defined in (3.18); and assuming $\Delta = 0$ the system H_2 performance defined in (3.37) is minimized with satisfactory constraint on the

control covariance defined in (3.38).

Note that the maximum singular value of $\bar{U}$ in (3.36) provides an upper bound for the control covariance matrix of the closed-loop system, which can be interpreted as an upper bound of the system l_2 to l_∞ gain from *w* to control input *u*, that is,

$$\|u\|_\infty^2 \le \sup_{t\ge 0} u^T(t)u(t) \le \bar{\sigma}(\bar{U}) \cdot \|w\|_2^2$$

due to the system l_2 to l_∞ gain; see [52], where $\bar{\sigma}(\cdot)$ denotes the maximum singular valve. Therefore, the l_∞ norm of control signal *u*(*t*) is bounded by $\bar{\sigma}(\bar{U})^{1/2}$ for any l_2 disturbance input *w* with its norm less than or equal to 1, which provides a method of designing LPV controllers with hard constraints on control inputs by selecting a proper $\bar{U}$.

3.4 Weighting Matrices Tuning

All weighting matrices were tuned during the control design and simulation validation phase. W_e and W_I, defined in Figure 3.4, are weighting matrices corresponding to performance outputs z_1 and z_2, which are tracking error and integral of tracking error, respectively. Under an l_2 bounded exogenous input w assumption with its l_2 norm bounded by 1, the l_∞ norm of outputs z_1 and z_2 are bounded by the diagonal elements of W_i defined in (3.37) due to the system l_2 to l_∞ gain. Tuning W_e and W_I leads to changing the penalty levels of the peak values of tracking error and error integral (their l_∞ gains), which could result in different tracking performance, such as overshoot, rise time and settling time, etc. Table II shows a sequence of controllers with different weighting matrices. Controllers 1 to 3 were designed to find a balance between W_e and W_I for achieving fast response without overshoot; controllers 4 to 6 were the results of relaxing the control constraint to obtain high control gain, leading to fast response. The

constraint η on the system H_∞ norm, defined in (3.39) and (3.40) is 250. Note that controllers were also designed with the same weighting matrices and the H_∞ norm bound as these used for controller 6 but with more relaxed control constraint $\bar{U}$, however the closed-loop system response was similar to that of controller 6. This is mainly due to the fact that as the control gain reaches certain point, the H_∞ norm constraint becomes active, which prevents the control gain from increasing, and the result is illustrated at the end of this section. As a result, controller 6 shows the most satisfactory performance and was experimentally validated later on.

Table 3. 2: Weighting matrices tuning

ontroller	W_e	W_I	$\bar{U}$
1	2.5	2.0	2
2	2.5	1.0	2
3	2.5	0.6	2
4	2.5	0.7	5
5	2.5	0.8	10
6	2.5	0.8	25

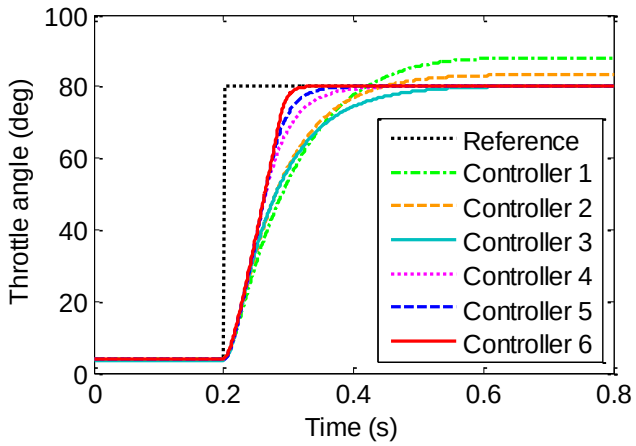

Figure 3. 6: Simulation results

Figure 3.7 shows the relationship between the input constraint $\bar{U}$ and the achieved H_2 performance ν, where ν is the minimum value given by (3.35) corresponding to the maximum

achievable performance under each given input constraint $\bar{U}$. An H_2 control without considering H_∞ performance bound η ($\eta = \infty$) is also plotted for comparison. As the input constraint increases (physically larger control effort), improved H_2 performance can be achieved. Note that when the input constraint is small, the performance curve of H_2 control and mixed control overlaps each other; this is because within this range, the H_∞ norm constraint is not active. On the other hand, when input constraint is large, the resulting controller have relatively high control gain, which makes the system robust stability sensitive to the uncertainties. Therefore, the H_∞ bound η becomes active which prevents the LPV control from improving its H_2 performance. In fact, the performance could become worse in practice due to unmodeled uncertainty. This demonstrates that the mixed constrained H_2/H_∞ is able to provide a good balance between the robust stability and performance.

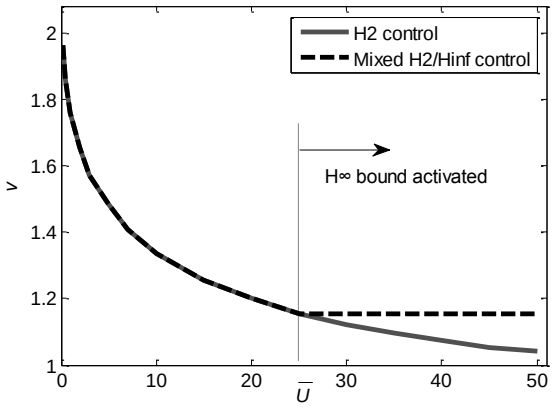

Figure 3. 7: Relationship between input constraint and performance

3.5 Experimental Validation

The finalized controller was then implemented into the MSU Opal-RT based prototype controller with a sampling time t_s = 1ms. The controller provides both PWM signal reference and

sign control signals to an H-bridge driver used to control the electronic throttle DC motor, see Figure 3.8 for the test bench setup.

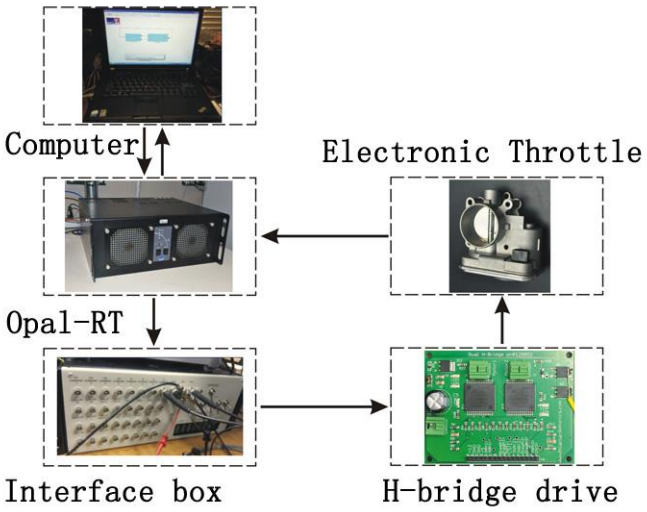

Figure 3. 8: Test bench setup

Firstly, three typical cases were investigated: large opening, crossing limp-home, and small opening operations, and the corresponding responses are shown in Figure 3.9 to 3.12. In general, to guarantee the vehicle's acceleration performance with reduced time delay between acceleration pedal position and throttle position, the settling time of the ETC system should be as short as possible. For example, during the SI and HCCI mode transition, it requires that the throttle plate opens from a small angle to widely-open within a few engine cycles, which is less than 0.2 second; furthermore, in order to control the charge air precisely, the throttle displacement needs to track a desired trajectory. Figure 3.9 and 10 show that for both opening and closing against a small angle and a large angle, the settling timing of the ETC system is within 0.1 second, which shows satisfactory performance. Simulation results are also plotted in Figure 3.9 and 10 for comparison purpose, and show a good match with the experimental results;

the tiny differences at the beginning and the end of the tracking could be due to unmodeled static friction and state estimation error.

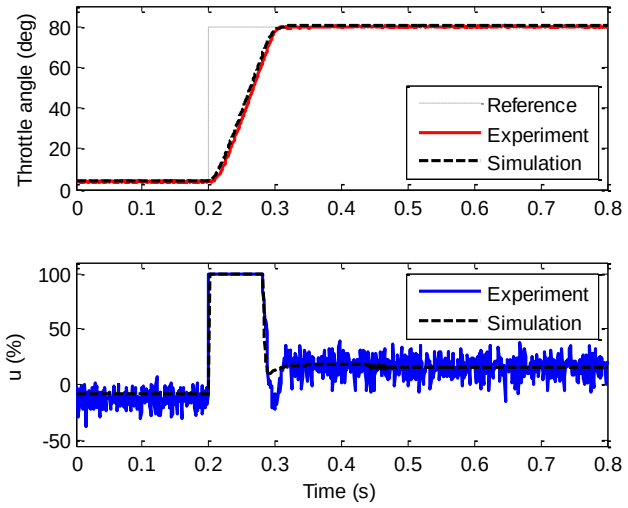

Figure 3. 9: Large opening case - rising

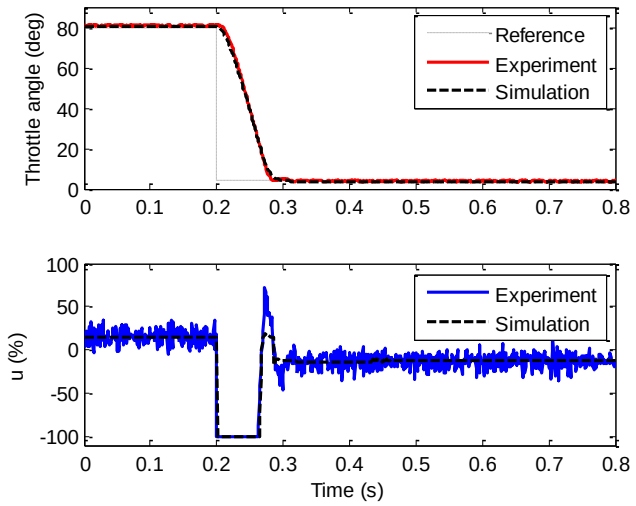

Figure 3. 10: Large opening case - falling

Figure 3.11 shows the system responses in case of crossing limp-home. Due to the effect of dual return springs, when the throttle plate crosses the LH position during the opening or closing operation, the DC motor has to overcome the preload torque in either direction, respectively. Thus any conventional linear controller without feed-forward control compensation (such as

fixed gain PID controller) will stop at the LH position for a while, leading to extended settling time. However, since a parameter-dependent feed-forward control u_0 was designed in the proposed control strategy to compensate the preload torque, the experiment result shows clearly that the throttle plate could cross the LH position fairly smoothly in both opening and closing cases; see Figure 3.11. An averaged tracking trajectory of 25 repeated cycles was also plotted in Figure 3.11 to reduce the sensor noise effect in the large scale.

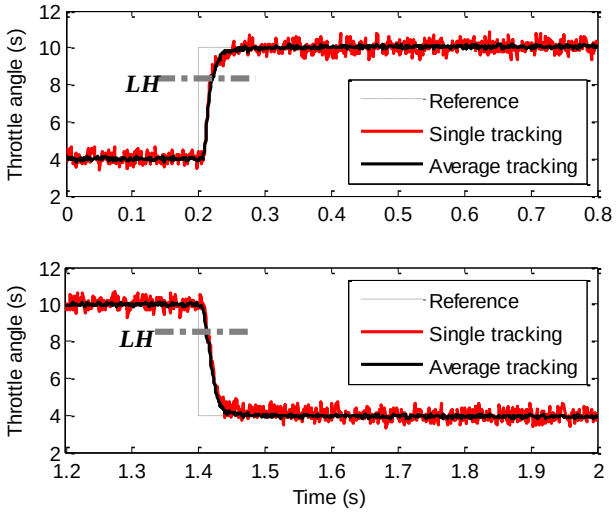

Figure 3. 11: Crossing limp-home case

When the throttle plate opens with a small angle, the engine is operated under a fairly low load. Manifold pressure is quite sensitive to the throttle angle within this operation range. Since the throttle position highly affects the engine combustion property, it is essential to control the throttle plate position accurately with fast response. Figure 3.12 shows a good performance with a small tracking angle between 4° and 6° , the 2% settling time is about 0.15s with no overshoot. The overlay of the single tracking trajectory under the 25-cycle averaged tracking also demonstrates that the response is repeatable. In the following paragraphs the proposed LPV

controller is compared with some commonly used controllers.

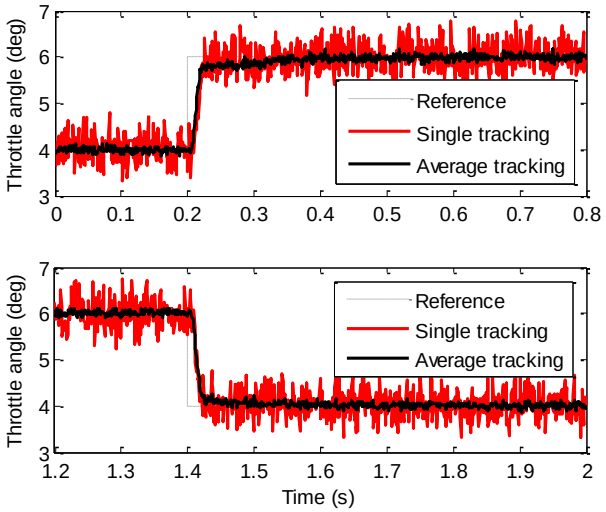

Figure 3. 12: Small opening case

Figure 3.13 compares the LPV controller with a well-tuned (fast response with no overshoot in a wide operation range) fixed gain PID controller. Note that the same reduced-order observer defined in (21) was used to estimate x_2 ($\dot{\theta}$) and used for derivative control in the PID controller to have a fair comparison. This PID controller is able to achieve quite similar performance as the LPV controller for the large opening case; however, for the small opening case it shows its weakness and its settling time is twice longer than that of the LPV controller. As shown in Figure 3.13, at the beginning of the rising period, these two controllers act almost the same; while approaching the target position, the response of the PID controller slows down significantly. The main reason is that Coulomb friction becomes significant under small angular velocity. The fixed gain PID controller cannot compensate this variation while the LPV controller takes the friction into consideration (modeled as a velocity dependent parameter) and the control gain is adjusted as a function of velocity.

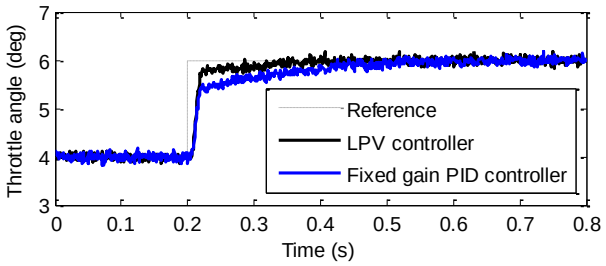

Figure 3. 13: Comparison with fixed gain PID controller

The other widely used control strategy is sliding mode control [42]-[43]. Here an anti-chattering type of sliding mode controller with integral control was used for comparison as follows.

$$u = \frac{1}{B_2}\left(A_{21}x_1 + A_{22}x_2 - \lambda_0 e_1 - \lambda_1 e_2 + \ddot{r} - \gamma - \beta \,\mathrm{sat}\left(\frac{s}{\varepsilon}\right)\right) \tag{41}$$

where the sliding surface is $s = \lambda_0 e_0 + \lambda_1 e_1 + e_2$ with $e_0 = \int e_1 dt$, $e_1 = x_1 - r$, and $e_2 = x_2 - \dot{r}$; the sub-index (i,j) is associated with the (i,j) element of matrix A or B in 3.6(a); and γ is the upper bound of the nonlinear term. Note that the saturation function was used to replace the sign function sgn(s) to reduce steady state chattering. Since there is a trade-off between convergence speed and the chattering phenomenon, a sequence of sliding mode controllers with different parameters were tested, as listed in Table III. The performance was also compared based upon the integral of the absolute tracking error between 4° and 6°; the last column of the table shows the maximal chattering magnitude of control signal u at steady state, due to the chattering phenomenon and sensor noise. It can be seen that the sliding mode control is capable of achieving better performance than the proposed LPV controller (sliding mode controller 2), but the control signal chatters severely at the steady state, which wastes a lot of control energy and could damage the mechanical system quickly; on the other hand, if the control is "soft" with

a small chattering (sliding mode controller 4), the tracking response becomes really slow.

Table 3. 3: Controller Performance Comparison

Controller	λ_1	β	ε	$\int \lvert e \rvert dt$	$\max \lvert \Delta u \rvert$
Sliding mode controller 1	50	1000	2	0.082	0.25
Sliding mode controller 2	50	2000	2	0.048	0.8
Sliding mode controller 3	100	1000	2	0.054	0.5
Sliding mode controller 4	50	1000	3	0.174	0.15
Sliding mode controller 5	50	1000	1	0.061	0.65
LPV controller				0.052	0.25

Sliding mode controller 1 provides the best balance between control energy and performance, thus it was selected to compare with the LPV controller in Figure 3.14. In order to observe the control signal, single tracking data was plotted instead of average data. It is obvious that with the similar control chattering magnitude, sliding mode controller provides slower tracking response than that of the LPV controller.

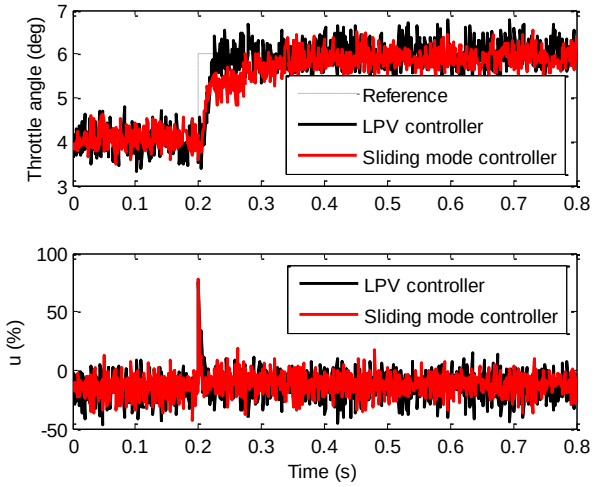

Figure 3. 14: Comparison with sliding mode controller

Finally, the robust performance of the throttle operation under battery voltage disturbance was studied. It is assumed that a stabilized throttle position is interrupted with a sudden vehicle

battery voltage change. For instance, this could happen during the engine crank start-up process. The performance of the LPV controller is compared with that of fixed gain PID controller with and without the feed-forward parameter dependent control u_0 in (7). Both battery voltage dropping and recovery cases were studied. Figure 3.15 shows the system responses when the battery voltage drops from 13V down to 7V within 10ms and remains at that level; the tracking error of the PID control without u_0 is about 1.5 degrees and it recovers within 0.8 second, while the fluctuation of throttle position is about 0.2 degree under PID control with u_0, and about 0.1 degree under LPV control. Figure 3.16 shows the case when the battery voltage recovers to its normal level. The tracking error of the PID control without u_0 is about 2.4 degrees and it recovers within 0.6 second, while the fluctuation of throttle position is about 0.4 degree under PID control with u_0, and about 0.1 degree under LPV control. Firstly, these results show the essential effect of the battery voltage depended u_0 in compensating the spring preload torque under any battery voltage condition. For the PID control without u_0, when the battery voltage changes, motor torque driven by the PID closed loop control cannot provide equivalent torque to compensate the spring preload torque, leading to a sudden tracking deviation which requires the integral term of the PID controller to compensate it gradually. This could be observed from the plot of control *u*, which changes immediately as battery voltage changes in the LPV controller, while it changes gradually for the PID controller. Secondly, due to the system modeling uncertainty u_0 might not fully compensate the preload torque; it could be seen that under the same u_0, the response of the LPV controller is still more robust than that of the PID controller. The reason is that LPV gain-scheduling controller adjusts its control gains as a function of the

battery voltage since battery voltage is one of the varying parameters. In this case, the control gains increase as the battery voltage drops. Combining both effects, the LPV controller provides the best performance.

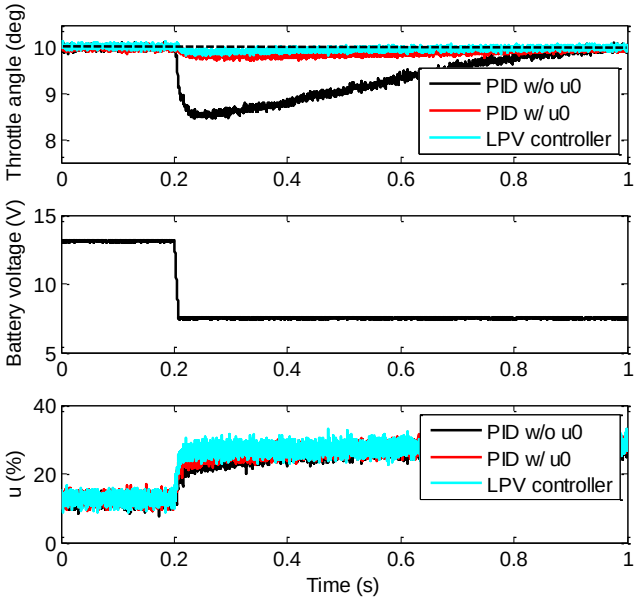

Figure 3. 15: Battery voltage drop case

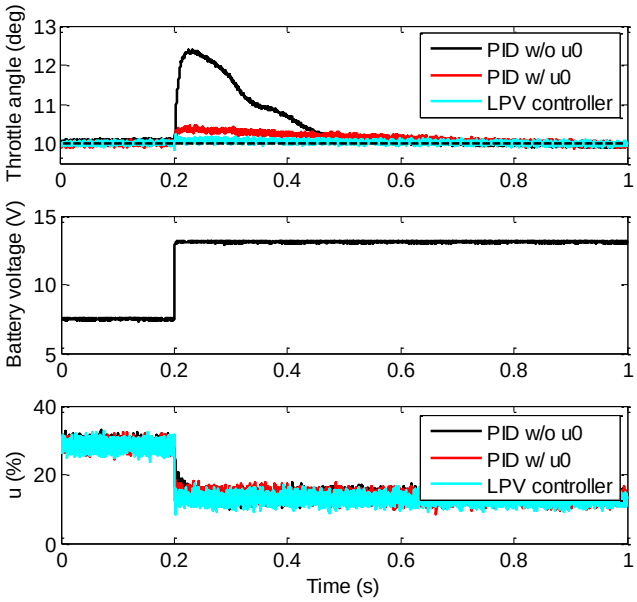

Figure 3. 16: Battery voltage recovery case

3.6 Conclusions

In this chapter a discrete-time gain-scheduling mixed constrained H_2/H_∞ controller was designed for an electronic throttle system based upon the LMI (linear matrix inequality) convex optimization scheme. To enable model-based control gain tuning, a sequence of the LPV controllers were designed with control effort from low to high by varying the H_2 constrain on control input and the designed controllers were evaluated through both simulation studies and experiment validation. The controller associated with the best performance was chosen for experimental validation and used for performance comparison with the conventional fixed gain PID (proportional-integral-derivative) and sliding mode controllers. The experimental results show significant tracking performance improvement of the LPV controller over the PID one, where the 2% settling time was reduced from 0.3 second (PID) down to 0.15 second (LPV). The LPV control also demonstrated superior performance under battery voltage variation with throttle plat held constant under 7 volts battery voltage step change.

CHAPTER 4

MODEL-BASED CONTROL FOR MODE TRANSITION BETWEEN SI AND HCCI COMBUSTION

4.1 Introduction

Due to the significant thermal and charge mixture differences between the HCCI and SI combustion, it is fairly challenging to achieve smooth mode transition between the SI and HCCI combustion. Note that the un-throttled HCCI combustion reduces pumping loss with relatively high in-cylinder temperature at intake valve closing (IVC) required by auto-ignition of HCCI combustion; while the SI combustion requires to be operated in a throttled mode with relatively low manifold pressure and temperature, especially around the combustion mode transition region. In [12] an experimental investigation on SI-HCCI-SI mode transition using hydraulic two-stage profile camshafts was performed, where the valve timing, one-step throttle opening timing, and fuel mass were optimized. However, considerable engine torque fluctuation during the combustion mode transition was observed. In [13] a state feedback controller was designed based on a state-space model obtained from system identification, fuel mass and negative valve overlap (NVO) were used as the control inputs to track the desired IMEP and combustion phasing. This model-based controller reduces torque fluctuation over the traditional PI (proportional and integral) controller, but engine torque output still varies unexpectedly, especially at the beginning of the mode transition. In [66] a control-oriented combustion model was linearized around the

steady-state SI and HCCI operational conditions, and a controller, composed of state-feedback and model-based feed-forward components, was used to control the fuel injection timing to track the desired combustion phasing without considering the hybrid mode combustion that starts with SI and ends with HCCI combustion. In [67] a model-based linear quadratic tracking strategy was used to track a desired manifold pressure to guarantee a reasonable air-to-fuel ratio and the fuel mass was controlled by using the iterative learning to maintain the torque at the desired level and the proposed control strategy was validated only in HIL (hardware-in-the-loop) simulations. Since the engine MAP was controlled based on the linearized intake dynamic model, which could lead to significant transition-by-transition variations. This could adversely affect the combustion stability during the mode transition.

In this chapter a model-based control strategy was developed to achieve smooth SI-HCCI combustion mode transition. The control strategy mainly consists of three parts: open-loop scheduled control, manifold pressure control for regulating charge air and fuel mass control for managing engine output torque. The valve lift, valve timing and spark timing are open-loop scheduled. By considering the filling dynamics of the intake manifold, a feed-forward control for the predetermined desired cycle-by-cycle throttle position was developed and an LPV closed-loop throttle position control strategy [50] was implemented to track the desired MAP (manifold air pressure) profile during the combustion mode transition. For the NMEP (net mean effective pressure) control, iterative learning approach was used to obtain the fuel mass at each transition cycle to maintain the engine NMEP at the desired level under any transition point; sensitivity-based feed-forward control was designed to compensate the potential NMEP

fluctuation due to the transition-by-transition variation (such as MAP variation). The developed control strategy was validated in a single-cylinder HCCI capable SI engine at four different transitional engine operational conditions.

This chapter is organized as follows. Section 4.2 describes the combustion mode transition control problem and provides a general control framework; based on the engine model described in Sections 4.3, manifold pressure control, fuel and NMEP control were presented in Sections 4.4 and 4.5, respectively. The associated experimental validation results are provided in Section 4.6. The last section adds some conclusions.

4.2 Mode Transition Control Problem

4.2.1 Engine configuration

As shown in Figure 4.1, the HCCI capable SI engine used for developing and validating the combustion mode transition strategy is a single cylinder engine equipped with EVVT systems for both intake and exhaust camshafts, dual-lift valve-train, and electronic throttle control (ETC) system. The LPV control strategy was used for precise and fast throttle position control [50]; and an OCC (output covariance constraint) controller [8] was used to accurately regulate the intake and exhaust valve timings. The intake air is heated by engine coolant through a heat exchange to around 350° K before entering the intake manifold to stabilize the HCCI combustion and extend the lean combustion limit. The engine was equipped with the in-cylinder pressure sensor to make it possible to calculate combustion characteristics such as NMEP and CA50 (crank position where 50% trapped fuel is burned). Table 4.1 lists the engine specifications.

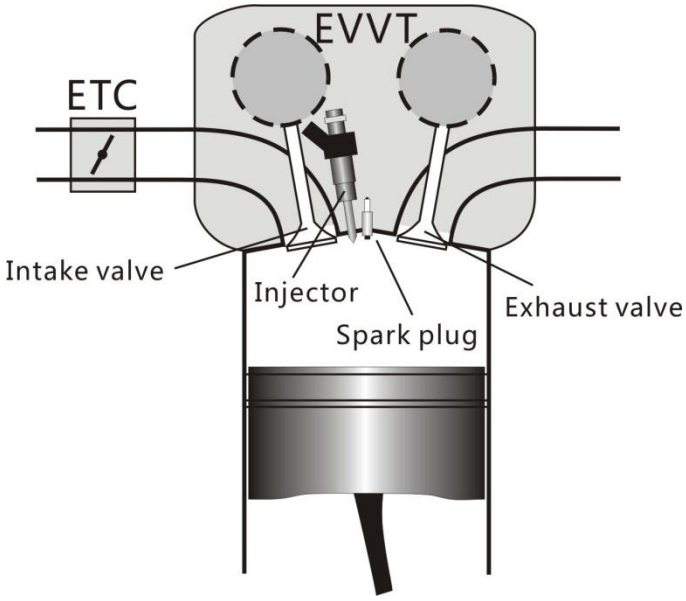

Figure 4. 1: Engine setup

Table 4. 1: Engine Specifications

Parameter	**Model value**
bore/stroke/con-rod length	86mm/86mm/151mm
compression ratio	12.7:1
Intake air temperature	350K
Intake/exhaust valve lifts-high	8.8 mm
intake valve opening duration-high	252 crank degree
exhaust valve opening duration-high	252 crank degree
Intake/exhaust valve lifts-low	4.4 mm
intake valve opening duration-low	148 crank degree
exhaust valve opening duration-low	148 crank degree

4.2.2 EVVT and NVO

SI and HCCI combustion requires quite different in-cylinder thermo-condition and charge mixture property. For instance, the engine is normally operated under mediate or low load when the mode transition is required between SI and HCCI combustion; see Figure 1.1. For example, during the mode transition from SI to HCCI combustion, before the transition the intake manifold pressure is relatively low due to throttled SI combustion and the engine is operated

under stoichiometric air-to-fuel ratio (AFR) required by the aftertreatment system; and after the transition the HCCI combustion is normally operated under a widely opened throttle with a relatively lean AFR and high exhaust-gas-recirculation (EGR), where the NVO is also utilized to trap a desired amount of the hot residual gas to manage the in-cylinder temperature at IVC, leading to high percentage of EGR. Managing the thermal-condition and charge-mixture property during the mode transition is the key for a smooth mode transition.

Figure 4.2 shows the cam profile with EVVT and dual-lift valve system. The dark solid curves show the cam profile in high valve lift, the dark dashed curves show the cam profile in low valve lift at the original position, and the grey solid curves show the phased cam profile in low valve lift for the required HCCI combustion. Both camshafts are able to phase 80° in crank angle.

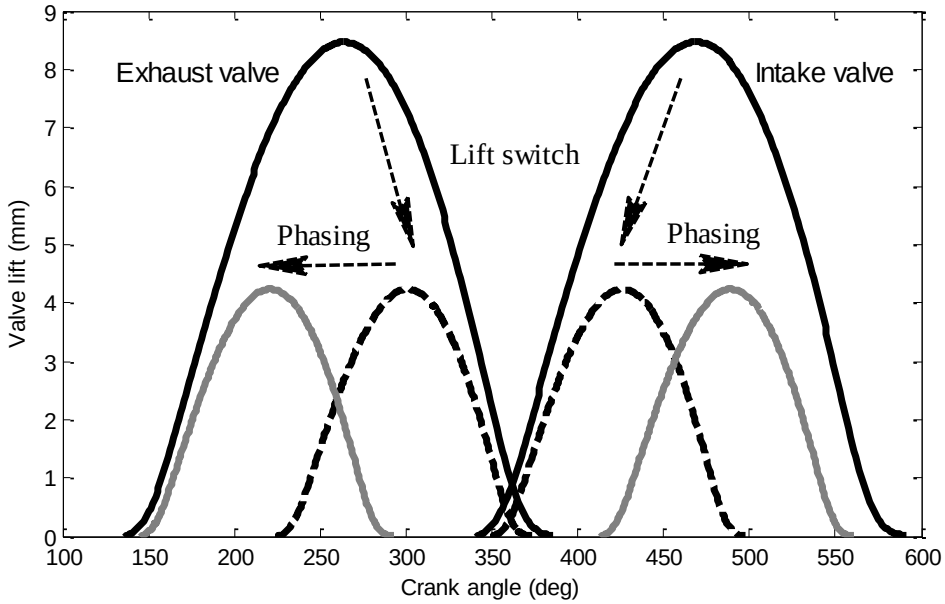

Figure 4. 2: Combustion performance with different pilot injection timing

One of the advantages of the EVVT system is that its operational performance is

independent of engine operating conditions such as engine oil temperature and pressure [8]. Hence with the fixed control system and driven actuator, the cycle-by-cycle performance of the EVVT can be easily determined, which is essential for EGR estimation, MAP and air-to-fuel ratio control strategy development. Figure 4.3 shows the in-cylinder pressure trace during the recompression phase (due to the NVO) under different cam phases of the EVVT at 2000 rpm. It took eight cycles for the cams to phase to the desired position for the HCCI combustion from its default SI location, and the internal EGR rate kept increasing which is reflected by the recompression pressure peaks.

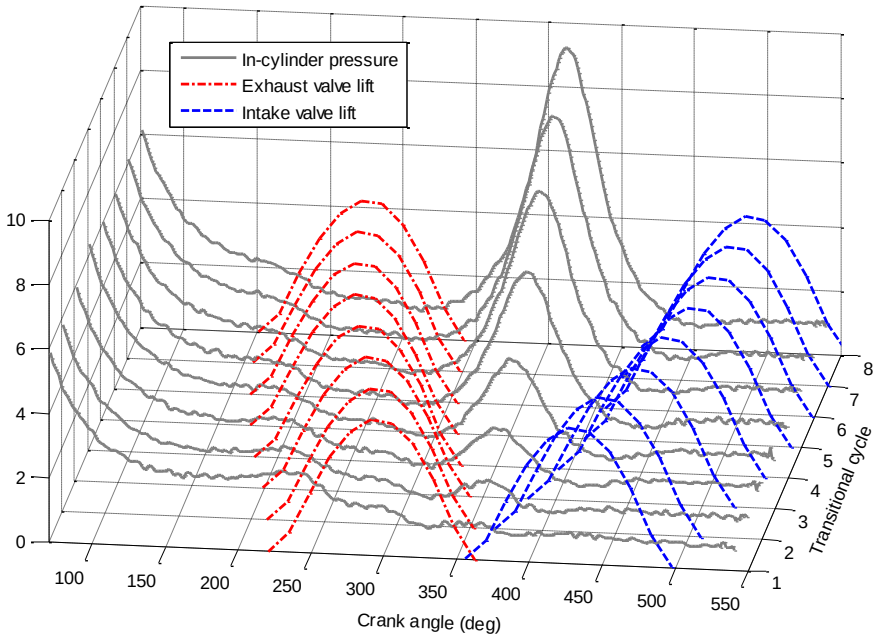

Figure 4. 3: EVVT action and in-cylinder recompression

4.2.3 Hybrid combustion mode

Theoretically, the HCCI combustion is initiated by auto-ignition; while the SI combustion is spark ignited without auto-ignition during the entire combustion process. However, there exists

another type of combustion that is a combination of SI and HCCI combustion, called hybrid combustion. Under this combustion mode, the combustion is initiated by the spark in the SI combustion mode and when the gas-mixture in the unburned zone satisfies the condition for auto-ignition, the HCCI combustion continuous in the unburned zone. This can be illustrated by the mass fraction burned (MFB) curve shown in Figure 4.4. Ignited by the spark, the hybrid combustion starts in the SI mode with a relatively slow heat release rate (see the solid curve between two circles); once the thermo condition of the auto-ignition in the unburned zone is satisfied, the combustion continues in HCCI mode with a relatively fast heat release rate (see the solid curve after the second circle). Hence the hybrid combustion mode is also called spark assisted HCCI combustion.

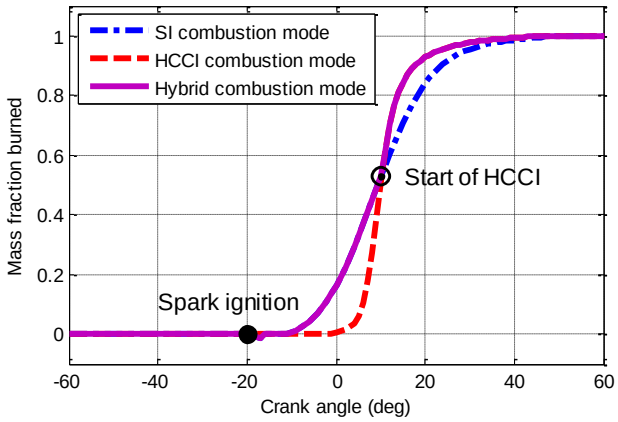

Figure 4. 4: Three types of combustion modes

The spark assisted HCCI combustion has been demonstrated to be able to improve the stability of HCCI combustion [69][70] and to expand the HCCI combustion operation limit to low load or high load [71][72]. Also it was used in the SI-HCCI combustion mode transition for achieving improved performance [71][73]. For the proposed mode transition strategy in this

study, the hybrid combustion is essential to the success of achieving smooth mode transition since the NVO level and manifold pressure are changing gradually between SI and HCCI conditions due to the slow EVVT response time.

Figure 4.5 shows an unsuccessful combustion mode transition from SI to HCCI at 2000 rpm without utilizing the hybrid combustion mode under relatively slow EVVT actuation. From the 3^{th} cycle, as the trapped residual gas increasing while the cam phasing starts, the spark timing was retarded and set to TDC at and after the 5^{th} cycle. Large drop of NMEP can be observed from cycles 4 to 7, along with large variations of CA50. By inspecting the in-cylinder pressure over these cycles during combustion transition shown in the left hand side of Figure 4.6, it can be observed that without the spark assistance, cycle 5 is under an ultra-late burning (see CA50 in Figure 4.5); and cycle 6 is almost misfired with very low NMEP (see Figure 4.5) due to the lean and high in-cylinder residual gas percentage. As a result, the unburned mixture along with the pilot injected fuel (to be discussed in the next subsection) resulted in an unexpected combustion during the NVO phase of cycle 6, leading to an extreme high pressure peak around 24 bar shown in Figure 4.5. This unexpected combustion during the NVO heats up the charge mixture at IVC of cycle 7, and triggered an ultra-early auto-ignition in cycle 7 with CA50 located at 25° BTDC with relatively low NMEP; see Figure 4.5. By utilizing the spark assisted hybrid combustion mode, the combustion performance can be significantly improved as shown in the right hand side of Figure 4.6. From the in-cylinder pressure traces it can be seen that the combustion starts with low heat release rate and switches to the HCCI combustion, which leads to the small bump for cycles 5 and 6; and the auto-ignition locations kept advancing from cycles 5 to 7 as the residual

gas percentage increases due to the graduate increment of the NVO by cam phasing. By scheduling the spark timing carefully, the combustion timing, represented by CA50, can be maintained properly to achieve a smooth combustion mode transition.

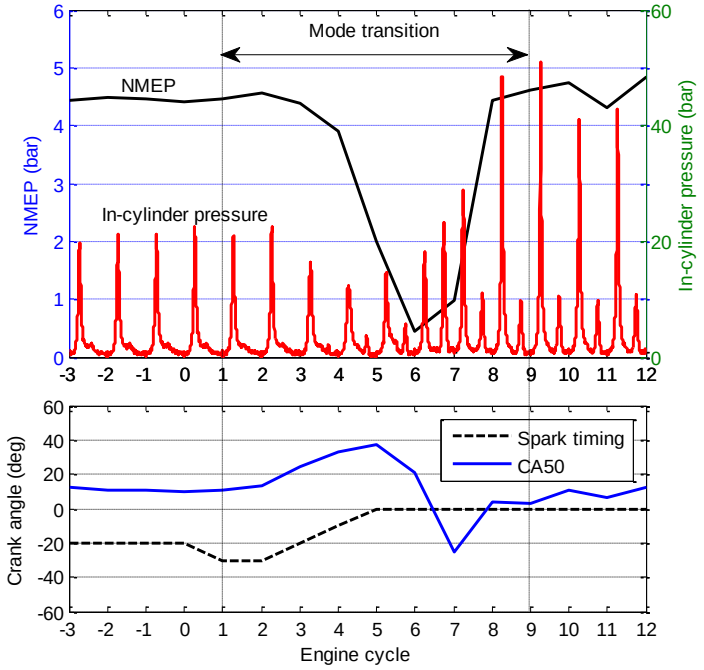

Figure 4. 5: An unsuccessful mode transition without hybrid mode combustion

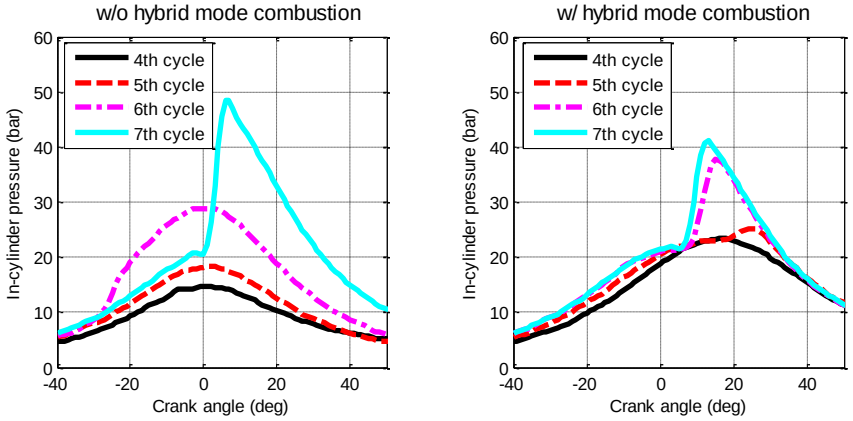

Figure 4. 6: In-cylinder pressure w/ and w/o assisted spark during mode transition

4.2.4 Split injection

Split injection is also widely used in the HCCI combustion [74][75]. By injecting certain amount of fuel into the hot residual gas during NVO phase, the reformed fuel stabilizes the auto-ignition and combustion timing for the HCCI combustion, especially at low load. Experimental results show that during the hybrid combustion cycles, pilot injection during the recompression is able to stabilize the HCCI combustion especially when the trapped residual gas is not high enough to initiate the auto-ignition.

To optimize the split injection strategy, a set of experiments of steady-state HCCI combustion with different pilot injection timings were conducted under different operational conditions. Figure 4.7 shows the experimental results for the engine operated at 2000 rpm with fuel mass of 13.8 mg, where 20% of the total fuel was injected during pilot injection and the pilot injection timing was varied from 320° to 360° ATDC (after top dead center). Note that the injection timing is defined as the end of injection pulse. It can be seen that there is a strong correlation between the pilot injection timing and CA50 (or NMEP). For this operational condition, 345° ATDC was chosen as the pilot injection timing for the highest NMEP and lowest COV (coefficient of variation). Figure 4.8 shows the corresponding fuel injection strategy, where the pilot injection is set to be 345° ATDC with 20% of the total fuel mass and main injection is set to be at 420° ATDC with 80% of the total fuel. Note that on the plot both of the injection pulse widths include 1 ms pre-charge period for the injector to reduce injection-to-injection variation and no fuel is injected during that period.

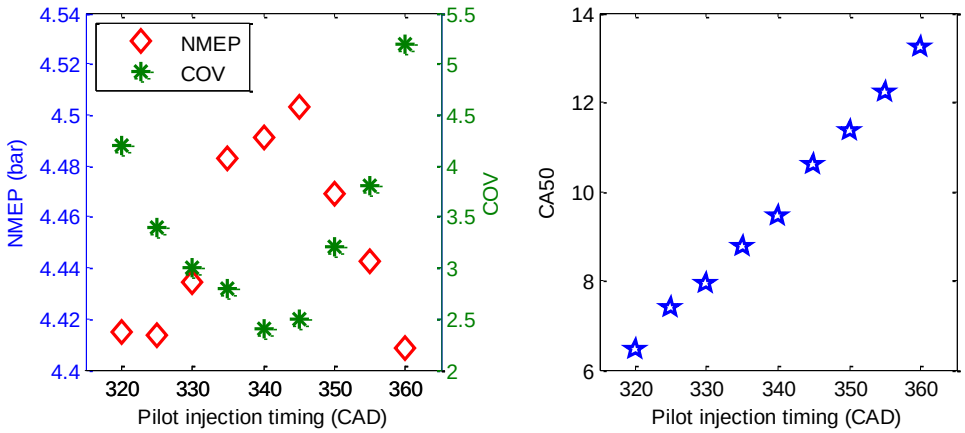

Figure 4. 7: Effects of pilot injection timing on the combustion performance

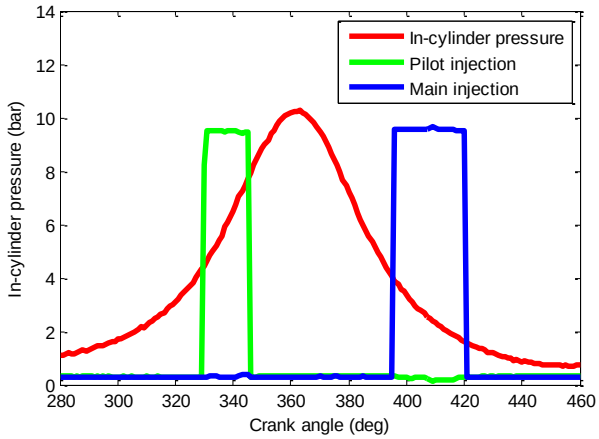

Figure 4. 8: Split injection strategy

4.2.5 Control problem

By combining the EVVT, split injection, and electronic throttle control using the hybrid combustion during the mode transition, the control strategy to achieve a smooth mode transition can be developed. Figure 4.9 shows the mode transition strategy for the SI to HCCI combustion mode transition when the engine is operated at 2000 rpm with 4.5 bar NMEP. Both of the intake and exhaust valves are switched from high lift to low lift at the beginning of mode transition. The intake valve was retarded by 63 crank degrees while the exhaust valve was advanced by 80 crank

degrees from the SI to HCCI combustion mode within 8 engine cycles. While the change of valve lift would result in a sudden change of in-cylinder temperature due to reduced effective compression ratio at the cycle from high to low lift, the spark timing was advanced significantly at the first transitional cycle to avoid the late combustion due to the reduced in-cylinder temperature caused by the declined effective compression ratio at the beginning of the transition. Starting with the 3rd cycle the single fuel injection was split into pilot and main injections to prepare for the following hybrid combustion; from the 6th cycle as the percentage of the HCCI combustion kept increasing in the hybrid combustion mode, the spark timing was retarded gradually to maintain the proper combustion timing; and finally at and after the 9th cycle the spark timing is remained at TDC (top dead center) for the stable HCCI combustion mode, which is used as a precaution in case of misfire. The throttle is opened step-by-step to follow the desired incremental MAP trajectory to maintain the normalized AFR between 1.0 and 1.2 such that the spark can reliably initiate the SI combustion for stable hybrid combustion. Figure 4.10 shows the in-cylinder pressure and AFR during a smooth mode transition using the proposed control strategy based upon the HIL simulation results. The AFR increases from stoichiometric SI combustion to lean (AFR=1.2) steady HCCI combustion mode gradually. It can be seen that as the MAP and AFR increase, the peak in-cylinder pressure increases gradually due to the increased rate of heat release in the SI-HCCI hybrid and HCCI combustion, and at the same time, the engine NMEP remained unchanged. As the exhaust valves gradually advances and intake valve gradually retards, the magnitude of pressure peaks during NVO phase also increases, which is indicated by the small peaks between the large in-cylinder pressure peaks in Figure 4.10

during the mode transition and HCCI combustion periods. For other transitional points, since the EVVT motion is independent of engine operational condition, the time-based valve opening trace is fixed, and the cycle-based spark timing and throttle opening could be determined similarly. Taking the transition at 1100 rpm as an example, the EVVT is able to complete the required cam phase adjustment within approximately 6 engine cycles, and the spark timing should start being retarded gradually from the 4th cycle, and the step-opening of throttle should be accelerated to ensure that the throttle is widely opened by the 5th cycle.

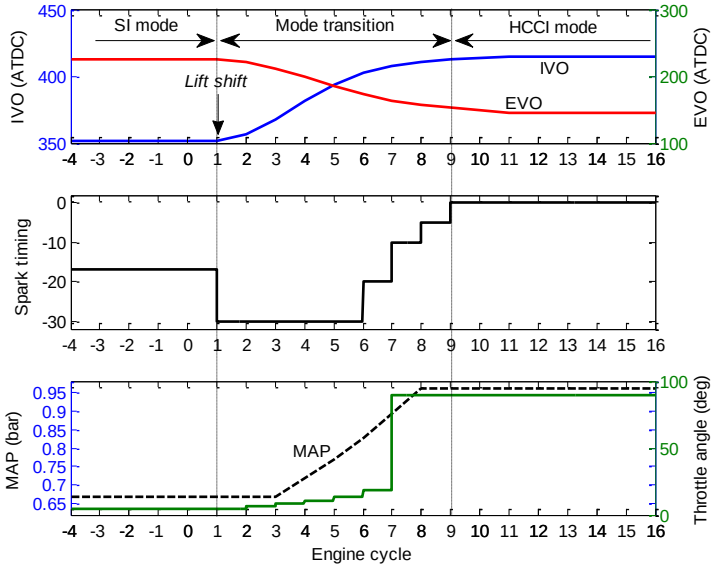

Figure 4. 9: Combustion mode transition strategy from SI to HCCI

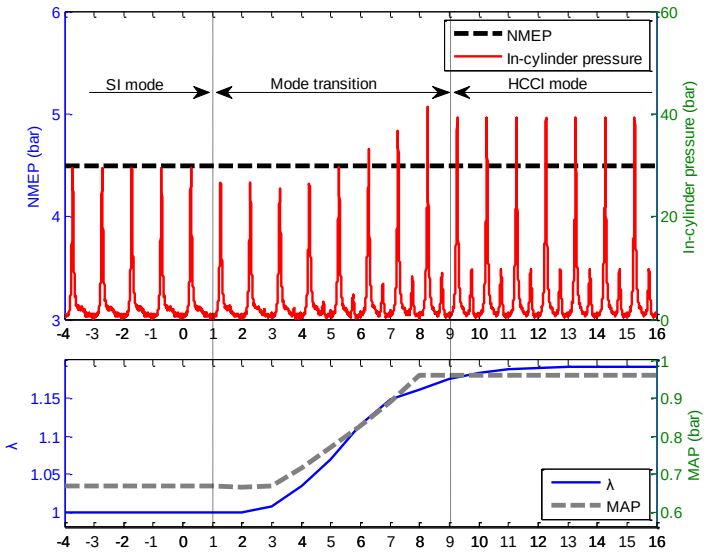

Figure 4. 10: Combustion performance during mode transition

For the case of combustion mode transition from HCCI to SI combustion, it is quite similar by reversing the order of all control sequences for the SI to HCCI mode transition. As shown in 0, the intake valve is advanced by 63 crank degrees while the exhaust valve is retarded by 80 crank degrees to transit to the steady SI operational condition. The MAP is required to follow a reversed control sequence shown in 0. However, it will take a few engine cycles for the MAP to reduce down to the desired level since the fresh air trapped in the manifold needs to be consumed by the intake process in a few engine cycles, hence, the MAP reduces at a slower rate than that in the case shown in 0. As a result, the throttle was closed immediately for the HCCI to SI mode transition, instead of a graduate step down operation. Consequently, between cycles 6 and 8, due to the relatively lean in-cylinder mixture, the spark timing needs to be further advanced to keep the combustion at the desired level.

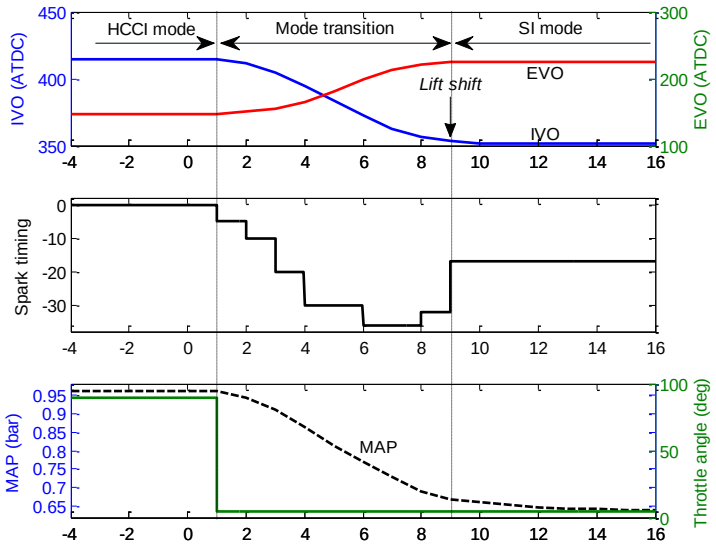

Figure 4. 11: Combustion mode transition strategy from HCCI to SI

4.2.6 Control framework

Figure 4.12 shows the architecture of the proposed model-based controller for combustion mode transition. The open-loop feed-forward control parameters are scheduled for spark timing, valve lift, intake and exhaust valve timings, the initial fuel mass of the iterative learning, and the reference throttle position to track the target MAP (see Section 4.4). The NMEP is controlled by regulating the fuel mass through iterative learning, and the sensitivity-based feed-forward controller adjusts the fuel mass to compensate the possible NMEP fluctuation by utilizing the measurement of CA50 of the last engine cycle and the MAP of current cycle; see Section 4.5. Note that is normally calculated based upon the measured in-cylinder pressure. During engine calibration process or steady-state operational condition, the iterative learning is turned on; and after the learning process converges, it could be turned off and the sensitivity-based compensation will continue for improved robustness. Note that the iterative learning gain cam

also be remained on with relatively small learning gain to make the control to be robust to engine aging and engine-to-engine variations.

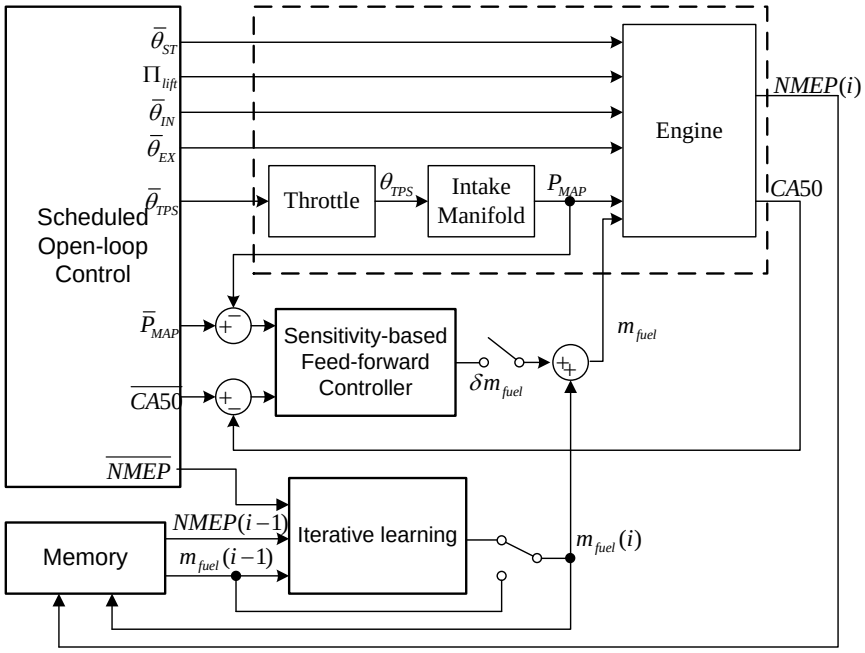

Figure 4. 12: Mode transition control diagram

4.3 Engine Combustion Modeling

In order to investigate the impact of intake charge action and fuel mass injected to the engine combustion characteristics, engine thermodynamics equations are derived for different combustion phases over the entire engine cycle. Figure 4.13 shows the definition of the engine cycle and its associated combustion events, where SOC, EOC, EVO, EVC, IVO, and IVC denote start of combustion, end of combustion, exhaust valve opening, exhaust valve closing, intake valve opening, and intake valve closing, respectively.

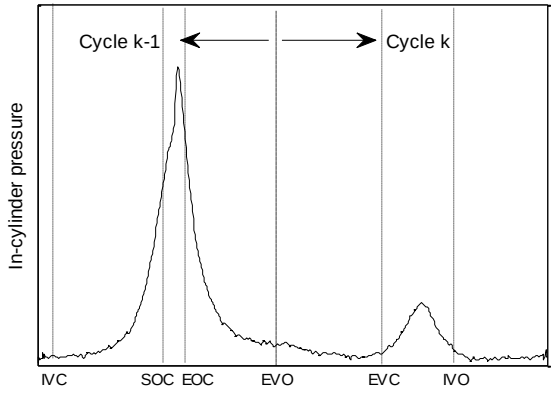

Figure 4. 13: Combustion events

EVO was used as the dividing point between cycles *k-1* and *k*, and the calculation of in-cylinder thermodynamics characteristics of cycle *k* was based on the measured in-cylinder pressure at cycle *k-1* and current intake manifold pressure at IVC of cycle *k*. Since the fuel injection timing was set to 300 degrees before TDC, which is close to IVO. All the parameters required for feed-forward fuel control shall be made available about 30° crank angle before fuel injection timing so that the engine control has enough time to schedule the fuel injection pulse; and the MAP at TDC before IVO was use instead of the MAP at IVO due to the assumption that the MAP at TDC and IVO is closed to each other. Modeled in-cylinder thermodynamics for different combustion phases is presented below.

4.3.1 Polytropic process

Polytropic process is assumed during the exhaust period (from exhaust valve opening to intake valve opening), compression, and expansion phases. Under the configuration of valve lifts and EVVT strategy, NVO starts from the second transition cycle once the valves have been shifted to the low lift. For polytropic process, the in-cylinder temperature at crank angle θ is

given by

$$T_\theta = T_e \left(\frac{V_e}{V_\theta} \right)^{n-1} \tag{4.1}$$

where the index *e* denotes the event of EVO, EVC, IVC, or EOC when θ locates within the exhaust, NVO, compression or expansion phase, respectively.

4.3.2 Charge mixing

During the intake phase, the residual gas and intake fresh charge can be considered separately. Firstly, the in-cylinder pressure at IVC is approximated to be equal to the intake manifold pressure, then the volume of the residual gas and the fresh charge can be obtained sequentially at IVC as follows:

$$V_{res}(k) = V_{EVC}(k) \left(\frac{P_{EVC}(k)}{P_{MAP}(k)} \right)^{1/n} \tag{4.2}$$

$$V_{air}(k) = V_{IVC}(k) - V_{EVC}(k) \left(\frac{P_{EVC}(k)}{P_{MAP}(k)} \right)^{1/n} \tag{4.3}$$

By the ideal gas law, the masses of the fresh charge and the average in-cylinder temperature are

$$m_{air}(k) = \frac{P_{MAP}(k) V_{air}(k)}{R T_{MAT}} \tag{4.4}$$

$$T_{IVC}(k) = \frac{P_{MAP}(k) V_{IVC}(k)}{\left[m_{res}(k-1) + m_{air}(k) + m_{fuel}(k) \right] R} \tag{4.5}$$

respectively.

4.3.3 Combustion process

Three combustion modes are investigated; and they are SI combustion mode applies for

transition cycles 1 to 5, SI-HCCI hybrid combustion mode for cycles 6 to 8, and HCCI combustion mode for cycles 9, 10, and beyond. Note that the in-cylinder temperature calculation can be simplified to be a sum of a polytropic volume change process and a heat release process [76]. In the SI mode, during the combustion process,

$$T_\theta(k) = T_{IVC}(k)\left(\frac{V_{IVC}(k)}{V_\theta}\right)^{n-1} + \frac{\eta Q_{LHV} m_{fuel}(k) x(\theta)}{mC_v} \tag{4.6}$$

where $m = m_{res}(k) + m_{air}(k) + m_{fuel}(k)$ is the total in-cylinder mass, η is the combustion efficiency, Q_{LHV} is the low heating value of the fuel, and $x(\theta)$ is the MFB (mass fraction burned) which can modeled by the Wiebe function. Note that MFB can also be calculated based upon the in-cylinder pressure [77].

In the HCCI combustion mode, since the combustion duration is much shorter than that in the SI mode, a constant volume heat release process can be assumed. Therefore, at the EOC

$$T_{EOC}(k) = T_{IVC}(k)\left(\frac{V_{IVC}(k)}{V_\theta}\right)^{n-1} + \frac{\eta Q_{LHV} m_{fuel}(k)}{mC_v} \tag{4.7}$$

For the SI-HCCI hybrid combustion mode, Arrhenius integral [79] is used to determine the start of HCCI (SOHCCI) combustion:

$$\int_{\theta_{IVC}}^{\theta_{SOC}} \frac{A}{N_e} e^{-\frac{E_a}{RT(\theta)}} d\theta = 1 \tag{4.8}$$

and the MFB is calculated before SOHCCI, which is represented by $x_{SI}(\theta)$. Consequently, at the switching point

$$T_{SI-HCCI}(k) = T_{IVC}(k)\left(\frac{V_{IVC}(k)}{V_\theta}\right)^{n-1} + \frac{\eta Q_{LHV} m_{fuel} x_{SI}(\theta)}{mC_v} \tag{4.9}$$

and at the EOC the in-cylinder temperature has the same expression as (4.7). The in-cylinder

pressure is obtained by ideal gas law for all of these three cases.

4.4 Manifold Pressure Control

Since the manifold filling dynamics is much slower than that of the electronic throttle, and pressure wave exists in the intake manifold due to the periodic engine intake valve events, a step-by-step manifold pressure feed-forward control strategy was developed. By using the ETC system in [50], for each engine cycle within the transition cycles, the throttle was set to a target position to achieve required manifold pressure, and the transient behavior of the throttle position was ignored due to its fast response time, which simplifies the calculation.

For the lean combustion circumstance, the fresh air prepared for combustion in cycle *k* consists of the newly charged air in (4.4) (cycle *k*) and also the unburned air in the residual gas from cycle *k*-1. Hence the normalized air-to-fuel ratio in cycle *k* is obtained by

$$\lambda(k) = \frac{m_{air}(k) + m_{air}(k-1)\left[\lambda(k)-1\right]}{14.6 m_{fuel}(k)} \tag{4.10}$$

The fuel mass $m_{fuel}(k)$ is expected to lie inside the range of fuel mass in steady SI mode and in steady HCCI mode. Based on a predetermined sequence of $\lambda(k)$, and controlled valve timing, required MAP can be obtained by Equations (4.3), (4.4), and (4.10).

Then consider the filling dynamics equation of the intake manifold

$$P_{MAP}(k) = P_{MAP}(k-1) + \frac{RT_{MAT}}{V_{man}}\left[m_{in}(k-1) - m_{out}(k-1)\right] \tag{4.11}$$

where T_{MAT}, V_{man}, m_{in}, and m_{out} denote the manifold temperature, manifold volume, intake air mass through the throttle to the manifold, and the air mass going to the cylinder from the

intake manifold, respectively. Note that m_{out} is easy to obtain by the scheduled nominal target and m_{in} can be obtained by the compressible flow equation below

$$\dot{m}_{in} = \varphi \frac{C_d \pi r^2 P_0 \sqrt{2\gamma/(\gamma-1)}}{\sqrt{RT_0}} \Psi\left(P_{MAP}\right) \tag{4.12}$$

During each engine cycle, the averaged manifold pressure $\bar{P}_{MAP}$ (where $\bar{P}_{MAP} = \left(P_{MAP}(k-1) + P_{MAP}(k)\right)/2$) is used as an approximation of P_{MAP} in Equation (4.2), therefore the target throttle position $\varphi(k)$ can be obtained that is also related to the engine speed.

4.5 Fuel and NMEP Control

The NMEP is defined as engine effective work done per unit volume over an engine cycle and it can be calculated the following integral

$$NMEP = \int p \mathrm{d}V \tag{4.13}$$

Since the in-cylinder pressure can be expressed as a function of the injected fuel mass, the intake manifold pressure, and the blowdown temperature at EVC from previous modeling analysis, the engine NMEP can also be written as

$$NMEP(k) = f\left(m_{fuel}(k), P_{MAP}(k), T_{EVC}(k)\right) \tag{4.14}$$

The control target is to maintain NMEP at the desired level by regulating the fuel mass for each transition cycle during the transition. In engine calibration process while repetitive operations are available, iterative learning control (ILC) [67][78] is an efficient approach to improve good tracking performance (fixed trajectory in this case) with simple control structure.

4.5.1 Iterative learning control

1） P-type iterative learning control

As the fuel mass m_{fuel} is the only control input, the nonlinear equation (14) can be partially linearized to obtain a simple state space for control purpose:

$$\begin{aligned} x(k+1) &= f\left(x(k)\right) + B(k)u(k) \\ y(k) &= x(k) \end{aligned} \tag{4.15}$$

where the $x(k) = NMEP(k)$ is the state, and B is the fuel sensitivity function which will be illustrated in the following subsection.

A P-type ([81] -[83]) ILC was used with a form of

$$u(i+1,k) = u(i,k) + K\left(y_d - y(i,k)\right) \tag{4.16}$$

where indexes i and k represent mode transition event number and engine cycle number for the given transition event, respectively; K is the proportional iterative learning gain; and y_d is the desired NMEP output. The system is stable if the learning gain satisfies that

$$\left|1 - K \cdot B(k)\right| \le 1 \tag{4.17}$$

which implies that

$$K \le 2/B(k) = 2\partial m_{fuel}(k)/\partial NMEP(k) \tag{4.18}$$

2） Robustness analysis

If the condition in (4.17) holds, the tracking error converges to zero as the iteration steps go to infinity assuming there are no external disturbances or measurement errors. However, in real engine applications, engine cycle-by-cycle variation can't be neglected. For mode transition, this cycle-by-cycle variation is mainly due to two reasons. One is that the engine combustion is

heavily dependent on in-cylinder turbulence for SI and HCCI combustion and the in-cylinder turbulence varies cycle-by-cycle; and the other is that the MAP tracking error and trapped mixture property variations caused by the previous combustion event.

Considering the following system with disturbance

$$\begin{aligned} x(k+1) &= f(x(k)) + B(k)u(k) + \eta(k) \\ y(k) &= x(k) \end{aligned} \tag{4.19}$$

and the disturbance

$$\eta(k) = \eta_1(k) + \eta_2(k) \tag{4.20}$$

is combined by η_1, defined as NMEP perturbation due to cycle-to-cycle variations of the turbulence charge-mixing, and η_2 , defined as NMEP perturbation due to the trapped mixture property variations of the previous engine cycle. Note that η_1 is difficult to be compensated due to its random nature and η_2 can be compensated by the sensitivity-based feed-forward control illustrated in the following subsection. It can also be shown that with bounded disturbance η_1, the convergence of system in (4.19) is guaranteed by the ILC law in (4.16) with a output tracking error bound in the form of

$$\lim_{i\to\infty} \sup |\delta y_i| \le f_1(K) + |\eta_1| f_2(K) \tag{4.21}$$

where $f_1(K)$ and $f_2(K)$ are functions of the learning gain *K*. More details are provided in [83]. Note that there is a tradeoff between the rate of convergence and the ILC robustness. That is, the high learning gain could result fast learning convergence with large steady-state error; while low learning gain leads to small steady-state tracking error but with slow learning convergence.

4.5.2 Sensitivity-based compensator

1） Sensitivity analysis

Let S_m, S_P, and S_T represent the NMEP sensitivities with respect to fuel mass, MAP, and exhaust temperature at EVC and they can be expressed as follows.

$$S_m(k)=\frac{\partial NMEP(k)}{\partial m_{fuel}(k)}=\left.\frac{\partial f}{\partial m_{fuel}(k)}\right|_{\bar{m}_{fuel}(k),\bar{T}_{EVC}(k-1),\bar{P}_{MAP}(k)} \tag{4.22}$$

$$S_P(k)=\frac{\partial NMEP(k)}{\partial P_{MAP}(k)}=\left.\frac{\partial f}{\partial P_{MAP}(k)}\right|_{\bar{m}_{fuel}(k),\bar{T}_{EVC}(k-1),\bar{P}_{MAP}(k)} \tag{4.23}$$

$$S_T(k)=\frac{\partial NMEP(k)}{\partial T_{EVC}(k-1)}=\left.\frac{\partial f}{\partial T_{EVC}(k-1)}\right|_{\bar{m}_{fuel}(k),\bar{T}_{EVC}(k-1),\bar{P}_{MAP}(k)} \tag{4.24}$$

where $\bar{m}_{fuel}(k)$, $\bar{T}_{EVC}(k-1)$ and $\bar{P}_{MAP}(k)$ denote the nominal values for fuel mass, MAP, and exhaust temperature at EVC under the current operational condition, and the same notation will be used in the following sections. Therefore, the first order approximation of (4.14) is

$$\delta NMEP(k)=\delta m_{fuel}(k)S_m(k)+\delta P_{MAP}(k)S_P(k)+\delta T_{EVC}(k-1)S_T(k) \tag{4.25}$$

Since the sensitivity-based feed-forward control target is to eliminate the NMEP fluctuation, by setting $\delta NMEP(k)=0$ the fuel mass correction can be obtained by

$$\delta m_{fuel}(k)=-\frac{1}{S_m(k)}\left[\delta P_{MAP}(k)S_P(k)+\delta T_{EVC}(k-1)S_T(k)\right] \tag{4.26}$$

The sensitivity functions $S_m(k)$, $S_P(k)$ and $S_T(k)$ is derived in the following subsections.

2） Sensitivity of fuel mass

The small deviation of the in-cylinder pressure and temperature during the compression phase caused by the evaporation of δm_{fuel} is ignored in this derivation. Then for the SI

combustion case, during the combustion phase

$$\bar{P}_\theta(k) = \frac{mR\bar{T}_{IVC}(k)}{V_\theta}\left(\frac{V_{IVC}(k)}{V_\theta}\right)^{n-1} + \frac{\eta Q_{LHV}\bar{m}_{fuel}(k)x(\theta)}{C_v V_\theta} \tag{4.27}$$

And as a result, assuming that the MFB does not change due to small variation of the fuel mass, the instantaneous in-cylinder pressure deviation is

$$P_\theta(k) - \bar{P}_\theta(k) = \frac{\eta Q_{LHV}\delta m_{fuel}(k)x(\theta)}{C_v V_\theta} \tag{4.28}$$

Note that the NMEP variation due to fueling mass based upon the MAP deviation is relatively small; hence the integral of pressure-to-volume within this period was omitted. During the combustion phase it can be expressed as

$$\begin{aligned}\int_{SOC}^{EOC}\left[P_\theta(k) - \bar{P}_\theta(k)\right]\mathrm{d}V_\theta &= \int_{SOC}^{EOC}\frac{\eta Q_{LHV}\delta m_{fuel}(k)x(\theta)}{C_v V_\theta}\mathrm{d}V_\theta \\ &= \delta m_{fuel}(k)\int_{SOC}^{EOC}\frac{\eta Q_{LHV}x(\theta)}{C_v V_\theta}\mathrm{d}V_\theta\end{aligned} \tag{4.29}$$

And during the expansion,

$$\begin{aligned}\int_{EOC}^{EVO}\left[P_\theta(k) - \bar{P}_\theta(k)\right]\mathrm{d}V_\theta &= \int_{EOC}^{EVO}\frac{\eta Q_{LHV}\delta m_{fuel}(k)}{C_v V_\theta}\left(\frac{V_{EOC}(k)}{V_\theta}\right)^n \mathrm{d}V_\theta \\ &= \delta m_{fuel}(k)\int_{EOC}^{EVO}\frac{\eta Q_{LHV}}{C_v V_\theta}\left(\frac{V_{EOC}(k)}{V_\theta}\right)^n \mathrm{d}V_\theta\end{aligned} \tag{4.30}$$

Since all the parameters containing in the integrals of Equations (4.29) and (4.30) are available for offline calculation, the sensitivity function of fuel can be finally obtained as follows.

$$S_m(k) \cong \int_{SOC}^{EOC}\frac{\eta Q_{LHV}x(\theta)}{C_v V_\theta}\mathrm{d}V_\theta + \int_{EOC}^{EVO}\frac{\eta Q_{LHV}}{C_v V_\theta}\left(\frac{V_{EOC}(k)}{V_\theta}\right)^n \mathrm{d}V_\theta \tag{4.31}$$

The derivation of $S_m(k)$ in the HCCI mode and SI-HCCI hybrid mode is similar, thus omitted here.

3） Sensitivity of intake manifold pressure

The change of intake manifold pressure results in variations of air charge mass, the in-cylinder temperature and air-to-fuel ratio. This consequently affects the engine NMEP. Under lean combustion operational condition with high percentage of residual gas, CA50 deviation, caused by air-to-fuel ratio change, is the dominant factor for NMEP fluctuations. Experimental results also reveals the strong relationship between CA50 and MAP deviations that can be expressed by

$$\delta CA50(k) \cong \delta P_{MAP}(k) \frac{1250\left[\overline{\lambda}(k)\text{-}1\right]^{1.5} e^{-50\left[\overline{\lambda}(k)\text{-}1\right]^{2.5}}}{\overline{P_{MAP}}(k)} \tag{4.32}$$

and the effect of CA50 deviation to NMEP can also be approximated by

$$\delta NMEP(k) \cong -0.2\left[\left(1+0.0085\left(\delta CA50(k)\right)^2\right)^{0.6} - 1\right]\overline{NMEP}(k) \tag{4.33}$$

see similar approximation in [84].

Finally the sensitivity function of the intake manifold pressure $S_P(k)$ can be calculated by combining Equations (4.32) and (4.33).

In the HCCI combustion mode, since the throttle is widely opened, the manifold pressure would remain unchanged and $S_P(k)$ is set to be zero.

4） Sensitivity of in-cylinder temperature

In the hybrid combustion mode, change of in-cylinder temperature affects the auto-ignition timing, which is the major factor of the NMEP deviation. The in-cylinder temperature of cycle *k*

is mainly affected by the trapped residual gas temperature from the previous cycle (*k-1*); the compensated fuel mass δm_{fuel} also leads to temperature variation. While the in-cylinder temperature is not measurable, CA50 can be used as a replacement measurer. Due to the page limitation, only the final calculation results are shown in this subsection. The in-cylinder temperature variation at EVC can be obtained by

$$\begin{aligned} T_{EVC}(k)-\bar{T}_{EVC}(k) \cong & \frac{\eta Q_{LHV}}{C_v V_{EVO}^{n-1}(k-1)} \cdot \\ & \left[m_{fuel}(k-1)\left(V_{CA50}(k-1)^{n-2}\right)-\overline{m_{fuel}}(k-1)\left(V_{\overline{CA50}}(k-1)^{n-2}\right)\right] \end{aligned} \tag{4.34}$$

Then the deviation of in-cylinder pressure at IVC is in the form of

$$\begin{aligned} & T_{IVC}(k)-\bar{T}_{IVC}(k) \\ & \cong \delta T_{EVC} \frac{\bar{P}_{MAP}(k) V_{IVC}(k)}{\bar{m}(k-1) R} \Bigg/ \left[\frac{1}{\bar{T}_{EVC}} - \frac{\bar{P}_{MAP}^{(n+1)/n}(k) \bar{P}_{EVC}^{(1-n)/n}(k-1)}{n T_{MAT}} \right] \\ & =: g(k) \delta T_{EVC} \end{aligned} \tag{4.35}$$

The deviation of auto-ignition timing with respect to the deviation of T_{IVC} is provided in [80] through first order approximation approach. The complete sensitivity function is

$$\begin{aligned} S_T(k) \cong & \int_{IVC}^{SOC} \left(\frac{V_{IVC}(k)}{V_\theta} \right)^n \mathrm{d}V_\theta + \int_{SOC}^{EVO} \frac{mRg}{V_\theta} \left(\frac{V_{IVC}(k)}{V_\theta} \right)^{n-1} \mathrm{d}V_\theta \\ & + \left[\overline{P_{EOC}}(k) - \overline{P_{SOH}}(k) \right] \frac{lg(k) E_A}{R \bar{T}_{IVC}^2(k)} e^{-\frac{E_A}{R T_{\overline{SOH}}(k)}} \int_{IVC}^{\overline{SOH}} \left(\frac{V_\theta}{V_{IVC}(k)} \right)^{1\text{-}n} e^{-\frac{E_A}{R T_\theta(k)}} \mathrm{d}\theta \end{aligned} \tag{4.36}$$

where the index *SOH* denotes the crank position associated with the start of auto-ignition (HCCI mode) during the hybrid combustion cycles, and $l = \partial V_\theta / \partial \theta |_{\overline{SOH}}$.

In the SI combustion mode, the effect of in-cylinder temperature of cycle *k-1* to the combustion of cycle *k* is minimum, and hence, $S_T(k)$ is set to zero.

4.6 HIL Simulation Validation

The proposed controller was first validated in HIL simulation environment as described in chapter 2 and Figure 2.7. The developed two-zone combustion engine model was used to replace the new engine, which is running in the dSPACE based host computer. Firstly, Figure 4.14 shows the throttle response and intake manifold pressure trajectory during mode transition, and the actual MAP signal matches the target MAP very well. Instantaneous MAP waves could also be observed in the figure, which is mainly due to the periodic manifold filling dynamics.

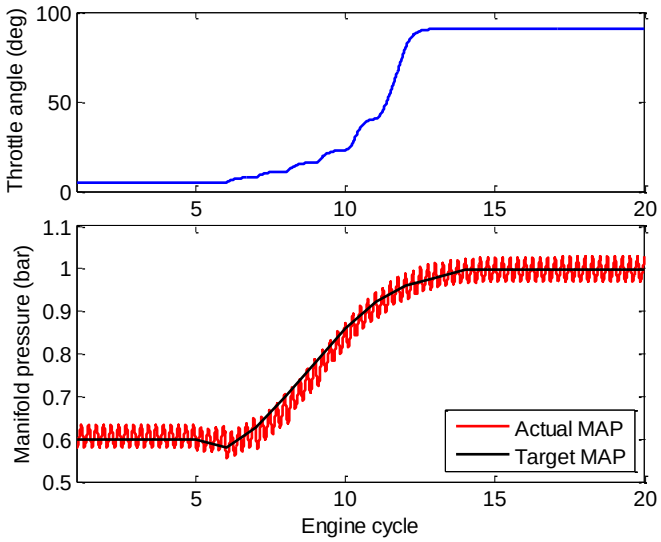

Figure 4. 14: Intake manifold pressure during mode transition

Secondly, the iterative learning control of fuel and NMEP was validated at 2000 rpm from SI to HCCI. Figure 4.15 shows the learned fuel mass for each transitional cycle at different learning iterations, and Figure 4.16 shows the resulted NMEP during transition. The initial fuel mass for the first three single injection cycles was set to be the same as that under steady SI combustion, and for the latter five engine cycles dual injection pulse widths were set to be identical to that under steady HCCI combustion. For the first mode transition, as the fuel mass is

relatively low during the last five transitional cycles, large drop of NMEP could be observed (see red curve in Figure 4.16). By the iterative learning, fuel mass was increased significantly for these five cycles (see yellow curve in Figure 4.15) at the 2nd learning iteration, and as a result, the NMEP level was also improved (see yellow curve in Figure 4.16). Then after 5 learning iterations, the fuel mass for each transitional cycle converged, and shows a continuous decrease from cycle 1 to cycle 8, due to the reducing pumping loss and increasing fuel economy. The NMEP fluctuation was maintained within 0.094 bar, which demonstrated a smooth combustion mode transition has been achieved.

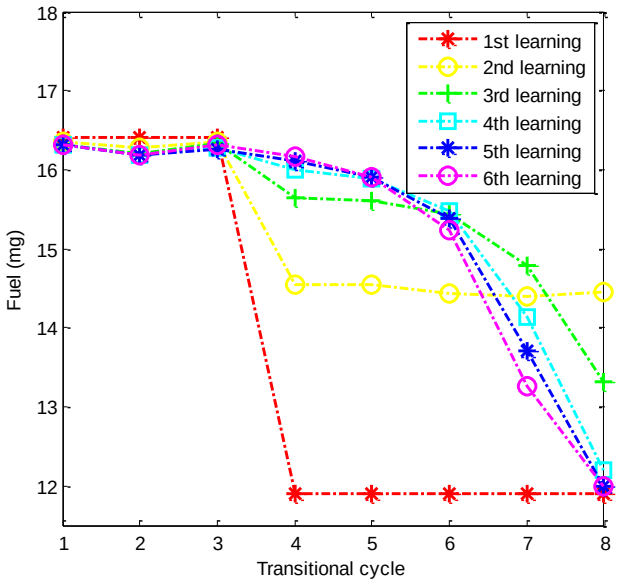

Figure 4. 15: Iterative learning of fuel mass

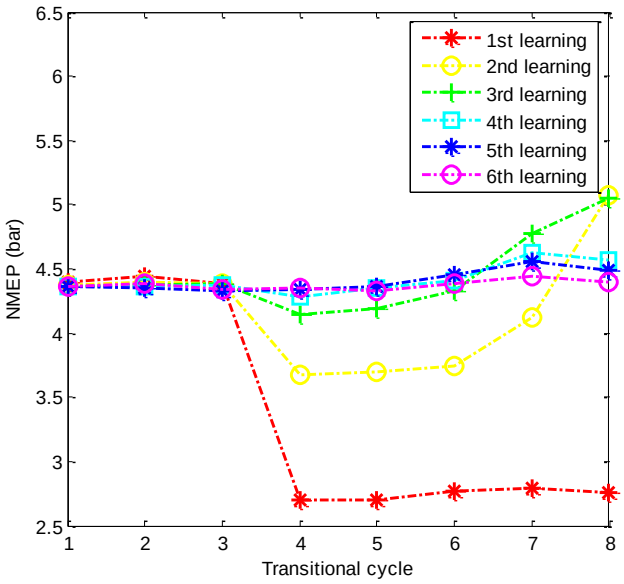

Figure 4. 16: Resulted NMEP under iterative learning control

Thirdly, in order to validate the proposed sensitivity-based feed-forward control strategy, the engine MAP dynamics were disturbed by an error introduced on the throttle opening during the transition. First a lower MAP case (that throttle opening is below the desired level) was simulated, and the result was shown in Figure 4.17. Note that filtered MAP traces were plotted to provide a clean vision of the MAP deviation. Under open-loop nominal controller, it can be seen that the NMEP fluctuation is more than 7% during mode transition under very small MAP deviations. However, with sensitivity-based feed-forward controller, a correction of the fuel injection quantity was realized to compensate for the possible deviation of NMEP, which reduces the transient NMEP fluctuation down to 0.5%. The other observation is that under open-loop control, a higher NMEP was shown for cycles 9 to 10, and a lower NMEP was shown for cycles 11 to 12. The reason is that for the hybrid combustion mode, a higher in-cylinder temperature will result in an increased HCCI combustion percentage and a reduced SI combustion percentage,

which could increase the combustion efficiency; and however in the pure HCCI combustion mode, the early combustion phase could lead to reduced thermal efficiency.

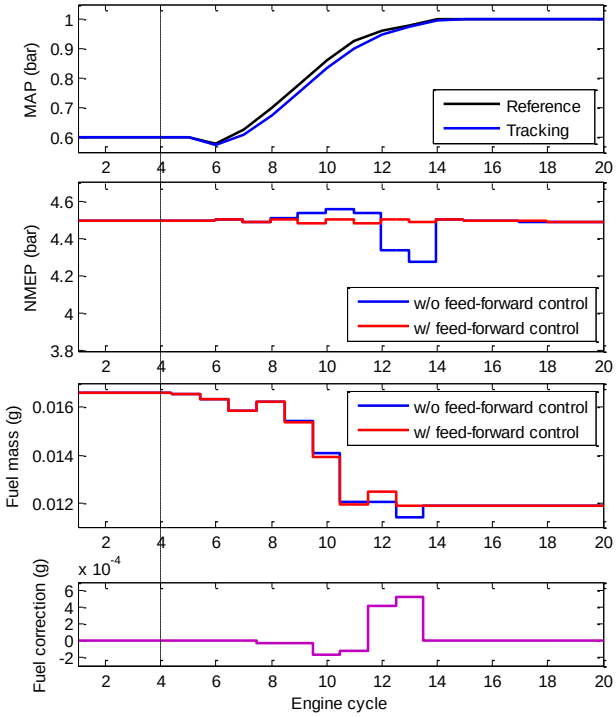

Figure 4. 17: Low MAP case validation

Figure 4.18 shows a high MAP case. It is clear that under the open-loop control, there was a sharp drop of the NMEP during the transition. The main reason is that the high MAP leads to high in-cylinder pressure during the compression phase, which could increase the pumping loss; while on the other hand the unchanged fuel injection mass would not provide additional work to compensate that loss. Under sensitivity-based feed-forward control, the fuel injection mass compensation leads to much smooth transient NMEP. From Figure 4.18, the NMEP fluctuation was reduced from around 14% down to 0.5%.

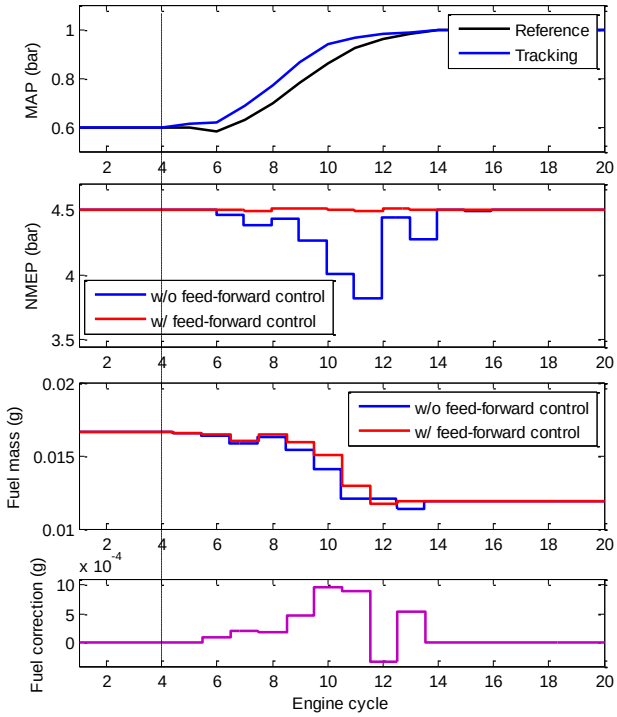

Figure 4. 18: High MAP case validation

4.7 Experimental Validation

The finalized controller shown in Figure 4.12 was then implemented into the MSU Opal-RT based prototype engine controller, and tests were conducted on an HCCI capable SI engine described in Section II. The instantaneous engine performance parameters were measured (such as valve timing, manifold pressure, and in-cylinder pressure) and calculated (such as NMEP, CA50) by Opal-RT engine controller in real-time.

Firstly, the mode transition from SI to HCCI was studied at 2000 rpm with 4.5 bar NMEP. Figure 4.19 shows the manifold pressure tracking results for a sequence of 10 mode transition cases. It can be seen that the manifold pressure follows the desired trajectory very well, the maximum tracking error (mostly occurs between the 5^{th} and 7^{th} cycles) is about 0.03 bar (5%),

and the maximum resulting air-to-fuel ratio tracking error is also about 0.05 (5%). This error is small enough for the sensitivity based control to compensate the resulting deviation.

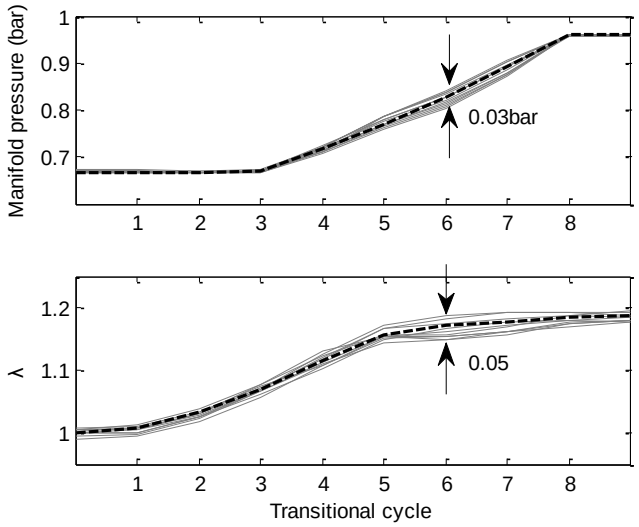

Figure 4. 19: Manifold pressure tracking

Figure 4.20 shows the iterative learning results without sensitivity-based fuel compensation, and the learning gain was selected as follows

$$K = S_m(k) = \partial NMEP(k) / \partial m_{fuel}(k)$$

Similar to the simulation validation, the initial fuel mass for the first three single injection cycles was set to be the same as that under steady SI combustion, and for the latter five engine cycles dual injection pulse widths were set to be identical to that under steady HCCI combustion. It could be seen that at the first learning iteration the deviation of NMEP is fairly large, especially around 4^{th} to 5^{th} cycles, where the charge mixture is relatively lean with a large percentage of residual gas existing. With the selected learning gain, the NMEP error reduced very fast but remained within a range of about 0.5 bar thereafter.

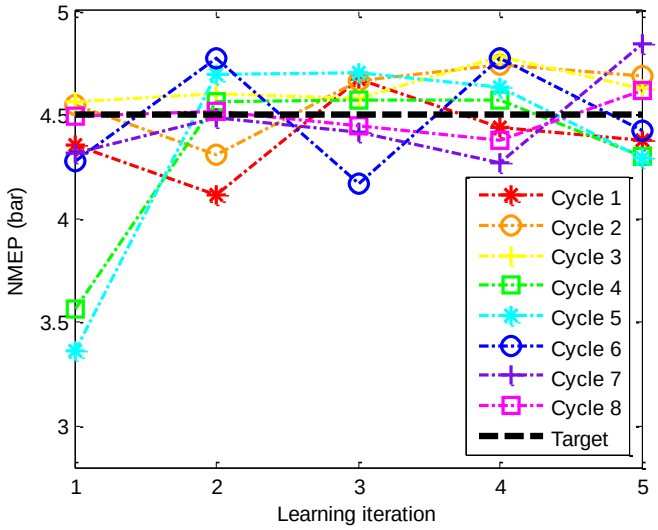

Figure 4. 20: Iterative learning w/o sensitivity compensation

Figure 4.21 shows a much better learning performance with the sensitivity compensation under the same operational condition, and with the learning gain chosen to be $K = S_m(k)/2$.

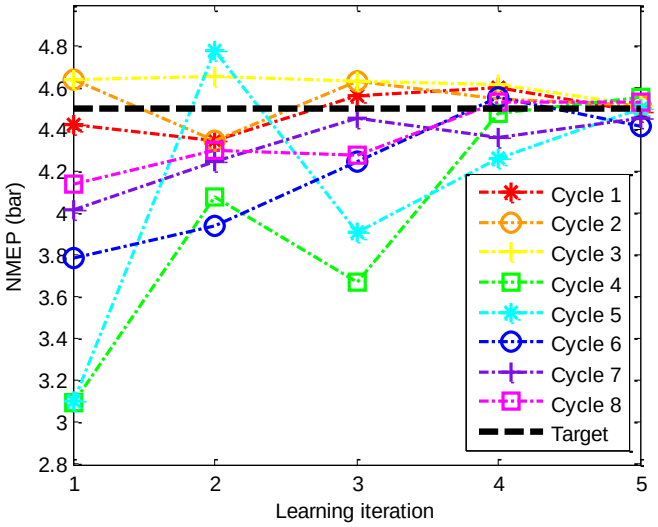

Figure 4. 21: Iterative learning with sensitivity compensation

The engine NMEP of all the transition cycles converges to the target in a little bit slower pace, but remains within a smaller error window around 0.1 bar. Note that there are still NMEP fluctuations during the transition especially for cycles 4 and 5, where the fuel sensitivity is far

away from the linear range; however, the learning still shows a good convergence at the end.

From Figure 4.22 it can be observed that during the learning iterations, for each learning iteration the updated fuel mass reduces for the first three cycles and increases for the next five cycles. After five learning iterations, the resulted fuel mass continuously reduces from the first cycle to the last cycle. The reason is that as the throttle is opened, the pumping loss is gradually reduced, leading to improved fuel economy. That is, less fuel is required to remain the same NMEP.

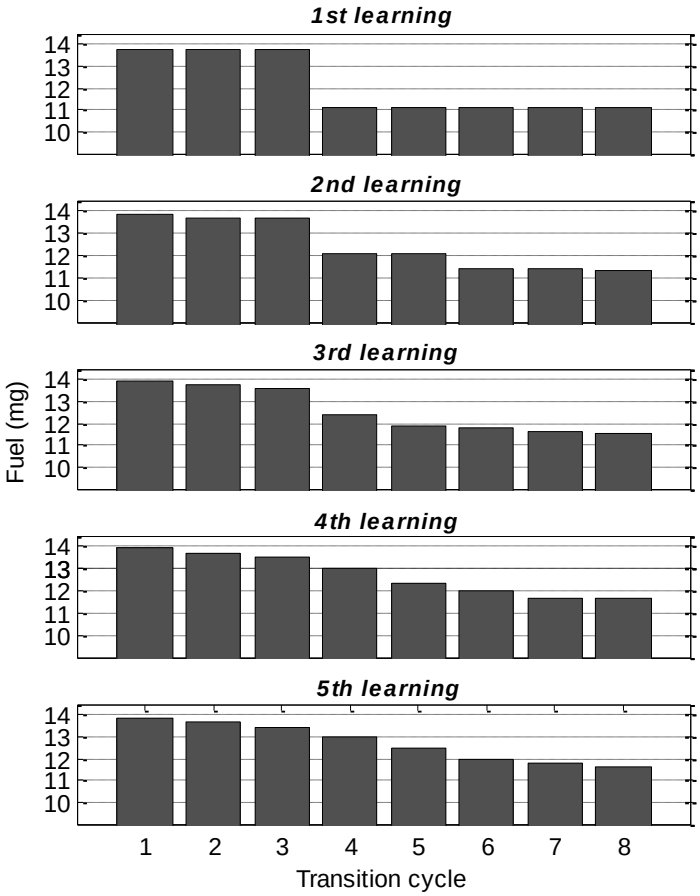

Figure 4. 22: Iterative learning of injected fuel mass

Taking the fuel mass learning process for the 6th cycle as an example, Figure 4.23 shows the

uniform fuel mass convergence, where the total fuel is modified by the sensitivity-based compensation to reduce possible cycle-by-cycle variation, and learning error due to system uncertainty as well.

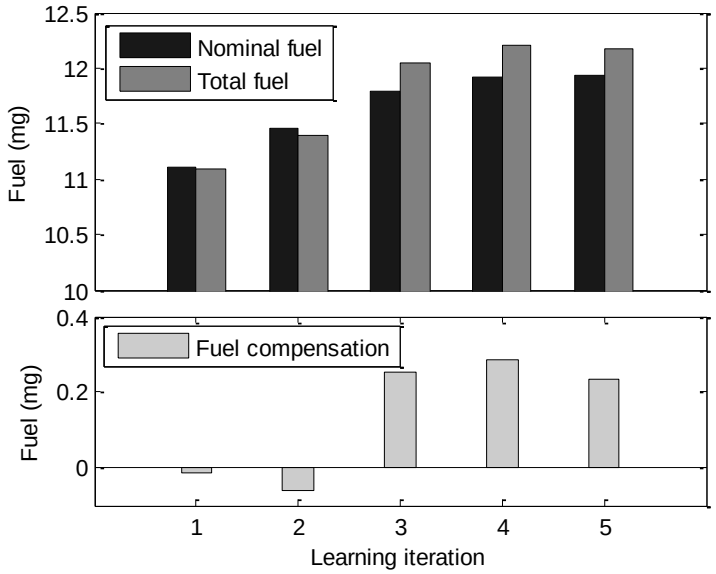

Figure 4. 23: Fuel mass learning in the 6th cycle

Once the iterative learning is converged, the fuel quantity can be fixed or the learning gain can be reduced significantly. Figure 4.24 shows a continuous 10 transitions under the fixed learned fuel strategy with or without sensitivity-based compensation. Due to the cycle-by-cycle variations caused by uncontrolled flow characteristics, certain NMEP fluctuation is expected for both cases; however, the maximum error reduced greatly from ±0.424 bar to ±0.171 bar when the sensitivity-based compensation control was turned on. Significant improvement was achieved especially for those cycles at the middle of transition, where the cycle-by-cycle variation is dominated by the fluctuation of manifold pressure, which results combustion phase shifting.

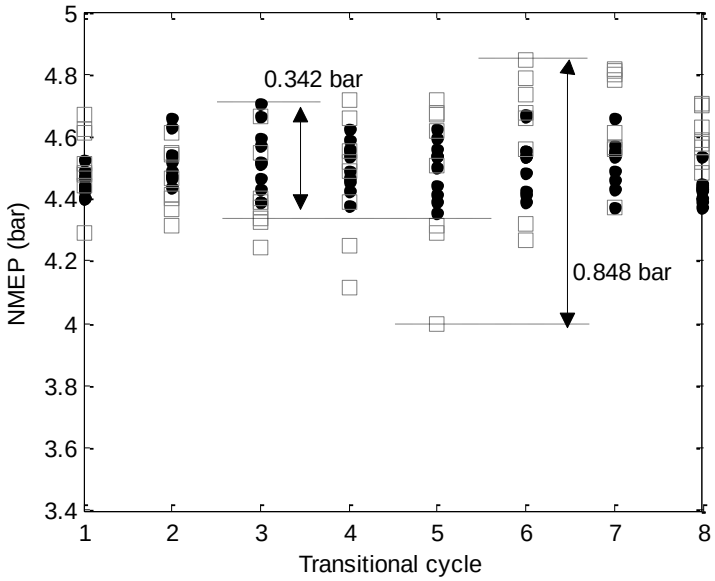

Figure 4. 24: Comparison with fixed gain PID controller

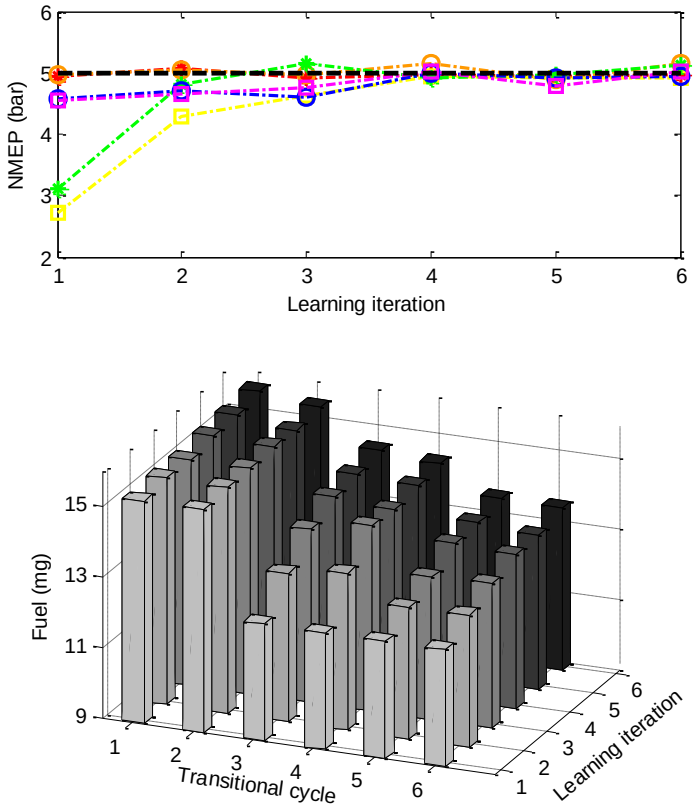

Figure 4. 25: Mode transition from SI to HCCI at 1500rpm with 5.0 bar NMEP

In Figure 4.25 to Figure 4.27 other combustion mode transition cases were studied at different engine operational conditions, including transition from SI to HCCI at 1500 rpm with 5.0 bar NMEP, transition from HCCI to SI at 2000 rpm with 4.5 bar NMEP and at 1500 rpm with 5.0 bar NMEP. Due to the figure size limitation, legend was omitted in these figures but they are the same as those in Figure 4.20 and Figure 4.21. Good convergences are shown for all of these cases within 5 to 6 learning iterations.

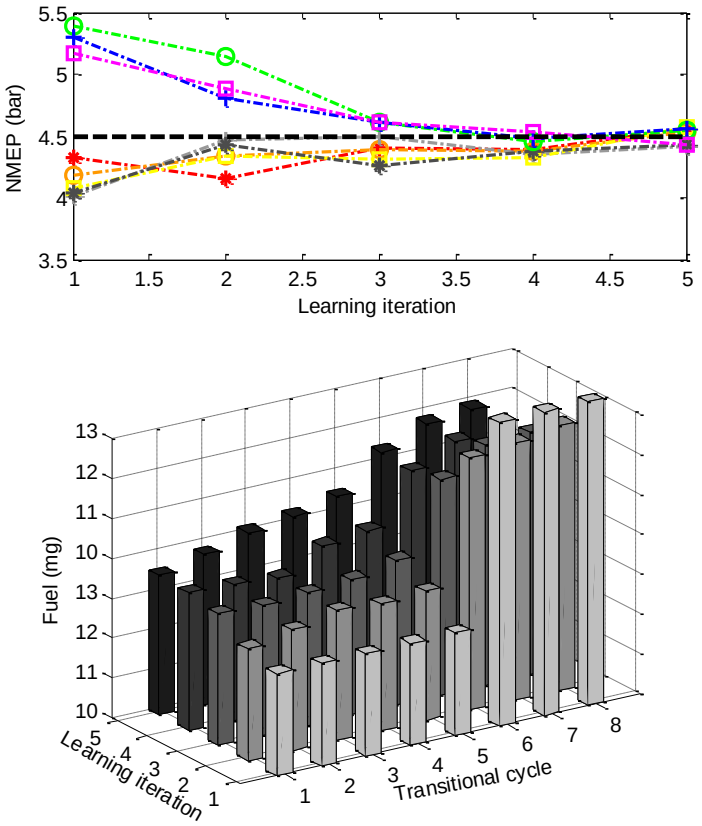

Figure 4. 26: Mode transition from HCCI to SI in 2000rpm, 4.5bar

Note that 6 engine cycles are needed for the transition from SI to HCCI at 1500 rpm. The initial fuel mass was set to the level for the steady SI mode for the first two cycles and HCCI

mode for the last four cycles. Similar performance could be observed as in 2000 rpm; NMEP dropped at middle cycles in the first iteration, and after the iterative learning converges, the total learned fuel mass shows a continuous decreasing from transition cycles 1 to 6.

For combustion mode transition from HCCI to SI, as the actions of all the actuators and the initial fuel mass are set opposite to the case of transition from SI and HCCI, NMEP was dropped from cycles 1 to 5 as the pumping loss increased, and was increased suddenly at cycle 6 as fuel mass in steady state SI was set. After 5 learning iterations, a continuous increasing fuel mass from cycle 1 to 8 was obtained as expect.

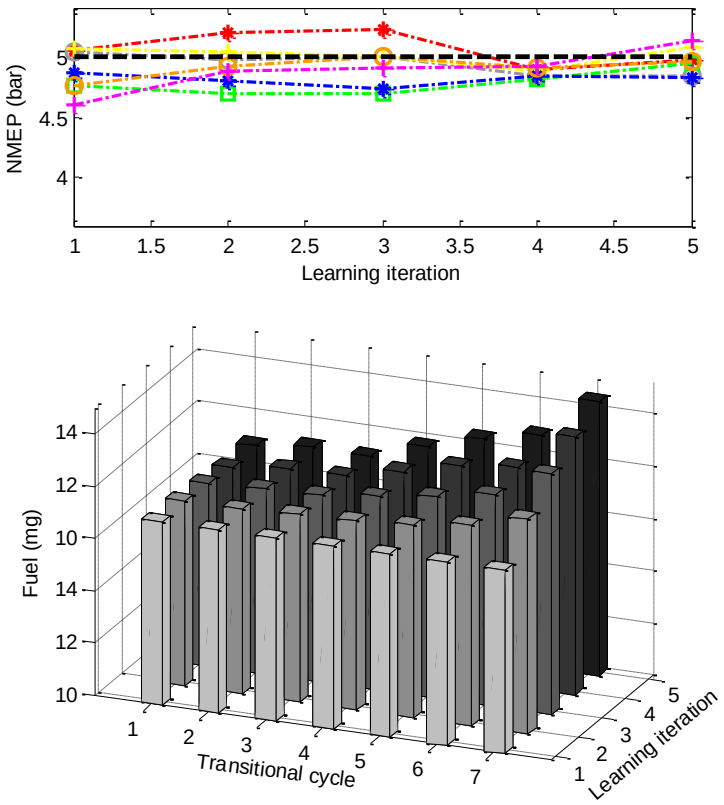

Figure 4. 27: Mode transition from HCCI to SI in 1500rpm, 5.0 bar

For the case of 1500 rpm, the other initial fuel condition was tried: fuel mass in steady HCCI mode was set to all the transition cycles. No sudden "jump" of NMEP appeared in the first learning iteration anymore, and after 5 iterations, the learning converges and similar result was obtained as in 2000 rpm.

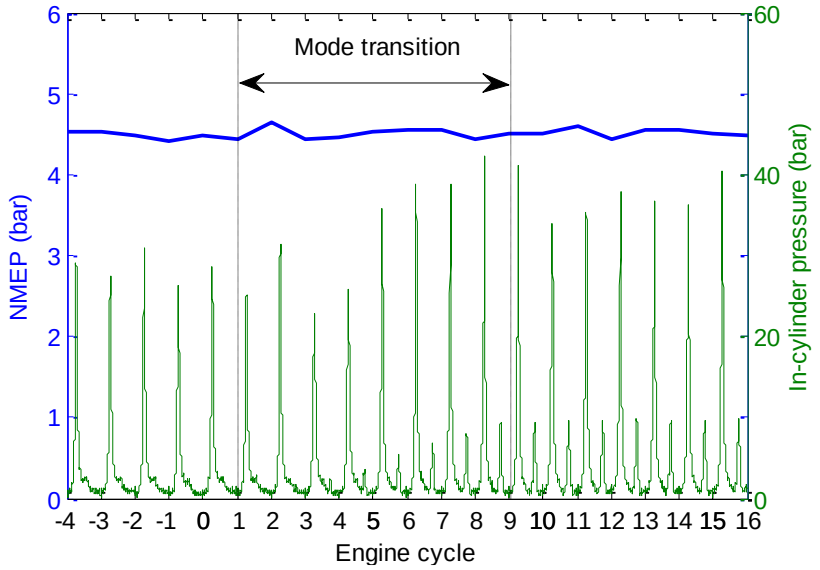

Figure 4. 28: Successful mode transition from SI to HCCI in 2000rpm, 4.5 bar

A successful mode transition from SI to HCCI combustion at 2000 rpm with 4.5 bar NMEP is represented by the in-cylinder pressure and the corresponding NMEP in Figure 4.28. During the combustion mode transition, the in-cylinder pressure trace shows a similar tendency as in Figure 4.10, and there was no significant late combustion or early auto-ignition. Note that significant combustion phase shifting could lead to large NMEP fluctuations. The smooth mode transition can be observed clearly from a continuously combustion mode transition between SI and HCCI as shown in Figure 4.29, where four mode transitions were completed within 300 engine cycles. The maximum absolute NMEP fluctuation during mode transition is about 5%.

Note that at this operational condition the maximum absolute cycle-by-cycle variation for the SI combustion is 3.5% and for the HCCI combustion is 4%. This indicates that the absolute NMEP fluctuation during the mode transition is compatible with these of steady SI and HCCI combustion. Furthermore, the maximum rate of the in-cylinder pressure rise during these transitional cycles is between these of SI combustion at about 1 bar/degree and HCCI combustion at about 4.5 bar/degree. This shows that smooth mode transition using the well regulated hybrid combustion mode was achieved by the control strategy without misfire or knock.

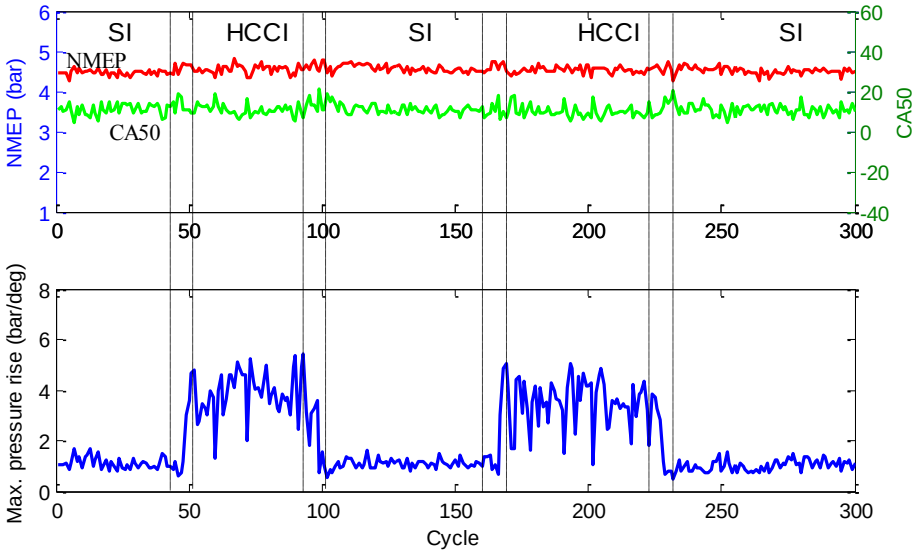

Figure 4. 29: Combustion mode transition between SI and HCCI

4.8 Hybrid Combustion Mode Observation

Then for all of these mode transition conditions, the experimental mass fraction burned (MFB) curves of the transitional cycles are shown in Figure 4.30 to Figure 4.33, where the red dots denote the auto-ignition (start of HCCI combustion in the unburned zone) location for the

hybrid combustion mode. From Figure 30 it can be observed that during the mode transition from the SI to HCCI combustion, the hybrid combustion starts at the 4th cycle when the split injection begins and it lasted for four cycles. The percentage of HCCI combustion gradually increases over the four hybrid combustion cycles. While for the case of mode transition from HCCI to SI combustion shown in Figure 4.31, the hybrid combustion lasted for five cycles, and the percentage of the HCCI combustion gradually decreases over the five hybrid combustion cycles. Note that it is not guaranteed that the mode transition always follows this pattern since the cycle-by-cycle variations, intake air temperature perturbation, and manifold pressure tracking error could affect the auto-ignition timing and even the start of the hybrid combustion cycle. To further investigate the spark timing in Figure 4.11 it can be seen that, in transitional cycles 6 and 7, the spark timing was heavily advanced; however the start of combustion, indicated by the CA10 locations of these two cycles were close to other transitional cycles; see Figure 4.31. The long ignition delay is caused by the reduced in-cylinder temperature due to the reduced effective compression ratio at beginning of transition and relatively low in-cylinder mixture temperature at IVC. This demonstrated the spark timing control is effective to maintain a reasonable CA50 for the hybrid combustion during the mode transition.

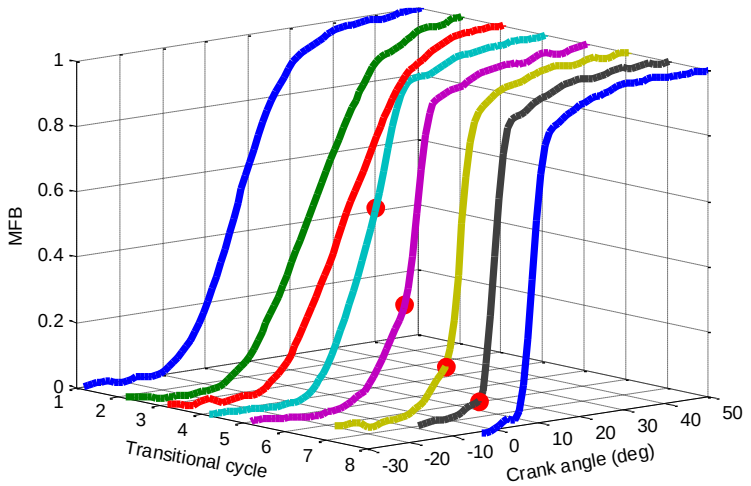

Figure 4. 30: Mode transition from SI to HCCI in 2000rpm, 4.5 bar

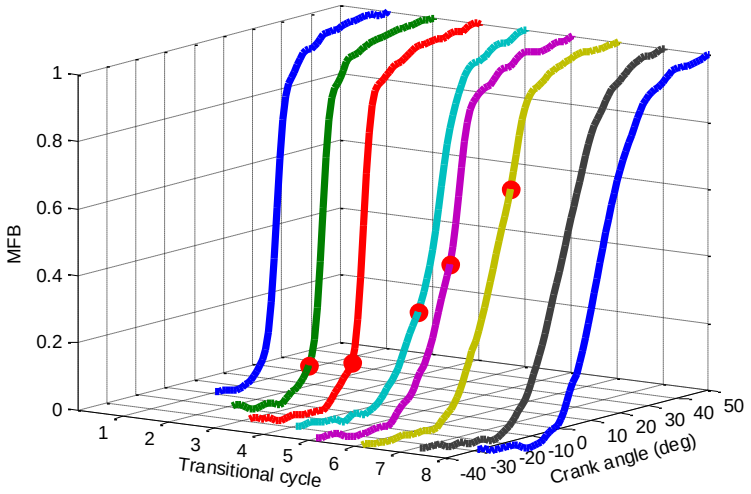

Figure 4. 31: Mode transition from HCCI to SI in 2000rpm, 4.5 bar

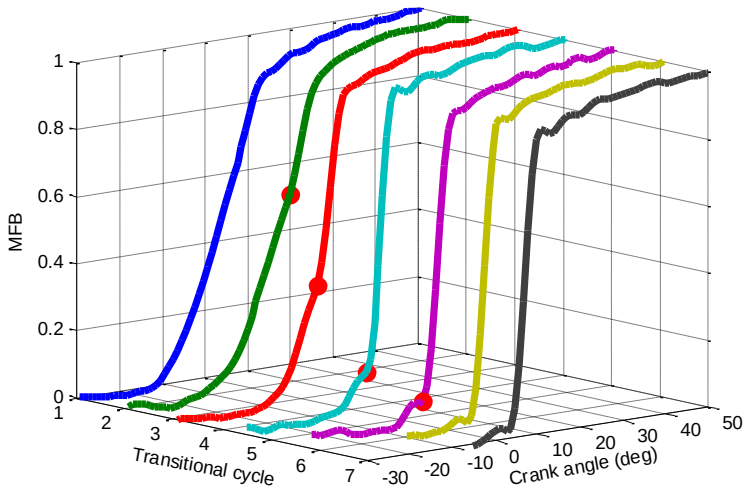

Figure 4. 32: Mode transition from SI to HCCI in 1500rpm, 5.0 bar

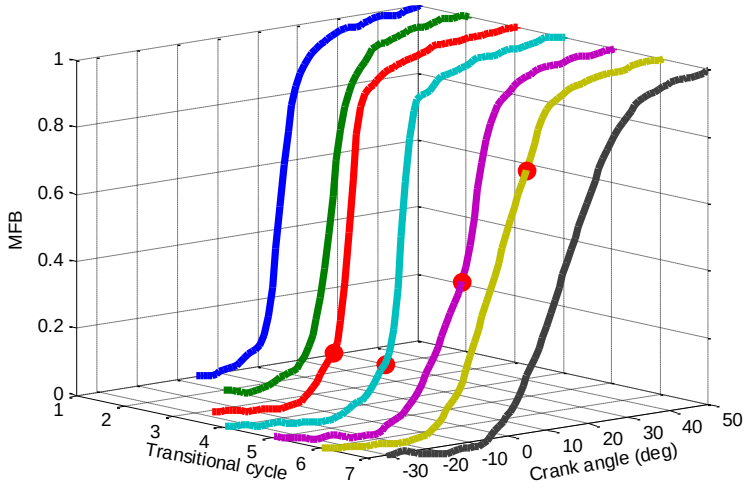

Figure 4. 33: Mode transition from HCCI to SI in 1500rpm, 5.0 bar

In the case of mode transition at 1500 rpm, hybrid combustion happened one cycle before the split injection for the SI to HCCI transition and after the split injection for the HCCI to SI transition; see Figure 4.32 and Figure 4.33. We believe that the engine thermal condition under low valve lift at this operational condition makes the auto-ignition easier than the other operational conditions.

4.9 Conclusions

A model-based control strategy for spark-ignition (SI) and homogeneously charge compression ignition (HCCI) combustion mode transition is proposed in this chapter that consists of manifold pressure control, iterative learning of NMEP (net mean effective pressure) control and sensitivity-based fuel compensator. The NMEP sensitivity of injected fuel quantity was derived based upon the control-oriented combustion model. Experiment results showed that the proposed MAP and iterative learning controller are able to achieve smooth mode transition between SI and HCCI combustion at a range of operational conditions, and the robustness under cycle-by-cycle variation has been greatly enhanced by utilizing the sensitivity-based feed-forward fuel compensator. The NMEP, an indication of engine output torque, fluctuation during the combustion mode transition was kept within 3%.

CHAPTER 5

CONCLUSIONS

5.1 Conclusions

In this dissertation, mode transition control between SI and HCCI combustion was investigated, which is one of the key challenges of realizing HCCI combustion on an HCCI capable SI engine. Firstly, for the purpose of control strategy development and validation, a control-oriented HCCI combustion engine model was developed for real-time HIL simulations. Secondly, an LPV gain-scheduling controller for the electronic throttle was designed for accurate throttle position control required by the combustion mode transition. Finally, a model-based mode transition controller between SI and HCCI combustion was developed, and smooth mode transition was demonstrated by both of the simulation and experimental validation. Based on the research results presented in Chapters 2, 3 , and 4 the following conclusions can be drawn.

- The developed control-oriented charge mixing and two-zone HCCI combustion model has shown significant improvement on combustion timing prediction and in-cylinder flow behavior than the existing one-zone model. This model is accurate enough to replace a real engine so that the proposed control strategy can be developed and validated through HIL simulations.
- The proposed LPV gain-scheduling control strategy for electronic throttle control has shown great improvement compared with conventional controllers in dealing with the high system

nonlinearity and external disturbance, and guarantees that the throttle plate position can be controlled accurately during mode transition with fast reposnse. The modeling and control design process also provides a novel approach for other mechatronics application.

- Smooth combustion mode transition was achieved by controlling the manifold pressure to track a reference trajectory that guarantees the air-to-fuel ratio to be within a reasonable range and by using the iterative learning method to regulate the NMEP during the transition. The sensitivity-based feed-forward control is able to compensate the NMEP fluctuations due to combustion cycle-by-cycle variations and the mode transition robustness was greatly improved.

5.2 Recommendations for Future work

In this dissertation, the combustion process modeling was based on MFB (mass fraction burnt) trace approximated by multiple Wiebe functions. The advantage of this approach is its simplicity, especially with low calculation requirement for real-time simulations. However, for a large operational range, calibrating the engine becomes complicated. And for the HCCI combustion, different operational conditions, such as air-to-fuel ratio and residual gas fraction, could lead to quite different combustion characteristics; a simple Wiebe function may not approximate the combustion process accurately. To improve this part of model, the alternative approach is chemical reaction-based modeling. By considering the chemical reactions of a few major molecules in the fuel, the real-time simulation requirement might be also satisfied.

In addition, controlling the HCCI combustion process is another important topic. Due to the cycle-to-cycle residual gas dynamics, auto-ignition timing is also relatively difficult to control. However, to consider the effect of combustion indecs (such as CA50, burn duration, etc.) of

current cycle to the next cycle, the complicated nonlinear system might be simplified into an LPV system, and certain control strategies could be applied for the combustion control problem.

BIBLIOGRAPHY

BIBLIOGRAPHY

[1] Thring, R., “Homogeneous-charge compression-ignition (HCCI) engines,” SAE Technical Paper 892068, 1989 (doi: 10.4271/892068).

[2] Aoyama, T., Hattori, Y., Mizuta, J., and Sato, Y., “An experimental study on premixed-charge compression ignition gasoline engine,” SAE Technical Paper 960018, 1996 (doi: 10.4271/960081).

[3] R. H. Stanglmaier and C. E. Roberts, “Homogeneous Charge Compression Ignition (HCCI): Benefits, Compromises, and Future Engine Applications,” *SAE Technical Paper*, SAE 1999-01-3682, 1999.

[4] Li, J., Zhao, H., Ladommatos, N., and Ma, T., “Research and development of controlled auto-ignition (CAI) combustion in a 4-Stroke multi-cylinder gasoline engine,” SAE Technical Paper 2001-01-3608, 2001 (doi: 10.4271/2001-01-3608)

[5] H. Zhao, *HCCI and CAI Engines for the Automotive Industry*. Cambridge, UK: WoodheadPublishing, 2007, pp. 6-36.

[6] Milovanovic, N., Blundell, D., Pearson, R. et al., “Enlarging the operational range of a gasoline HCCI engine by controlling the coolant temperature,” SAE Technical Paper 2005-01-0157, 2005 (doi: 10.4271/2005-01-0157).

[7] Yao, M., Chen, Z., Zheng, Z., et al., “Effect of EGR on HCCI combustion fuelled with dimethyl ether (DME) and methanol dual-fuels,” SAE Technical Paper 2005-01-3730, 2005 (doi: 10.4271/2005-01-3730).

[8] Z. Ren and G. Zhu, “Integrated system ID and control design for an IC engine variable valve timing system,” *Journal of Dynamic Systems, Measurement, and Control* 133.2 (2011): 021012.

[9] Santoso, H., Matthews, J., and Cheng, W. K., “Managing SI/HCCI dual-mode engine operation,” SAE Technical Paper 2005-01-0162, 2005 (doi: 10.4271/2005-01-0162).

[10] Urata, Y., Awasaka, M., Takanashi, J., et al., “A study of gasoline-fuelled HCCI engine equipped with an electromagnetic valve train,” SAE Technical Paper 2004-01-1898, 2004 (doi: 10.4271/2004-01-1898).

[11] Fuerhapter, A., Unger, E., Piock, W. F., and Fraidl, G. K., "The new AVL CSI engine - HCCI operation on a multi-cylinder gasoline engine," SAE Technical Paper 2004-01-0551, 2004 (doi: 10.4271/2004-01-0551).

[12] H. Wu, et al., "Experimental investigation of a control method for SI-HCCI-SI transition in a multi-cylinder gasoline engine." *SAE International Journal of Engines* 3.1 (2010): 928-937.

[13] A. Widd, et al., "Investigating mode switch from SI to HCCI using early intake valve closing and negative valve overlap." *2011 JSAE/SAE International Powertrains, Fuel & Lubricants*. 2011.

[14] P. Kongsereeparp, et al, "A Stand-along Multi-zone Model for Combustion in HCCI Engines," *ASME Internal Combustion Engine Division 2005 Fall Technical Conference*, Ottawa, ON, Canada, September, 2005, pp. 265-274.

[15] N. P. Komninos, "Modeling HCCI combustion: Modification of a multi-zone model and comparison to experimental results at varying boost pressure," *Applied Energy*, 86 (2009), pp. 2141-2151.

[16] D. J. Rausen and A. G. Stefanopoulou, "A Mean-Value Model for Control of Homogeneous Charge Compression Ignition (HCCI) Engines," *ASME Journal of Dynamics, Measurement, and Control*, vol. 127, Sep 2005.

[17] G. M. Shaver, M. J. Roelle, and J. C. Gerdes, "Modeling Cycle-to-cycle Dynamics and Mode Transition in HCCI Engines with Variable Valve Actuation," *Control Engineering Practice*, 14 (2006), pp 213–222.

[18] X. Yang and G. Zhu, "A Control-oriented Hybrid Combustion Model of a Homogeneous Charge Compression Ignition Capable Spark Ignition Engine," *Journal of Automobile Engineering*, San Francisco, CA, June, 2011.

[19] V. Tandra and N. Srivastava, "A Two Zone Model of a Single Cylinder HCCI Engine for Control Applications," *2008 ASME Dynamics and Control Conference*, Ann Arbor, Michigan, October, 2008.

[20] S. Zhang, G. Zhu, Y. Yoon, and Z. Sun, "A Control Oriented Charge Mixing and HCCI Combustion Model for Internal Combustion Engines ," *2012 ASME Dynamic Systems and Control Conference,* 2012 vol. 226 pp.1380-1395.

[21] J. B. Heywood, *Internal Combustion Engine Fundamentals*. New York: McGraw-Hill, Inc., 1988.

[22] G. Woschni, "A Universally Applicable Equation for Instantaneous heat Transfer Coefficient in the Internal Combustion Engine," *SAE Technical Paper*, SAE 670931, 1967.

[23] J. Chang and O. Guralp, "New Heat Transfer Correlation for an HCCI Engine Derived from Measurements of Instantaneous Surface Heat," *SAE Technical Paper*, SAE 2004-01-2996, 2004.

[24] A. M. Mahrous, et al, "Effect of Intake Valves Timings on In-Cylinder Charge Characteristics in a DI Engine Cylinder with Negative Valve Overlapping," *SAE Technical Paper*, SAE 2008-01-1347, 2008.

[25] T. Lucchini, G. D'Errico, and M. Fiocco, "Multi-Dimensional Modeling of Gas Exchange and Fuel-Air Mixing Process in a Direct-Injection, Gas Fueled Engine," *SAE Int.*, SAE 2011-24-0036, 2011.

[26] R. B. Bird, W. E. Stewart, E. N. Lightfoot, *Transport Phenomena*. John Wiley & Sons, Inc., 2007, pp. 659.

[27] M. Hillion, J. Chauvin, and N. Petit, "Controlling the Start of Combustion on an HCCI Diesel Engine," *2008 American Control Conference*, Seattle, Washington, June, 2008.

[28] J. Bengtsson, M. Gafvert, and P. Strandh, "Modeling of HCCI Engine Combustion for Control Analysis," *43rd IEEE Conference on Decision and Control*, Atlantis, Paradise Island, Bahamas, December, 2004.

[29] S. Tanaka, F. Ayala, J. C. Keck, and B. Heywood, "Two-stage ignition in HCCI combustion and HCCI control by fuels and additives," *Combustion and Flame*, 132 (2003), pp. 219–239.

[30] A. Iqbal, et al, "Ignition Delay Correlation for Predicting Autoignition of a Toluene Reference Fuel Blend in Spark Ignition Engines," *SAE Int*., SAE 2011-01-0338.

[31] M. Canova, et al, "A Control-Oriented Model of Combustion Process in a HCCI Diesel Engine," *2005 American Control Conference,* Portland, OR, June, 2005.

[32] D. Kawano, et al, "Effect of fuel properties on combustion and exhaust emissions of homogeneous charge compression ignition (HCCI) engine," *SAE Technical Paper*, SAE 2004-01-1966.

[33] K. Kuwahara, et al, "Chemical Kinetics Study on Two-stage Main Heat Release in Ignition Process of Highly Diluted Mixtures," *SAE Int.*, SAE 2013-01-1657.

[34] C. Rossi, A. Tilli, and A. Tonielli, "Robust Control of a Throttle Body for Drive by Wire Operation of Automotive Engines," *IEEE Transactions on Control Systems Technology*, Vol. 8, No.6, November, 2000.

[35] S. Satou, S. Nakagawa, etc, "An Accurate Torque-based Engine Control by Learning Correlation between Torque and Throttle Position," *SAE Technical Paper Series*, 2008-01-1015, 2008.

[36] H. Lee and S. Sul, "Fuzzy-Logic-Based Torque Control Strategy for Parallel-Type Hybrid Electric Vehicle," *IEEE Transactions on Industrial Electronics*, Vol. 45, No. 4, August, 1998.

[37] V. H. Johnson, K. B. Wipke, and D. J. Rausen, "HEV Control Strategy for Real-Time Optimization of Fuel Economy and Emissions," *SAE Technical Paper Series*, 2000-01-1543, 2000.

[38] X. Yang and G. Zhu. "SI and HCCI Combustion Mode Transition Control of an HCCI Capable SI Engine," *IEEE Transactions on control systems technology*, Vol. 21, No.5, September, 2013.

[39] C. C. de Witt, I. Kolmanovsky, and J. Sun, "Adaptive Pulse Control of Electronic Throttle," *2001 American Control Conference*, Arlington, VA, June, 2001.

[40] J. Deur, D. Pavkovic, N. Peric, et al. "An Electronic Throttle Control Strategy Including Compensation of Friction and Limp-Home Effects," *IEEE Transactions on Industry Applications*, Vol. 40, No.3, May, 2004.

[41] S. Jiang, M. H. Smith, and J. Kitchen. "Optimization of PID Control for Engine Electronic Throttle System Using Iterative Feedback Tuning," *SAE Technical Paper Series*, 2009-01-0370, 2009.

[42] M. Yokoyama, K. Shimizu, and N. Okamoto. "Application of sliding-mode servo controllers to electronic throttle control," *Decision and Control, 1998. Proceedings of the 37th IEEE Conference on*. Vol. 2. IEEE, 1998.

[43] A. Beghi, L. Nardo, and M. Stevanato, "Observer-Based Discrete-Time Sliding Mode Throttle Control for Drive-By-Wire Operation of a Racing Motorcycle Engine," *IEEE Transaction on Control System Technology*, Vol. 14, No.4, July, 2006.

[44] M. Reichhartinger, and M. Horn, "Application of Higher Order Sliding-Mode Concepts to a Throttle Actuator for Gasoline Engines," *IEEE Transaction on Industrial Electronics*, Vol. 56, No.9, September, 2009.

[45] X. Gong, et al. "A Nonlinear Feedforward-Feedback Controller Design for Electronic Throttle Based on Flatness." *2012 24th Chinese Control and Decision Conference (CCDC)*. IEEE, 2012.

[46] G. Panzani, M. Corno, and S. Savaresi, "On Adaptive Electronic Throttle Control for Sport Motorcycles," Control Engineering Practice 21(1), 2013, pp. 42–53.

[47] L. Wu, X. Yang, and F. Li, "Nonfragile Output Tracking Control of Hypersonic Air-Breathing Vehicles With an LPV Model," *IEEE Transaction on Mechatronics*, Vol. 18, No.4, August, 2013.

[48] R. Merry, J. Holierhoek, M. Molengraft, et al. "Gain Scheduling Control of a Walking Piezo Actuator," *IEEE Transaction on Mechatronics*, Vol. 19, No.3, June, 2014.

[49] M. Corno, M. Tanelli, S. Savaresi, et al. "Design and Validation of a Gain-Scheduled Controller for the Electronic Throttle Body in Ride-by-Wire Racing Motorcycles," *IEEE Transaction on Control System Technology*, Vol. 19, No.1, January, 2011.

[50] S. Zhang, J. Yang, and G. Zhu, "LPV modeling and mixed constrained H_2/H_∞ control of an electronic throttle," *IEEE transactions on mechatronics*, 2014 vol. pp issue 99 (doi: 10.1109/TMECH.2014.2364538).

[51] X. Chen, Y. Wang, I. Haskara, and G. Zhu, "Optimal Air-to-Fuel Ratio Tracking Control with Adaptive Biofuel Content Estimation for the LNT Regeneration," *IEEE Transaction on Control System Technology* (*Published online*, DOI: 10.1109/TCST.2013.2252350)

[52] G. Zhu, M. A. Rotea, and R. E. Skelton, "A Convergent Algorithm for the Output Covariance Constraint Control Problem," *SIAM Journal of Control and Optimization*, Vol. 35, No. 1, pp. 341-361, Jan., 1997.

[53] A. White, G. Zhu, and J. Choi, "A Linear Matrix Inequality Solution to the Input Covariance Constraint Control Problem," *2013 ASME Dynamic Systems and Control Conference*, Palo Alto, CA, October, 2013.

[54] K. Zhou, J. C. Doyle, *Essentials of Robust Control*. New jersey: Prentice Hall, 1998

[55] K. Ogata, *Discrete-time Control Systems*. Englewood Cliffs, NJ: Prentice Hall, 1995

[56] J. Warrem, S. Schaefer, etc. "Barycentric Coordinates for Convex Sets," *Advances in Computational Mathematics,* Vol. 27, No. 3, 2007, pp. 319-338.

[57] J. D. Caigny, J. F. Camino, R. Oliveira, P. Peres, and J. Swevers, "Gain-scheduled H_2 and H_∞ Control of Dicrete-time Polytopic Time-varying Systems," *IET Control Theory and Applications,* 4: 362-380, 2010.

[58] A. White, G. Zhu, and J. Choi, "Guaranteed l_2 to l_∞ Control for Discrete-time Polytopic LPV Systems," *2013 American Control Conference*, Washington, DC, June, 2013.

[59] A. White, Z. Ren, G. Zhu, and J. Choi, "Mixed H_2/H_∞ Observer-Based LPV Control of a Hydraulic Engine Cam Phasing Actuator," *IEEE Transaction on Control System Technology*, Vol. 21, No.1, January, 2013.

[60] A. White, G. Zhu, and J. Choi, *Linear Parameter Varying Control for Engineering Applications,* Springer-Verlag London Limited, May 10, 2013.

[61] R. H. Stanglmaier and C. E. Roberts, "Homogeneous Charge Compression Ignition (HCCI): Benefits, Compromises, and Future Engine Applications," *SAE Technical Paper, SAE 1999-01-3682*, 1999.

[62] F. Zhao, T. Asmus, D. Assanis, et al., "Homogeneous Charge Compression Ignition (HCCI) Engines: Key Research and Development Issues," *Progress in Technology*, 94, 2003.

[63] G. Zhu, S. Zhang, A. Huisjen, and H. Schock, "Fast Combustion mode transition between HCCI and SI Combustion," DOE ACE/HCCI working group meeting, San Francisco, CA, February, 2013.

[64] H. Wu, et al., "Experimental investigation of a control method for SI-HCCI-SI transition in a multi-cylinder gasoline engine." *SAE International Journal of Engines* 3.1 (2010): 928-937.

[65] A. Widd, et al., "Investigating mode switch from SI to HCCI using early intake valve closing and negative valve overlap." *2011 JSAE/SAE International Powertrains, Fuel & Lubricants*. 2011.

[66] N. Ravi, et al., "Closed-loop Control of SI-HCCI Mode Switch Using Fuel Injection Timing," *2013 ASME Dynamic Systems and Control Conference*, 2013.

[67] X. Yang, G. Zhu, and X. Chen, "SI and HCCI Combustion Mode Transition Control of an HCCI Capable SI Engine," *IEEE Transactions on control systems technology*, Vol. 21, No.5, September, 2013.

[68] S. Zhang, A. P. White, J. Yang, and G. Zhu, "LPV Control of an Electronic Throttle," *2013 ASME Dynamic Systems and Control Conference*, San Francisco, CA, October, 2013.

[69] Z. Wang, J. Wang, S. Shuai, et al., "Study of the Effect of Spark Ignition on Gasoline HCCI Combustion," *Proceedings of the Institution of Mechanical Engineers, Part D, Journal of Automobile Engineering*, 2006 220: 817, DOI: 10.1243/09544070JAUTO151.

[70] B. T. Zigler, P. E. Keros1, K. B. Helleberg1, et al., "An experimental investigation of the sensitivity of the ignition and combustion properties of a single-cylinder research engine to spark-assisted HCCI," *International Journal of Engine Research*, 2011, 12(4): 353-375.

[71] J. Hyvönen, G. Haraldsson, B. Johansson, "Operating Conditions Using Spark Assisted HCCI Combustion During Combustion Mode Transfer to SI in a Multi-Cylinder VCR-HCCI Engine," SAE Technical Paper 2005-01-0109, 2005, doi: 10.4271/2005-01-0109.

[72] P. G. Aleiferis, A. G. Charalambides, Y. Hardalupas, et al., "Autoignition Initiation and Development of n-heptane HCCI Combustion Assisted by Inlet Air Heating, Internal EGR or Spark Discharge: An Optical Investigation," SAE Technical Paper 2006-01-3273, 2006, doi: 10.4271/2006-01-3273.

[73] T. Matsuda, H. Wada, T. Kono, et al., "A Study of a Gasoline-fueled HCCI Engine~Mode Changes from SI Combustion to HCCI," SAE Technical Paper 2008-01-0050, 2008, doi: 10.4271/2008-01-0050.

[74] T. Urushihara, K. Hiraya, A. Kakuhou, et al., "Expansion of HCCI Operating Region by the Combination of Direct Fuel Injection, Negative Valve Overlap and Internal Fuel Reformation," SAE Technical Paper 2003-01-0749, 2003, doi: 10.4271/2003-01-0749.

[75] L. Koopmans, R. Ogink, I. Denbratt, "Direct Gasoline Injection in the Negative Valve Overlap of a Homogeneous Charge Compression Ignition Engine," SAE Technical Paper 2003-01-1854, 2003, doi: 10.4271/2003-01-1854.

[76] S. Zhang, G. Zhu, and Z. Sun, "A Control-Oriented Charge Mixing and Two-zone HCCI Combustion Model," *IEEE transactions on vehicular technology*, 2013 vol. pp issue 99.

[77] M. Mittal, G. Zhu, and H. J. Schock, "Fast mass fraction burned calculation using net pressure method for real-time applications," *Proceedings of the Institution of Mechanical Engineers, Part D, Journal of Automobile Engineering*, Vol. 223, pp389-394, 2009.

[78] H. Adam, G. Pradeep, and Z. Sun, "Iterative learning control of a fully flexible valve actuation system for non-throttled engine load control," Control Engineering Practice, v.19, no.12, 2011 Dec, pp.1490-1505.

[79] J. Heywood, *Internal Combustion Engine Fundamentals*. New York: McGraw-Hill, Inc., 1988.

[80] M. Hillion, J. Chauvin, and N. Petit, "Controlling the Start of Combustion on an HCCI Diesel Engine," *2008 American Control Conference*, Seattle, Washington, June, 2008.

[81] S. S. Saab, "On the P-type Learning Control," *IEEE Transactions on automatic control*, Vol. 39, No.11, November, 1994.

[82] C. Chien, J. Liu, "A P-type Iterative Learning Controller for Robust Output Tracking of Nonlinear Time-varying Systems," *1994 American Control Conference*, Baltimore, Maryland, June, 1994

[83] D. Wang, "Convergence of robustness of discrete time nonlinear systems with iterative learning control," *Automatica*, Vol. 34, No.11, pp. 1445-1448, 1998

[84] F. A. Ayala, M. D. Gerty, and J. B. Heywood, "Effect of combustion phasing, relative air-fuel ratio, compression ratio, and load on SI engine efficiency." *SAE Technical Paper, SAE 2006-01-0229*, 2006